

**Development and Application of DFT Based Methods for Studying Transition Metal Oxide  
Catalysis**

by

Shang Jiang

A thesis submitted in partial fulfillment of the requirements for the degree of

Master of Science

in

Chemical Engineering

Department of Chemical and Materials Engineering

University of Alberta

©Shang Jiang, 2022

## Abstract

Transition metal oxides (TMOs) are commonly used as catalysts and catalyst supports in a variety of chemical transformations. Computational tools like density functional theory (DFT) are often used to study TMO catalyzed reactions, as TMOs are strongly correlated systems which require the additional Hubbard U-correction to reduce the systematic error caused by excessive electron delocalization in DFT. However, commonly reported U values are optimized to reproduce bulk properties and fail to predict surface properties like surface-adsorbate interactions and catalytic reaction energetics. Meanwhile, experimental surface characterization techniques like X-ray Photoelectron Spectroscopy (XPS) have difficulties identifying key surface adsorbates or reaction intermediates corresponding to the XPS shifts observed. A synergistic application of XPS and DFT+U can be used to determine the surface specific U values, as well as unidentified adsorbed surface moieties on the TMO surface. NiO and Co<sub>3</sub>O<sub>4</sub> were chosen as sample TMOs in this thesis. We use previously published experimental XPS shifts data to gauge the DFT+U calculated core level binding energy shifts with U values ranging from 0-6eV, for clean catalyst surface or probable adsorbates with potential surface vacancies. For NiO, the U value ~2eV is able to reproduce the experimental XPS O1s core level binding energy correctly and this surface specific U value of 2eV also helps in assigning the experimental observed shifts to adsorbed oxygen (+1.8 and +2.2eV), surface lattice oxygen on which hydrogen is dissociative adsorbed (+2.2eV) and the oxygen connected with hydrogen and carbon in adsorbed HCO<sub>2</sub> closed to a Ni Vacancy site on the NiO surface. As for Co<sub>3</sub>O<sub>4</sub>, despite of the disagreement on the bulk property optimized U value, ~3eV of U value could successfully predict the experimentally observed XPS shifts, and these shifts are also identified to be surface lattice oxygen on which hydrogen is dissociative adsorbed, the oxygen connected with carbon and surface cobalt in adsorbed HCO<sub>3</sub>

for +1.5eV and the oxygen connected with carbon and surface cobalt in adsorbed  $\text{HCO}_2$  for +2.6eV. Then, we demonstrated the application of surface property optimized U value to elucidate demethylation of benzyl alcohol to phenol on CuO surface in water and at room temperature. The surface U value of CuO, 4eV is benchmarked by the same method and is able to accurately capture the adsorption free energy of hydrogen on CuO(111) surface. Using a combination of catalyst characterization, chemical and acoustic analysis, isotope labelling and density functional theory computations, we reveal the molecular reaction mechanism, involving benzaldehyde as an intermediate. Water is not just a benign solvation medium but it directly participates in the chemistry by getting dissociated due to ultrasound and the OH from water gets adsorbed on the catalyst surface, inhibiting its recombination. The surface adsorbed OH from water plays a key role in activating the C-H bond in benzyl alcohol to form benzaldehyde and later incorporates itself into the phenyl ring to form phenol.

## Preface

This thesis focuses on two parts, i) determining surface specific Hubbard-U corrections and identifying key adsorbates on NiO and Co<sub>3</sub>O<sub>4</sub> and ii) computational investigations on low-temperature, water assisted tandem demethylenation of benzyl alcohol to phenol on CuO. The research presented in Chapter 4 and all the computational work from Chapter 5, is my original work.

Chapter 5 summarizes work done in collaboration with Teseer Bahry, Umesh Jonnalagadda, Wen Liu, Benoit Teychene, Francois Jerome and Prince Nana Amaniampong. They performed the catalyst preparation and characterization and provided all the experimental data. All the computational calculation were performed by myself under the guidance of Dr. Samir H. Mushrif. Manuscript preparation was accomplished with the help of Dr. Samir H. Mushrif.

A version of Chapter 4 has been submitted for publication in *Physical Chemistry Chemical Physics (PCCP)* as

Jiang, S. and Mushrif, S.H., *Determining surface-specific Hubbard-U corrections and identifying key adsorbates on Nickel and Cobalt oxide catalyst surfaces*

A version of Chapter 5 has been submitted for publication in *Nature Catalysis* as

Bahry, T., Jiang, S., Jonnalagadda, U., Liu, W., Teychene, B., Jerome, F., Mushrif, S.H. and Amaniampong, P.N., *Sonocatalytic, water-assisted tandem demethylenation of benzyl alcohol to phenol*

## **Acknowledgement**

I would like to thank my supervisor Dr. Samir H. Mushrif for his continuous support and guidance throughout my graduate program. Your expertise, patience and passion for research have helped me overcome numerous difficulties and inspired me to become a better person.

I would like to thank my current and former group members for their support and encouragement. Arul Padmanathan, Jose Carlos Velasco Calderon, Nilesh Orupattur, Prof. Ojus Mohan, Sagar Bathla and Seth Beck, I am so fortunate that I have the opportunities to work with such talented and heartening friends.

I would like to thank the Department of Chemical and Material Engineering, Faculty of Engineering, Faculty of Graduate Studies and Research, University of Alberta. The financial support from Natural Sciences and Engineering Research Council of Canada (NSERC) and computational resources from Digital Research Alliance of Canada (previously known as Compute Canada) are gratefully acknowledged.

## Tables of Contents

1. Introduction .....	1
2. Literature Survey .....	4
2.1 Previously reported experimental XPS core level binding energy shifts .....	4
2.2 Examples of how the bulk U values fail to capture/predict surface properties .....	5
2.3 Previous investigations of U values on CuO, NiO and Co <sub>3</sub> O <sub>4</sub> .....	6
2.4 Previous Studies of Sonochemistry on TMO catalysis .....	8
3. Methodology.....	10
3.1 The Formulation of DFT .....	10
3.2 The implementation of Hubbard U-correction in DFT+U.....	15
3.3 Computational methods .....	16
4. Determining surface specific Hubbard-U corrections and identifying key adsorbates on NiO and Co <sub>3</sub> O <sub>4</sub> .....	19
4.1 Benchmarking for computational parameters of NiO model .....	19
4.2 Benchmarking for computational parameters of Co <sub>3</sub> O <sub>4</sub> model.....	23
4.3 Screening of adsorbates on NiO (100) and Co <sub>3</sub> O <sub>4</sub> (100).....	27
4.4 The Rationale of Structure of Different Molecules Adsorbed on TMO surface .....	30
4.5 Comparison of experimental and computational core level binding energy shifts .....	32
5. Low-temperature, water assisted tandem demethylation of benzyl alcohol to phenol.....	38
5.1 Summary of the experimental results of benzyl alcohol conversion on CuO .....	38
5.2 DFT+U investigations into benzyl alcohol conversion to phenol on CuO (111).....	48
5.3 Benzyl alcohol to phenol reaction mechanism .....	51
5.4 The role of water/hydrogen peroxide in the formation of phenol .....	52
5.5 Benzaldehyde and hydroxy-benzyl alcohol reactions .....	53
5.6 The formation of ethylene glycol as the side product .....	55
6 Conclusions and Future Work .....	57

## List of Tables

Table 2.1 Previously reported O1s core level binding energy shifts and corresponding surface adsorbates assigned.....	5
Table 4.1 The DFT calculated energy of the system of NiO with different k-point choices.....	23
Table 4.2 The DFT calculated energy of the system of Co <sub>3</sub> O <sub>4</sub> with different k-point choices...	26
Table 4.3 O1s Core-level Binding Energy Shifts Relative to the O1s Core-level Binding Energy of Bulk Lattice Oxygen for Different Surface Adsorbates (corresponding to Fig. 4.9) on NiO (100) evaluated at U value of 5.3eV and 2eV.....	29
Table 4.4 O1s Core-level Binding Energy Shifts Relative to the O1s Core-level Binding Energy of Bulk Lattice Oxygen for Different Surface Adsorbates (corresponding to Fig. 4.10) on Co <sub>3</sub> O <sub>4</sub> (100) evaluated at U value of 6.0eV and 3.5eV.....	30
Table 5.1 Product yields for the CuO catalyzed sonochemical oxidation of model substrate .....	57

## List of Figures

Figure 2.1 a) DFT predicted hydrogen adsorption enthalpy at different U values and b) DFT predicted core level binding energy shift for oxygen in adsHCO <sub>2</sub> at different U values, both on CuO (111) surface.....	7
Figure 3.1 The wave function of the system under the nuclear potential and under the pseudopotential .....	15
Figure 3.2 Slab model for a) NiO (100), b) Co <sub>3</sub> O <sub>4</sub> (100) and c) CuO (111) surface. ....	18
Figure 4.1 DFT+U optimized lattice parameter for NiO using different U values in comparison with experimentally measured lattice parameter .....	20
Figure 4.2 The most stable magnetic arrangement for NiO (100) .....	21
Figure 4.3 Convergence test showing the variation in calculated surface oxygen O1s core level binding energy shifts with the increasing slab thickness (number of layers) for surface oxygen on NiO(100) .....	21
Figure 4.4 Representation of the system used to model NiO (100) surface, slab size, illustrating the number of layers and vacuum thickness .....	22
Figure 4.5 DFT+U optimized lattice parameter for Co <sub>3</sub> O <sub>4</sub> using different U values in comparison with experimentally measured lattice parameter .....	24
Figure 4.6 The most stable magnetic arrangement for Co <sub>3</sub> O <sub>4</sub> (100).....	24
Figure 4.7 Convergence test showing the variation in calculated surface core level binding energy with the increasing slab thickness (number of layers) for surface oxygen on Co <sub>3</sub> O <sub>4</sub> (100).....	25
Figure 4.8 Representation of the system used to model Co <sub>3</sub> O <sub>4</sub> (100) surface, slab size, illustrating the number of layers and vacuum thickness.....	26
Figure 4.9 Structure of various surface adsorbates on NiO (100) surface evaluated to comparing with experimental XPS core level binding energy shifts.....	28
Figure 4.10 Structure of various surface adsorbates on Co <sub>3</sub> O <sub>4</sub> (100) surface evaluated to comparing with experimental XPS core level binding energy shifts.....	28
Figure 4.11 Variation of computed O1s core level binding energy shifts at different U values for a.) O <sub>2 ads</sub> – O2, b.) O <sub>2 ads</sub> – O1, c.) O attached with adsorbed H atom, d.) HCO <sub>2 ads</sub> – O3@Ni_vac on NiO (100) surface .....	34
Figure 4.12 Variation of computed O1s core level binding energy shifts at different U values for a.) O attached with adsorbed H atom, b.) HCO <sub>3 ads</sub> – O1, c.) HCO <sub>2 ads</sub> – O1, d.) HCO <sub>2 ads</sub> – O2 on Co <sub>3</sub> O <sub>4</sub> (100) surface. ....	36
Figure 5.1 (a) XRD analysis (b) SEM analysis (c) TEM analysis (d) AFM analysis (e) XPS Cu2p analysis (f) XPS Cu LMM analysis, of as-prepared CuO catalyst .....	40



Figure 5.2 In-situ formation of H <sub>2</sub> O <sub>2</sub> in the presence and absence of CuO catalyst and In-situ formation of H <sub>2</sub> O <sub>2</sub> in the presence of CuO-864 catalyst (blue code), in-situ formation of H <sub>2</sub> O <sub>2</sub> during hot filtration test (red code) .....	42
Figure 5.3 Conversion of benzyl alcohol and phenol yields in the ultrasound reactor, as a function of time.....	44
Figure 5.4 Mechanisms and energy profiles of the conversion of benzyl alcohol to phenol on CuO (111) .....	49
Figure 5.5 Free Energy profile for the catalytic conversion of benzyl alcohol to phenol on CuO (111) surface and various intermediate and transition states .....	50
Figure 5.6 The configurations for (a) water molecule adsorbed on CuO (111); (b) transition state and (c) final state of water dissociation on CuO(111) surface.....	53
Figure 5.7 hydroxy-benzyl alcohol adsorption configurations on CuO (111) surface .....	54
Figure 5.8. Free Energy profile for the formation ethylene glycol on CuO (111), from the aldehyde groups cleaved from benzaldehyde. ....	55

## List of abbreviations and symbols

cRPA	Constrained random phase approximation
DFT	Density functional theory
GGA	Generalized gradient approximation
E	Energy of the system
H	Hamiltonian
HFUS	High Frequency Ultrasound
LDA	Local-density approximation
PBE	Perdew-Burke-Ernzerhof functional
RPA	Random phase approximation
T	Kinetic energy
TMO	Transition metal oxide
U	Hubbard U correction
XC	Exchange correlation
XPS	X-ray photoelectron spectroscopy
$v$	Potential of the system
$\rho$	Electron density
$\Psi$	Wave function

## 1. Introduction

Transition metal oxides (TMOs) are commonly used in a variety of reactions as catalysts and catalyst supports in industrial processes, such as selective oxidation and dehydrogenation of hydrocarbons to produce chemicals, chemical-looping combustion, and water-gas shift reaction<sup>1-3</sup>. TMOs are utilized for their semiconductive properties and surface catalytic activities, with advantage of low cost, high surface area and low toxicity<sup>1</sup>. TMOs are classified as reducible and irreducible depending on the energy cost of breaking the metal-oxygen bond, and reducibility is one of the most key characteristics of TMO catalysts in reactions. Typically, the TMOs with reported band gaps lower than 3eV are considered reducible<sup>4</sup>. Reducible TMOs are characterized by facile oxygen vacancy formation which could promote redox reaction via its surface metal cations, while irreducible TMOs have a relatively higher vacancy formation energy<sup>4-6</sup>. The performance of a TMO catalyst for a specific reaction also depends on the adsorbate-surface interaction and the type and degree of doping on the catalyst surface<sup>2</sup>. Hence, TMO catalyzed reactions are complicated and the dynamic nature of the surface under reaction conditions is very important to understand for the future design and development of TMO-based catalysts.

Experimental surface characterization techniques like X-ray Photoelectron Spectroscopy (XPS) are commonly used for catalyst characterization, and they could provide insights into the change in the chemical state and the environment of surface species on TMO catalyst during the reaction<sup>7,8</sup>. The experimentally measured chemical shifts in core level binding energies is often used to identify the structure and binding site of the surface adsorbates<sup>8-10</sup>. However, the assignment of these observed core level binding energy shifts to corresponding surface moieties is extremely challenging, and experimentalists often have difficulties identifying these shifts with confidence based on the spectroscopic data only<sup>2</sup>. The dynamic nature of surface reaction on TMO catalyst and the participation of surface lattice oxygen (possible vacancy site) further complicate the situation. Hence, there are limitations to applying the experimental methods standalone in the investigation of the TMO catalyzed process.

At the same time, computational tools like density functional theory (DFT) are often used to gain insights into the electronic structure, adsorption configurations and reaction pathways of TMO catalyzed reactions. As TMOs are described as strongly correlated systems, DFT often over-

predicts the delocalization of  $d,f$ -orbital electrons and treats TMOs as conductors instead of semiconductor/insulator<sup>11</sup>. The implementation of Hubbard U-correction is the most widely used method to fix this systematic error, due to the DFT+U method's add-on nature and little additional computational cost. Hubbard U-correction is a net penalty function, which improves the occupancy of certain orbitals by forcing electron localization, restricting the amount of delocalization down by standard DFT method and restoring the insulating nature of TMO<sup>2,12-14</sup>.

However, the choice of appropriate U value for the specific system is also a challenge. The U values are commonly determined by empirical fitting of the bulk material properties (ex. lattice parameter, band gap), which cannot correctly reproduce surface properties such as surface-adsorbate interactions<sup>3</sup>. In literature, U values are also be determined by the constrained random phase approximation (cRPA) method<sup>15</sup> or constrained DFT linear-response method<sup>16</sup>. These methods mostly focus on successfully representing the bulk TMO yet may fail on application to surface-catalyzed reactions<sup>2,14</sup>. In Chapter 2, we will discuss in detail previous published investigations on the effect of U value on the computational result and how the commonly used, bulk-property optimized U values fail to reproduce surface properties of TMOs. Recently, *Trinh et al.*<sup>2</sup> proposed a synergistic approach combining experimental XPS and computational DFT+U techniques, the surface specific U value for CuO is determined as 4eV and the surface adsorbates corresponding to the experimentally observed core level binding energy shifts are identified at the same time. This surface property optimized U value of 4eV could successfully predict the hydrogen adsorption energy on CuO surface, as reported by *Bhola et al.*<sup>1</sup>.

This thesis is organized as follows: In Chapter 2, literature review is performed on previous experimental XPS and computational DFT+U investigations on TMO catalyst surfaces. Chapter 3 describes in detail the computational methods used in this thesis, including the formulation of DFT+U. Chapter 4 demonstrates the synergistic application of XPS and DFT+U methods, in which that surface specific U value for TMO could be determined based on experimental XPS results and the unidentified surface adsorbates corresponding to XPS shifts could be assigned, concurrently. NiO and Co<sub>3</sub>O<sub>4</sub> were chosen as sample TMO in this investigation as they are widely used in industrial catalytic processes<sup>17-23</sup>, like upgrading biomass, converting hydrocarbons into valuable chemicals, and producing syngas. The objective of this investigation is to simultaneously determine surface-specific U values as well as the identification of

adsorbates on the surface which correspond to experimental XPS core level binding energy shifts. The surface-specific  $U$  value determined in the work could be used for future DFT calculations, to capture the correct free energy barriers and reaction free energies for TMO catalyzed reactions. Meanwhile, the assignment of experimental XPS core level binding energy shifts to their respective adsorbates could be extended to advanced XPS techniques such as in-situ/operando XPS, to identify the key surface adsorbates or reaction intermediates. In Chapter 5, we first introduce the experimental work done by our collaborator regarding low-temperature, water-assisted tandem demethylenation of benzyl alcohol to phenol on CuO. Then, DFT+ $U$  calculations were performed with appropriate surface specific  $U$  value to i) elucidate the detailed reaction mechanism and compute activation free energy barriers and reaction free energies of the catalytic conversion of benzyl alcohol to phenol; ii) investigate the dissociation of water on the catalyst surface and the role of water and  $H_2O_2$  in the reaction; iii) confirm the postulated reaction mechanism of the catalytic conversion of benzaldehyde and *para*-hydroxy-benzyl alcohol, in line with the experiments performed in the presence of  $H_2O_2$  under silent conditions; and iv) elucidate the formation mechanism of the side product, ethylene glycol. We demonstrate that using a sonochemically synthesized CuO catalyst and water at 25 °C, benzyl alcohol oxidation reaction can be systematically steered towards a tandem demethylenation to form phenol with a synergistic experimental and theoretical methods. Chapter 6 concludes this thesis and summarizes the findings and results.

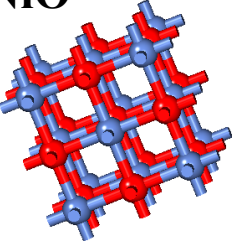
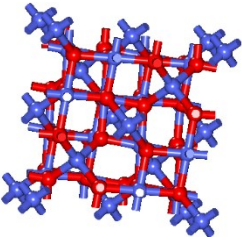
## 2. Literature Survey

In Section 2.1, we reviewed previous literature and spectroscopic data on NiO and Co<sub>3</sub>O<sub>4</sub>. As we noticed that experimentalists have difficulties assigning the observed XPS shifts, DFT can calculate shifts for different adsorbates and help assign these shifts. However, DFT prediction of XPS shifts is not reliable without a proper U value benchmarked based on TMO surface properties. Section 2.2 includes previous works showing the bulk U values that fail to capture and predict the surface properties of TMO. In Section 2.3, previous computational DFT+U literature on CuO, NiO and Co<sub>3</sub>O<sub>4</sub> is discussed and analyzed, as they will be further investigated in later chapters as sample TMO catalysts. In Section 2.4, the importance of sonochemistry combined with computational tools on TMO is discussed.

### 2.1 Previously reported experimental XPS core level binding energy shifts

As discussed in previous chapter, the assignment of observed core level binding energy shifts to surface species is extremely challenging, and experimentalists often have difficulties identifying these shifts with confidence based on the spectroscopic data only<sup>2</sup>. We reviewed literature and spectroscopic data to the best of our ability for NiO and Co<sub>3</sub>O<sub>4</sub>. Table 2.1 presents the commonly reported O1s core level binding energy shifts on both catalytic surfaces and interestingly, we noticed that there is good agreement as there are certain core level binding energy shifts reported among different studies. For NiO O1s, those shifts are at +1.8eV, +2.2eV and +3.6eV<sup>24-36</sup>, and for Co<sub>3</sub>O<sub>4</sub>, the commonly reported O1s XPS core level binding energy shifts are at +1.5eV and +2.6eV<sup>37-51</sup>. However, there is disagreement in the assignment of these shifts. For example, Wulser et al.<sup>27</sup> suggested that +1.8eV shift corresponds to the surface adsorbed hydroxyl group, while Biesinger et al.<sup>34</sup> assigned the very same shift to the vacancy site. Table 2.1 also summarized the assignment of all these shifts respectively from previous studies, further showing the arbitrariness and contradictions in assigning these shifts. These commonly reported XPS core level binding energy shifts are used as a gauge to determine the surface-specific U value for TMOs later.

Table 2.1. Previously reported O1s core level binding energy shifts and corresponding surface adsorbates assigned.

Unit cell model	Previous reported XPS O1s core level binding energy shifts (eV)	Possible corresponding surface adsorbates previously reported
<b>NiO</b> 	+1.8eV	Adsorbed H, adsorbed OH, under-coordinated lattice oxygen (Ni vacancy)
	+2.2eV	Adsorbed H, adsorbed OH, adsorbed O <sub>2</sub> or O atom, O defect
	+3.6eV	Adsorbed O, adsorbed O <sub>2</sub> , adsorbed carbonate species, adsorbed CO or CO <sub>2</sub>
<b>Co<sub>3</sub>O<sub>4</sub></b> 	+1.5eV	Adsorbed OH, under-coordinated lattice oxygen (Co vacancy), O defect, surface adsorbed O atom
	+2.6eV	O defect, under-coordinated lattice oxygen (Co vacancy), adsorbed carbonate species, adsorbed O <sub>2</sub>

## 2.2 Examples of how the bulk U values fail to capture/predict surface properties

DFT+U method is widely used for computational investigations on TMO surface catalyzed reactions. However, most studies chose their U values only based on representing the bulk TMO, ignoring that the bulk-property optimized U values are not appropriate for surface catalyzed reactions<sup>2,14</sup>. In recent years, more and more researchers noticed this problem of the DFT+U with bulk U value fails to reproduce or predict the experimental observations. For example, *Bennett et al.*<sup>52</sup> showed that the choice of U value for CeO<sub>2</sub> affected the adsorption energies of different species differently, and stated that the choice of U value would influence not only the quantitative adsorption energy, but also the qualitative thermodynamic reaction profile for TMO surface catalyzed reactions. *Huang et al.*<sup>53</sup> also noticed this problem and showed that the choice of U value could be improved with the inclusion of adsorbate-surface interactions and adsorption

configurations on CeO<sub>2</sub> surface. Moreover, *Hu et al.*<sup>54</sup> reported that the bulk property optimized U value of 5.9eV is not able to correctly match RPA (random phase approximation) prediction of H and CO adsorption energy on Co<sub>3</sub>O<sub>4</sub> surface. Recently, *Bhola et al.*<sup>1</sup> and *Trinh et al.*<sup>2</sup> conducted a thorough investigation regarding the U value choice on CuO, and they showed a U value of 4eV could describe the surface much better compared to bulk-property optimized value (details will be discussed in next section). The synergistic approach they developed to combine experimental and computational methods is adopted by this study, and to extend on other TMO systems.

### 2.3 Previous investigations of U values on CuO, NiO and Co<sub>3</sub>O<sub>4</sub>

The U value of 7eV for CuO is well established in the literature and it is obtained by fitting of bulk physical properties like band gap, magnetic momentum, and bulk lattice parameter<sup>1,2,55-59</sup>. However, there are limitations if U value is only benchmarked on bulk TMOs without any consideration to adsorbate-surface interaction and surface chemistry during the reaction. *Bhola et al.*<sup>1</sup> emphasized the importance of properly benchmarking U value. Throughout an entire reaction, some reaction steps might be weakly affected by the choice of the U value, for example, physisorption, weakly interaction with limited or no charge transfer. However, the adsorption energies of reaction intermediates or products, and the energy of vacancy formation or oxygen consumption are strongly dependent on the choice of U value. Hence, to accurately predict the energetics of entire TMO catalyzed reaction, an appropriate U value is required. Hydrogen molecule is chosen as probe molecule since the adsorption energy of hydrogen is a suitable descriptor for the reactivity of TMO mediated hydrogen abstraction reactions in hydrocarbons<sup>60-64</sup>. According to *Bhola et al.*<sup>1</sup>, the theoretical prediction on hydrogen adsorption free energy on CuO changes over 100kJ/mol as the U value changes from 0 to 9eV, as shown in Figure 2.1a. As the bulk property optimized U value of 7eV underestimates the adsorption energy of hydrogen, a lowered U value around 4-5eV is more appropriate to reproduce the experimentally measured adsorption energy of hydrogen.

A synergistic approach combining experimental and computational tools was proposed by *Trinh et al.*<sup>2</sup>. The combination of the XPS and DFT+U techniques, can be used to determine the surface-specific U value, while simultaneously identify unknown adsorbed surface moieties on



the TMO surface. This synergistic approach was performed on CuO (111) and compared the experimental XPS with DFT+U calculated O1s core level binding energy shifts of various possible adsorbates on the CuO (111) surface. Figure 2.1b<sup>2</sup> shows the DFT predicted core level binding energy shift for oxygen in adsorbed HCO<sub>2</sub> at different U values on CuO (111) surface. The U value range of 4 to 4.5eV is able to reproduce the experimental XPS O 1s core level binding energy correctly while the bulk property optimized and commonly used U value of 7 eV fails. There is a good agreement between the adsorption energy determined U value and XPS determined U value, indicating that the appropriate surface U value benchmarked by either method is able to capture the various surface-adsorbate interactions, chemical states and energetics for elementary reaction steps on the specific catalyst surface accurately. Hence, in order to properly investigate a TMO catalyzed reaction, it is necessary to evaluate the appropriate U value based on the surface-specific properties, instead of bulk properties.

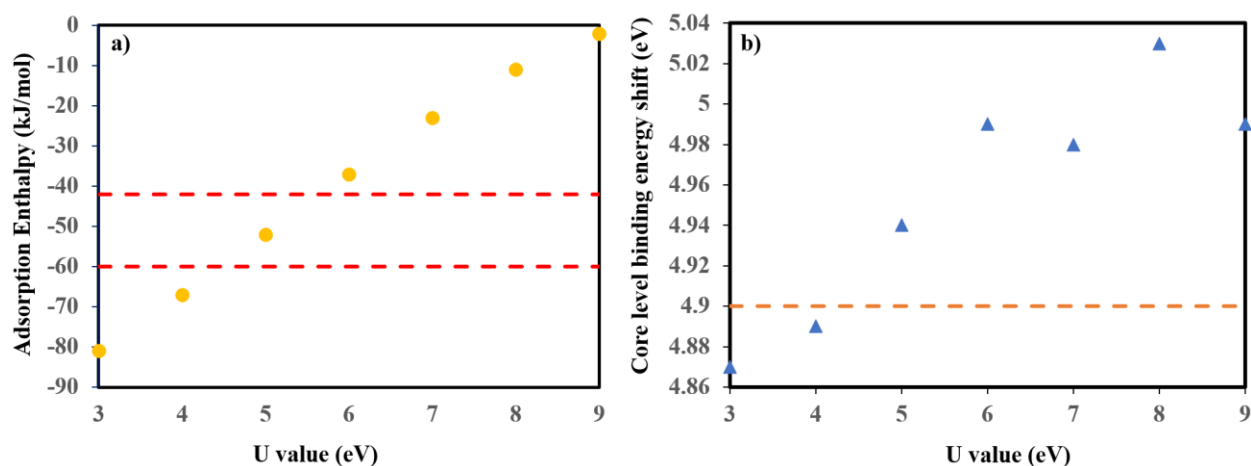


Figure 2.1 a) DFT predicted hydrogen adsorption enthalpy at different U values and b) DFT predicted core level binding energy shift for oxygen in adsHCO<sub>2</sub> at different U values, both on CuO (111) surface. Dash lines represent the experimentally measured adsorption enthalpy and core level binding energy shifts, respectively. Data point are adapted from *Bhola et al.*<sup>1</sup> and *Trinh et al.*<sup>2</sup>.

We adopted the synergistic approach suggested by Trinh et al.<sup>2</sup> and performed DFT+U calculation on NiO and Co<sub>3</sub>O<sub>4</sub> surfaces with different choices of U values. NiO is a TMO with low price, large band gap and good thermal and chemical stability. It is of interest for various engineering applications such as batteries, fuel cells, electrochemical capacitances, and catalysts or catalyst supports, such as oxygen evolution reaction (OER), chemical looping combustion (CLC) and chemical looping reforming (CLR)<sup>64-69</sup>. A bulk property optimized U value of 5.3eV

is well established in the literature and commonly used in various studies<sup>70-73</sup> for NiO. On the other hand, Co<sub>3</sub>O<sub>4</sub> is a relatively cheap and active reducible TMO commonly utilized in gas sensors, batteries, energy storage and catalysts or catalyst supports for oxygen evolution reactions, NO decomposition, CO oxidation<sup>74-82</sup>. For Co<sub>3</sub>O<sub>4</sub>, there is disagreement on the U value choice among the community. There are studies that use 5.9eV<sup>54,83-85</sup>, some others use a lower value from 2.0-3.5eV<sup>86-88</sup>, and some suggest that the U value should be set as 4.4eV/6.6eV for Co<sup>2+</sup> and Co<sup>3+</sup>, respectively<sup>84,89</sup>. Selcuk and Selloni<sup>87</sup> suggest that 3.0eV is a better overall description of the electronic structure and surface reactivity yet 5.9eV is better suited to magnetic properties; *Hu et al.*<sup>54</sup> reported that the bulk property optimized U value of 5.9eV is not able to correctly predict the reaction performance of Co<sub>3</sub>O<sub>4</sub>, and they suggest a bi-U strategy combining surface U of 1.35eV and bulk U of 3.5eV to reproduce RPA (random phase approximation) results. This confusion in the determination of U value further reinforces the importance of benchmarking U value, with the combination of experimental and computational techniques on NiO and Co<sub>3</sub>O<sub>4</sub> surface.

In Chapter 4, the synergistic approach developed by Trinh et al.<sup>2</sup> is adopted on NiO and Co<sub>3</sub>O<sub>4</sub> to investigate their proper surface specific U value based on experimental XPS results and assign the surface adsorbates to XPS shifts based on DFT+U calculations. In Chapter 5, 4.0eV is used as the proper surface U value for CuO, to investigate low temperature, ultrasonic-assisted benzyl alcohol conversion to phenol.

## 2.4 Previous Studies of Sonochemistry on TMO catalysis

Sonochemistry, particularly high frequency ultrasound (>100 kHz), has been widely used as an unconventional activation technique for material synthesis<sup>90,91</sup>, environmental remediation<sup>92</sup> and food processing<sup>93</sup>, where acoustic cavitation-induced oxygenated radicals (e.g., •OH) act as initiators to trigger chemical reactions. Recently, the use of high frequency ultrasound is undergoing a sort of renaissance as an alternative activation tool in synthetic chemistry<sup>94-96</sup>. For instance, High frequency ultrasound was used as a combined strategy with metal ions to convert phenol and phenyl derivatives into polyphenols<sup>97</sup>. The technological potential of high frequency

ultrasound in directly altering products formations in synthetic chemistry has been broadly demonstrated and documented in literature<sup>90,98</sup>. Inspired by these works and in-line with our efforts in harnessing the chemical potential of sonochemistry in synergy with catalysis for organic reactions, we revisited the widely studied benzyl alcohol oxidation reaction<sup>99-102</sup>, from a radically different perspective to gain first-hand insights into the mechanisms involved in its transformation to other aromatic products of industrial importance. Meanwhile, DFT+U is often used as the computational tool to investigate TMO catalyzed reactions under ultrasound conditions, such as glycerol oxidation on CuO<sup>103</sup>, cellulose oxidation on Au supported Fe<sub>2</sub>O<sub>3</sub><sup>104</sup>, and glucose oxidation on CuO<sup>105</sup>. The computational tools can calculate the free energy barrier and reaction free energy of each reaction steps, verify the experimental hypothesis and unravel reaction mechanisms and the role of TMO catalyst.

In Chapter 5, we demonstrate for the first time through synergistic experimental and theoretical investigations how the popular benzyl alcohol oxidation reaction can be systematically steered towards tandem demethylenation and hydroxylation via an alternate activation mechanism, with selectivity up to 80 % towards phenol. This is achieved using the synergy between a sonochemically synthesized cupric oxide catalyst and ultrasonically generated *in-situ* H<sub>2</sub>O<sub>2</sub> from water, at ambient conditions (25 °C), without any external oxidising agent. This work would find application in the conversion of lignin components into diverse hydroxy aromatic building blocks and generally offers potential for new, mild methods for efficient unmasking of phenol.

### 3. Methodology

Section 3.1 discusses the basic formulation of DFT. Section 3.2 discusses the implementation of Hubbard U correction to traditional DFT method for strongly correlated systems. Section 3.3 includes the computational methods used in Chapter 4 and 5.

#### 3.1 The Formulation of DFT

Density functional theory (DFT) is a popular computational method used in catalyst design and development. Comparing with the wave-function approach, DFT could describe the system by connecting the electron density with the energy of the system while the complexity and computational cost of a wave function increases exponentially with the size of a system. The basis of DFT is that the one-to-one correspondence between the electron density and the ground state electronic energy of the system, stated by Hohenberg and Kohn<sup>106</sup> in 1964. They demonstrated the basic idea of how to calculate the ground state energy of a multi-electron system using the variational principle, without having to resort to calculate the wave function. As the Schrodinger wave equation for an N electron system is given as

$$\left[ \sum_i^N -\frac{1}{2} \nabla^2 - \sum_i^N \sum_j^N \frac{1}{r_{ij}} + \sum_i^N \frac{Z}{r_i} \right] \Psi = E \Psi \quad (\text{Eqn.1})$$

And the ground state of electronic density of the system can be calculated as

$$\rho(r_1) = N \int dx_1 d2 \dots dN \Psi^*(r_1, x_1, 2, \dots, N) \Psi(r_1, x_1, 2, \dots, N) \quad (\text{Eqn.2})$$

Then, the wave function,  $\Psi$ , the potential,  $v$ , and the ground state density,  $\rho$ , could be expressed as

$$\Psi = \Psi(v[\rho]) = \Psi(\rho) \quad (\text{Eqn.3})$$

According to the variational principle, the energy of the system can be calculated as,

$$E = \min_{\Psi} \langle \Psi | H | \Psi \rangle = \min_{\rho} \langle \Psi[\rho] | H | \Psi[\rho] \rangle = \min_{\rho} \langle \Psi[\rho] | T + v + V_{ee} | \Psi[\rho] \rangle \quad (\text{Eqn.4})$$

where  $T = \frac{-\nabla^2}{2}$ ,  $v = -\frac{Z}{r}$  and  $V_{ee} = \frac{1}{r_{ee}}$

Then, Eqn. 4 can be separated as:

$$E = \min_{\rho} \{ \langle \Psi[\rho] | v | \Psi[\rho] \rangle + \langle \Psi[\rho] | T + V_{ee} | \Psi[\rho] \rangle \} = \min_{\rho} \{ \int d^3r \rho(r) v(r) + F[\rho] \} \quad (\text{Eqn.5})$$

The energy is thus minimized over the density and not over the wave function.

The inverse mapping of density on potential is also valid, by Thomas<sup>107</sup> and Fermi<sup>108</sup>, provided a way to calculate the energy of a non-interacting system by replacing the wave function with electron density:

$$\begin{aligned} E &= \sum_{i=1}^N \int d^3r \chi_i(\vec{r}) \left( -\frac{\nabla^2}{2} \right) \chi_i(\vec{r}) + \sum_{i=1}^N \int d^3r \chi_i(\vec{r}) \chi_i(\vec{r}) v(\vec{r}) \\ &= \sum_{i=1}^N \int d^3r \chi_i(\vec{r}) \left( -\frac{\nabla^2}{2} \right) \chi_i(\vec{r}) + \sum_{i=1}^N \int d^3r \rho(\vec{r}) v(\vec{r}) \end{aligned} \quad (\text{Eqn. 6})$$

As shown in Eqn.6, Thomas-Fermi replaced the wave function with the electronic density. They also showed that the kinetic energy part of a homogenous electron gas is given as:

$$T_s = \frac{3}{10} (3\pi^2)^{\frac{2}{3}} \int d^3r \rho^{\frac{5}{3}}(\vec{r}) \quad (\text{Eqn.7})$$

Hence according to Thomas-Fermi<sup>107,108</sup> approach, the energy of the non-interacting system can be given in terms of the electron density as,

$$E(\rho) = \sum_{i=1}^N \frac{3}{10} (3\pi^2)^{\frac{2}{3}} \int d^3r \rho^{\frac{5}{3}}(\vec{r}) + \int d^3r \rho(\vec{r}) v(\vec{r}) \quad (\text{Eqn.8})$$

This Thomas-Fermi<sup>107,108</sup> approach of calculating the kinetic energy part of the non-interacting system of electrons is used to develop a scheme to evaluate the functional  $F[\rho]$ .

In 1965, Kohn and Sham<sup>109</sup> suggested that the electron kinetic energy should be calculated from an auxiliary set of orbitals used for representing the electron density. The main drawback of previous orbital-free DFT models is the poor representation of the kinetic energy, and Kohn-Sham density functional theory (KS-DFT) splits the kinetic energy functional into a term can be calculated exactly and a small correction term. KS-DFT introduces a fictious non-interacting system which Hamiltonian can be given as

$$h_{ks} = -\frac{1}{2}\nabla^2 + v_{ks}(\vec{r}) \quad (\text{Eqn.9})$$

The first term in Eqn. 9 represents the kinetic energy of the electrons and the second term represents the potential energy of electron-nucleus interactions. For such an orbital corresponding to the above Hamiltonian, is often referred as KS orbital,  $\chi_{ks}$ . The kinetic energy of the non-interacting system is

$$T_S = \langle \chi_{ks} | T | \chi_{ks} \rangle \quad (\text{Eqn. 10})$$

For the actual wave function of the system,  $\Psi$ , the ground state electronic energy could be expressed as

$$\begin{aligned} E &= \langle \Psi | T + v + V_{ee} | \Psi \rangle = \langle \Psi | T | \Psi \rangle + \int d^3r \rho(\vec{r}) v(\vec{r}) + \langle \Psi | V_{ee} | \Psi \rangle \\ &= T_S + \int d^3r \rho(\vec{r}) v(\vec{r}) + U[\rho] - E_{XC} \end{aligned} \quad (\text{Eqn. 11})$$

where  $U[\rho] = \frac{1}{2} \int d^3r d^3r' \frac{\rho(\vec{r})\rho(\vec{r}')}{|\vec{r}-\vec{r}'|}$  and  $E_{XC} = T_K - T_S + \langle \Psi | V_{ee} | \Psi \rangle - U[\rho]$ . As  $T_S$  is the kinetic energy which can be calculated using KS orbitals. The “exchange-correlation” functional term,  $E_{XC}$ , is the only undetermined functional of electronic density which needs to be approximated, and it is about 10% of the total energy.  $E_{XC}$  accounts for the difference between the actual electronic kinetic energy of the system and the KS non-interacting electronic kinetic energy, and the difference between exact electron-electron interaction energy and  $U[\rho]$ . Typically the kinetic energy correlation part is minimal and many functional do not compute the kinetic energy correction explicitly and some use empirical parameters for this correction. However, the electron-electron interaction correction is relatively significant. The two common approximations for  $E_{XC}$  are the local density approximation (LDA) and the generalized gradient approximation (GGA). LDA treats the exchange correlation energy density at every point in a system will be the same as that exchange-correlation energy density of the interacting uniform electron gas of the same electron density as in that position. GGA is an improvement over LDA with the implementation of the gradient correction as

$$E_{XC}^{GGA} = \int d^3r g(\rho, \nabla\rho) \quad (\text{Eqn.12})$$

Since Perdew-Burke-Ernzerhof (PBE) functional<sup>110</sup> is used throughout this thesis, only the formulation of GGA will be discussed. In PBE functional,  $E_{XC}$  is given as is separated into exchange and correlation part and the correlation term is given as

$$E_C^{GGA} = \int \rho [\epsilon_c(r_s, \zeta) + H(r_s, \zeta, t)] d^3r \quad (\text{Eqn.13})$$

Where  $t$  is the dimensionless density gradient given as  $t = \frac{|\nabla\rho|}{2\phi k_s \rho}$ ,  $\phi = \frac{(1+\zeta)^{\frac{2}{3}} + (1-\zeta)^{\frac{2}{3}}}{2}$ ,  $\zeta = \frac{\rho_\alpha - \rho_\beta}{\rho_\alpha + \rho_\beta}$ ,

$$k_s = \sqrt{\frac{4(3\pi^2\rho)^{\frac{1}{3}}}{\pi(\frac{\hbar^2}{me^2})}} \quad , \quad H = \left(\frac{e^2}{\hbar^2}\right) 0.031091\phi^3 \ln\left(1 + \frac{0.066725}{0.031091} t^2 \left[\frac{1+\bar{A}t^2}{1+\bar{A}t^2+\bar{A}^2t^4}\right]\right) \quad ,$$

$$\bar{A} = \frac{0.066725}{0.031091} \left[ \exp\left\{\frac{-\epsilon_c}{\frac{e^2}{\hbar^2} \frac{1}{me^2}}\right\} - 1 \right]^{-1} . \text{ The exchange energy term is defined as}$$

$$E_X^{GGA} = \int \rho \epsilon_x(\rho) F_X(s) d^3r \quad (\text{Eqn.14})$$

Where  $s$  is another type of reduced density gradient given as  $\left(\frac{r_s me^2}{\hbar^2}\right)^{0.5} \phi t / 1.2277$  and  $F_X(s) =$

$$1 + 0.0804 - \frac{0.804}{1 + \frac{0.2195s^2}{0.804}}$$

When DFT is applied to repeated periodic system such as crystal and catalyst surface, periodic conditions to the unit cell can be used to reduce the computational cost. If the cell is defined by vector  $a_1, a_2$  and  $a_3$ , then its volume is  $\Omega = a_1 \cdot (a_2 \times a_3)$ , the general lattice vectors are integer multiples of these vectors as

$$\bar{L} = N_1 a_1 + N_2 a_2 + N_3 a_3 \quad (\text{Eqn. 15})$$

In such case, the effective potential also has periodicity which is

$$v_{eff}(\vec{r} + \bar{L}) = v_{eff}(\vec{r}) \quad (\text{Eqn. 16})$$

Such periodic potential can be expanded as a Fourier series. Due to the nature of the Fourier transformation,  $v_{eff}(\vec{r})$  is transformed from a real space periodic potential into a Fourier space potential. Bloch's theorem states that if  $v(\vec{r})$  is a periodic potential, then the wave function of a

one electron Hamiltonian of the form  $-\frac{1}{2}\nabla^2 + v(\vec{r})$  is given as planewave times a function with the same periodicity as the potential. Hence, the KS-DFT equations can be rewritten as

$$\left(-\frac{1}{2}\nabla^2 + v_{k_s}(\vec{r})\right)\Psi_{\vec{k}}(\vec{r}) = \epsilon_{\vec{k}}\Psi_{\vec{k}}(\vec{r}) \quad (\text{Eqn. 17})$$

And the electron density is given as

$$\rho(\vec{r}) = 2 \frac{\Omega}{(2\pi^3)} \int |\Psi_{\vec{k}}(\vec{r})|^2 \delta(E_F - \epsilon_{\vec{k}}) d^3k \quad (\text{Eqn.18})$$

Factor 2 in Eqn. 18 is to take into account both the electron spins and  $\delta$  is the step function which 1 for positive and 0 for negative function arguments. The integration in Eqn. 18 is over the Brillouin zone, which means the primitive cell in the reciprocal space. Hence, only a small periodic cell is needed for a extended system with extended number of electrons. Since the electronic wave function at k-points close to each other will be similar, it is also possible to replace the above integral as a discrete sum over limited number of k-points. The error due to this approximation can be minimized by using large number of k-points<sup>11</sup>. In this work, the convergence tests regarding to the choice of k-point were performed and will be discussed later. For practical application of planewaves approach, a solution to the nodal structure of valence wave functions problem needs to be addressed. Therefore, pseudopotentials are used to replace the electron-nuclear potential. Since this pseudopotential eradicates the core electrons from the system, it is very important that the pseudopotential takes into account the electron-nucleus interaction as if shielded the core electrons and the electron-electron interaction between the valence and core electrons. Hence the pseudopotential is angular moment dependent as well. Also, the contribution of core electrons to chemical bonding is negligible and only the valence electrons play significant part in it. Outside a certain cut-off radius, the pseudopotential matches the true potential of the system, and the pseudo-wave function matches the true wave function of the system, as shown in Figure 3.1. The core electrons play an important part in the calculation of the total energy though and this implies that the removal of core electrons will also result in lower energy differences between different configurations, thereby reducing the costs in achieving the required accuracy. Ultra-soft pseudopotentials are used throughout this work.



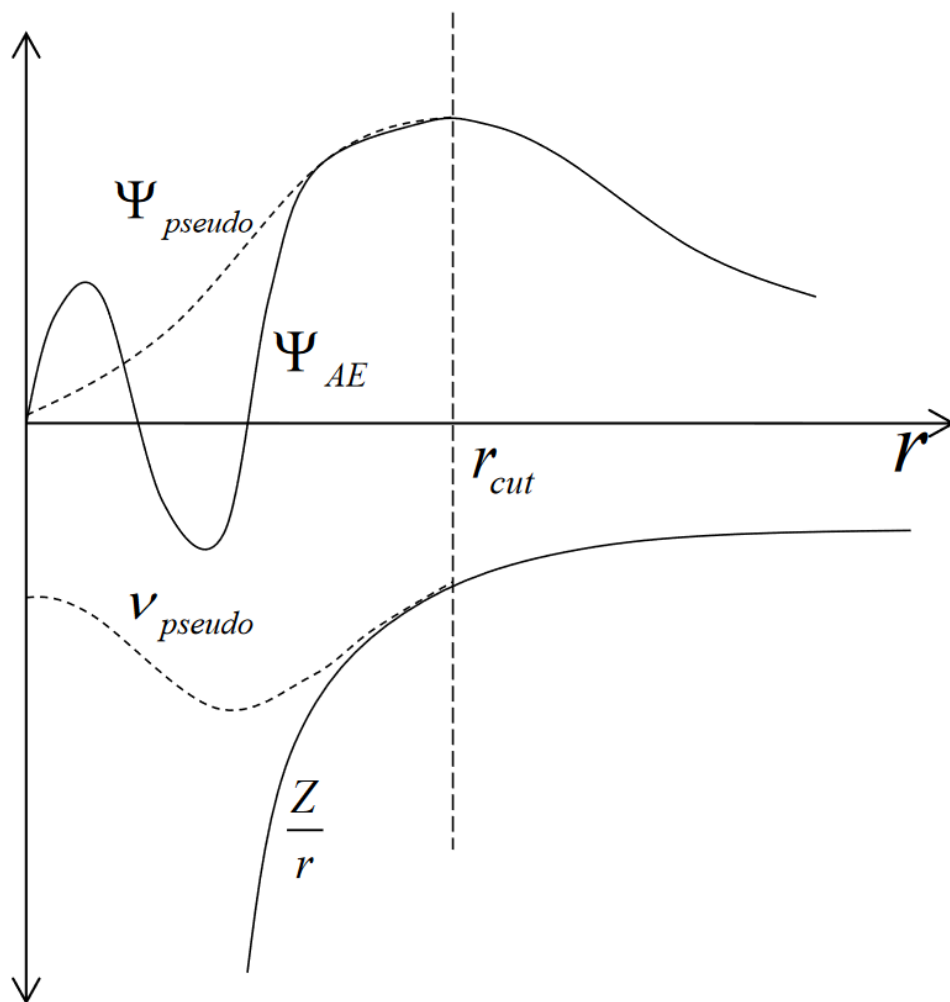


Figure 3.1. The wave function of the system under the nuclear potential and under the pseudopotential

### 3.2 The implementation of Hubbard U-correction in DFT+U

As discussed in the previous section, as DFT is one of the most efficient computational tools, yet the accuracy of DFT dramatically fails in the prediction of electronic and other related properties of semiconductors<sup>112</sup>. TMOs are often described as strongly correlated systems, and DFT describes the correlated systems with over-prediction on the delocalization of  $d,f$ -orbital electrons and treats TMOs as conductors instead of semiconductor/insulator<sup>11,13,113</sup>. The reason behind this systematic error is due to the inability of the approximated exchange-correlation

functional to completely cancel out the electronic self-interaction contained in the Hartree term, hence, electrons are there that can induce added self-interaction, ultimately causing the over-delocalization<sup>13,113</sup>. The implementation of Hubbard U-correction is the most widely used method to fix this systematic error, introduced and developed by Anisimov et al.<sup>13</sup> and Dudarev et al.<sup>12</sup> The total energy of the system predicted by the DFT+U method is given as:

$$E_{DFT+U} = E_{DFT} + \frac{U-J}{2} \sum_{\sigma} n_{m,\sigma} - n_{m,\sigma}^2 \quad (\text{Eqn. 19})$$

Where  $n$  is the atomic-orbital occupation number,  $m$  is the orbital momentum,  $\sigma$  is a spin index,  $U$  is the on-site Coulomb repulsion and  $J$  represents the exchange interaction. The Hubbard U-correction is often referred to as effective U value<sup>12</sup>,  $U_{eff} = U - J$ . This Hubbard U-correction represents a net penalty function, which improves the occupancy of certain orbitals by forcing electron localization, restricts the amount of delocalization down by the standard DFT method and restores the insulating nature of TMO<sup>2,12-14</sup>. According to Rohrbach et al.<sup>114</sup>, a larger U value is required to compensate for the binding characteristic of LDA, which will lead to widening of the energy gap, and DFT+U with GGA is a better choice for the functional. Therefore, in this thesis, PBE functional are chosen through the investigations. The adds-on nature and low additional consumption on computational resources make DFT+U method efficient and popular when investigating TMO systems, yet the accuracy of the results depends on the choice of U value, as discussed before.

### 3.3 Computational methods

Figure 3.2 shows the catalytic surface models for NiO(100), Co<sub>3</sub>O<sub>4</sub>(100) and CuO(111). In Chapter 4, all calculations were performed with the periodic plane-wave implementation (with the plane-wave cutoff energy of 450eV) of DFT using the Vienna Ab-initio Simulation Package (VASP)<sup>115-118</sup> with the projector augmented wave (PAW) scheme<sup>119,120</sup>. The Perdew-Burke-Ernzerhof (PBE) exchange correlation functional<sup>110</sup> was used as the Generalized gradient approximation (GGA). Gamma-centred  $3 \times 4 \times 1$  K-point sampling and within the Monkhorst-Pack scheme was used for integration over the Brillouin zone and integration was performed using the tetrahedron method with Blochl corrections for both NiO and Co<sub>3</sub>O<sub>4</sub> model<sup>1,2</sup>. The

convergence criteria for total energy and inter-atomic forces of all calculations were  $10^{-6}$  eV per unit cell and 0.01eV/Å, respectively. All TMO models were simulated by spin-polarized calculation with the most stable antiferromagnetic configurations. NiO was modelled as periodic seven-layer slab and  $\text{Co}_3\text{O}_4$  was modelled as periodic ten-layer slab, 10 Å vacuum thickness was added on top of both models to prevent the interaction between repeated periodic slabs. The detailed computational parameters' benchmarking will be discussed in Chapter 4, and it ensures that the calculated XPS shift is only related to the change in U value.

In Chapter 5, for computational investigation of sonocatalytic transformation of benzyl alcohol to phenol on CuO, according to *Bhola et al.*<sup>1</sup> and *Trinh et al.*<sup>2</sup>, the appropriate surface-specific U value should be used to predict the surface reactions, pathways, and energetics, instead of U value optimized for bulk properties. Hence, GGA+U method with the Hubbard U correction of 4.0 eV was used as it could successfully capture the surface O1s core level binding energy and experimental surface adsorption enthalpy on CuO (111) surface. In this study, CuO was modelled as periodic four-layer slabs and a 15 Å vacuum thickness above the top layer was used to prevent the interaction between repeated periodic unit cells. The top layer and the adsorbates were allowed to fully relax while the bottom two layers were fixed at the optimized bulk lattice parameters to reduce the computational cost without influencing the accuracy of simulations. The convergence criteria for total energy and interatomic forces were set to  $10^{-6}$  eV per unit cell and 0.01 eV/Å, respectively. All the calculations were performed with spin polarization as the antiferromagnetic ground state of  $\text{CuO}^2$ . The  $4 \times 3 \times 1$  Monkhorst–Pack grid was used to sample the Brillouin zone, and the tetrahedron method with Blöchl corrections was employed for all calculations. Transition states were reached using the Nudged Elastic Band (NEB) method<sup>121-124</sup> and confirmed with the vibrational frequency calculations with only one imaginary frequency. To obtain the free energies of the process, the entropy, zero-point energy and enthalpy correction were computed from statistical thermodynamics for all adsorbed structures, while those values for gas-phase molecules were taken from the standard thermodynamics NIST-JANAF table<sup>1,125,126</sup>.

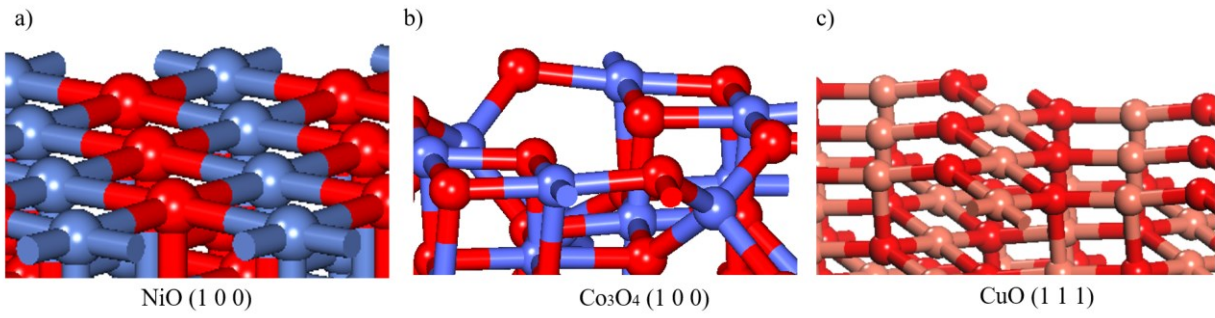


Figure 3.2 Slab model for a) NiO (100), b)  $\text{Co}_3\text{O}_4$  (100) and c) CuO (111) surface. Dark blue, light blue, salmon and red balls represent nickel (Ni), cobalt (Co), copper (Cu) and oxygen (O), atoms, respectively.

#### **4. Determining surface specific Hubbard-U corrections and identifying key adsorbates on NiO and Co<sub>3</sub>O<sub>4</sub>**

As mentioned in Chapter 2, the existing methods of determining U values mostly focus on representing the bulk TMO and fail to model surface-catalyzed reactions<sup>2,14</sup>. In this chapter, we adopted the synergistic approach suggested by Trinh et al.<sup>2</sup> and performed DFT+U calculation on NiO and Co<sub>3</sub>O<sub>4</sub> surfaces with different choices of U values. The commonly reported XPS core level binding energy shifts from literature (reported in Chapter 2) are used to determine the surface-specific U value for both TMOs, and the DFT+U calculation results could be used to determine surface adsorbates and configurations corresponding to the XPS shifts. The objective of this investigation is to simultaneously determine surface-specific U values, as well as to identify adsorbates that correspond to experimental XPS core level binding energy shifts on NiO and Co<sub>3</sub>O<sub>4</sub>. Meanwhile, the assignment of experimental XPS core level binding energy shifts to their respective adsorbates could be extended in future to advanced XPS techniques such as in-situ/operando XPS, to identify the key surface adsorbates or reaction intermediates.

##### **4.1 Benchmarking for computational parameters of NiO model**

Figure 4.1 shows the DFT+U optimized lattice parameter for NiO using different U values. The experimentally measured lattice parameter for NiO is ~4.176Å and the difference is around 1% despite the choice of the U values. The lattice parameter is optimized for every U value separately. Figure 4.2 shows the row-by-row magnetic ordering used in the simulation, and it is the most stable magnetic ordering among bulk-like, row-by-row and layer-by-layer that could be assigned to NiO(100) structure. The computational core level binding energy for atoms is very sensitive to the local environment of catalyst surface. Hence, it is important to benchmark the thickness of the slab to ensure that the atoms at the central layers are capable of representing the bulk site, which will act as reference for core level binding energy shifts. Figure 4.3 shows the convergence test for slab thickness and a seven-layer model is chosen. Other computational parameters such as energy cut-off, the choice of K-point, and energy convergence criteria are also benchmarked to ensure that the calculated XPS shift is only related to the change in U value. Hence, NiO was modelled as periodic seven-layer slabs and a 10 Å vacuum thickness above the top layer was used to prevent the interaction between repeated periodic unit cells. The top five

layers and the adsorbates were allowed to fully relax while the bottom two layers were fixed at the optimized bulk lattice parameters to reduce the computational cost without influencing the accuracy of simulations. The convergence criteria for total energy and interatomic forces were set to  $10^{-6}$  eV per unit cell and 0.01eV/A, respectively. All the calculations were performed with spin polarization as the antiferromagnetic ground state of NiO. The  $3 \times 4 \times 1$  Monkhorst–Pack grid was used to sample the Brillouin zone (convergence test for k-points data is shown in table 4.1), and the tetrahedron method with Blöchl corrections was employed for all calculations. The representation of NiO model is shown in Figure 4.4.

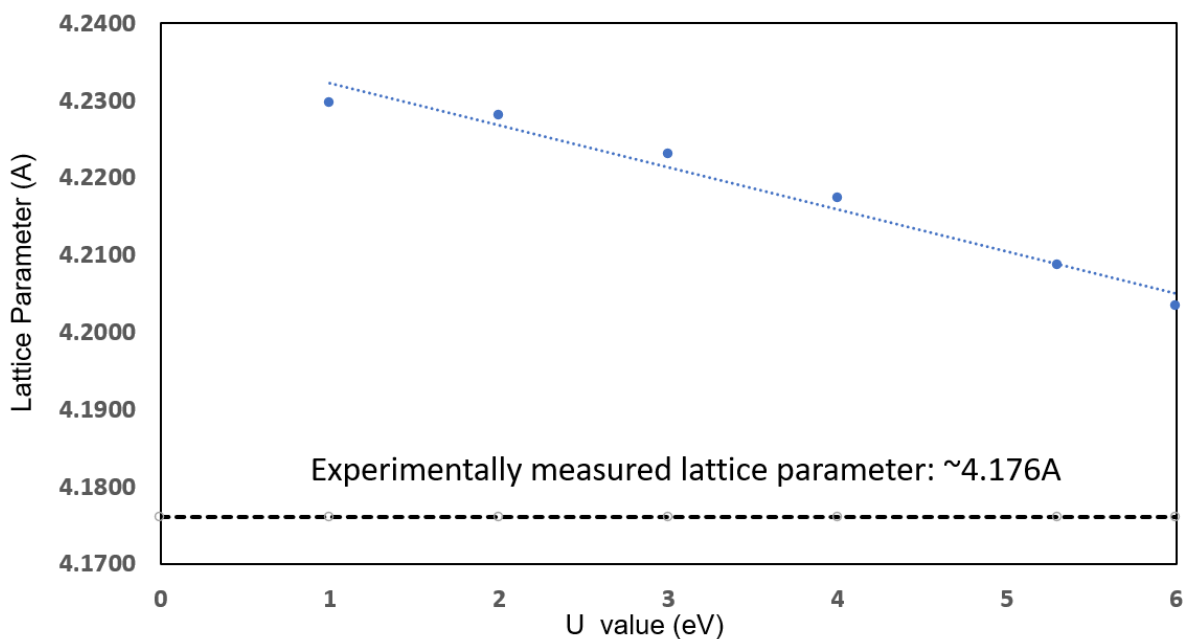


Figure 4.1. DFT+U optimized lattice parameter for NiO using different U values in comparison with experimentally measured lattice parameter

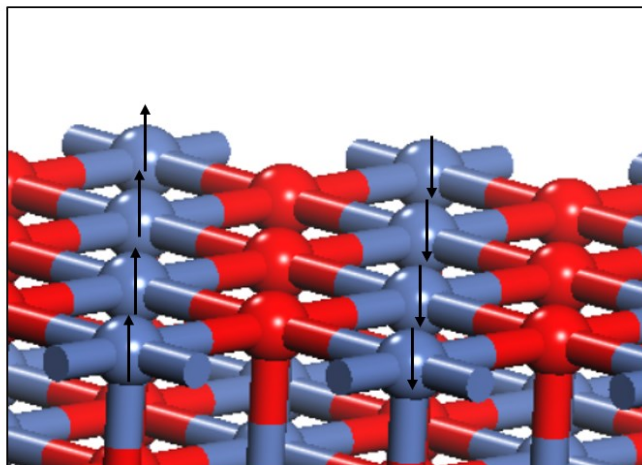


Figure 4.2. The most stable magnetic arrangement for NiO (100), showing row-by-row magnetic spin ordering (where the alternating atoms of Ni in any particular row have same magnetic spins.) The upward and downward arrows represent the positive and negative spin, respectively. Dark blue and red balls represent nickel (Ni) and oxygen (O) atoms, respectively.

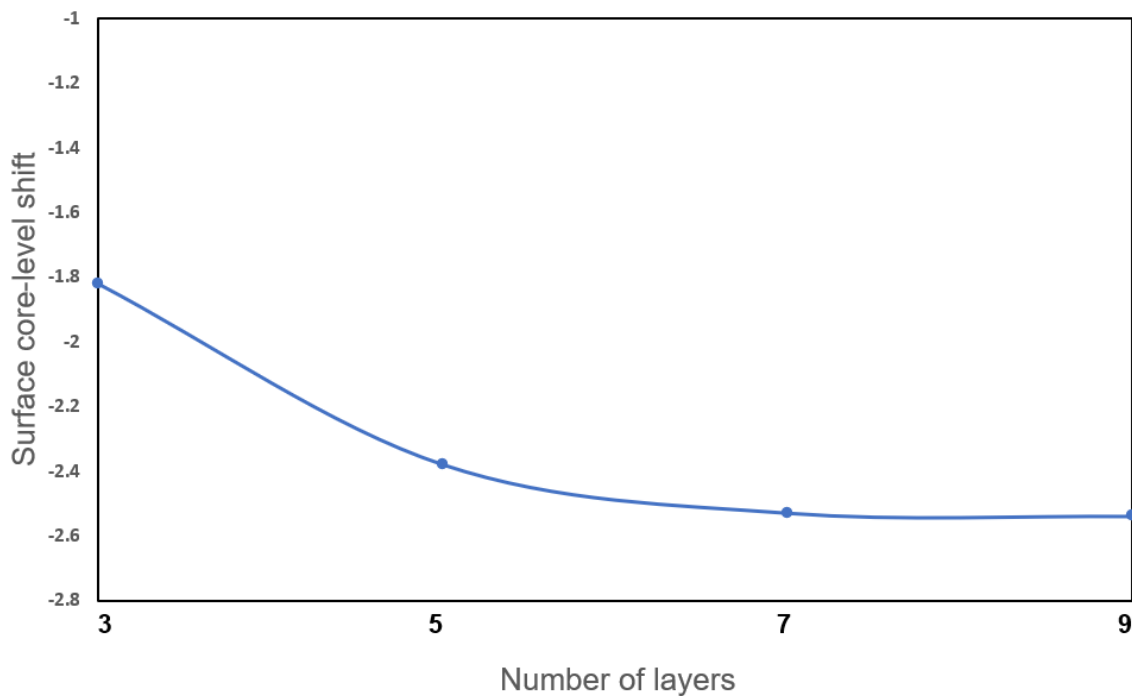


Figure 4.3. Convergence test showing the variation in calculated surface oxygen O1s core level binding energy shifts with the increasing slab thickness (number of layers) for surface oxygen on NiO(100).

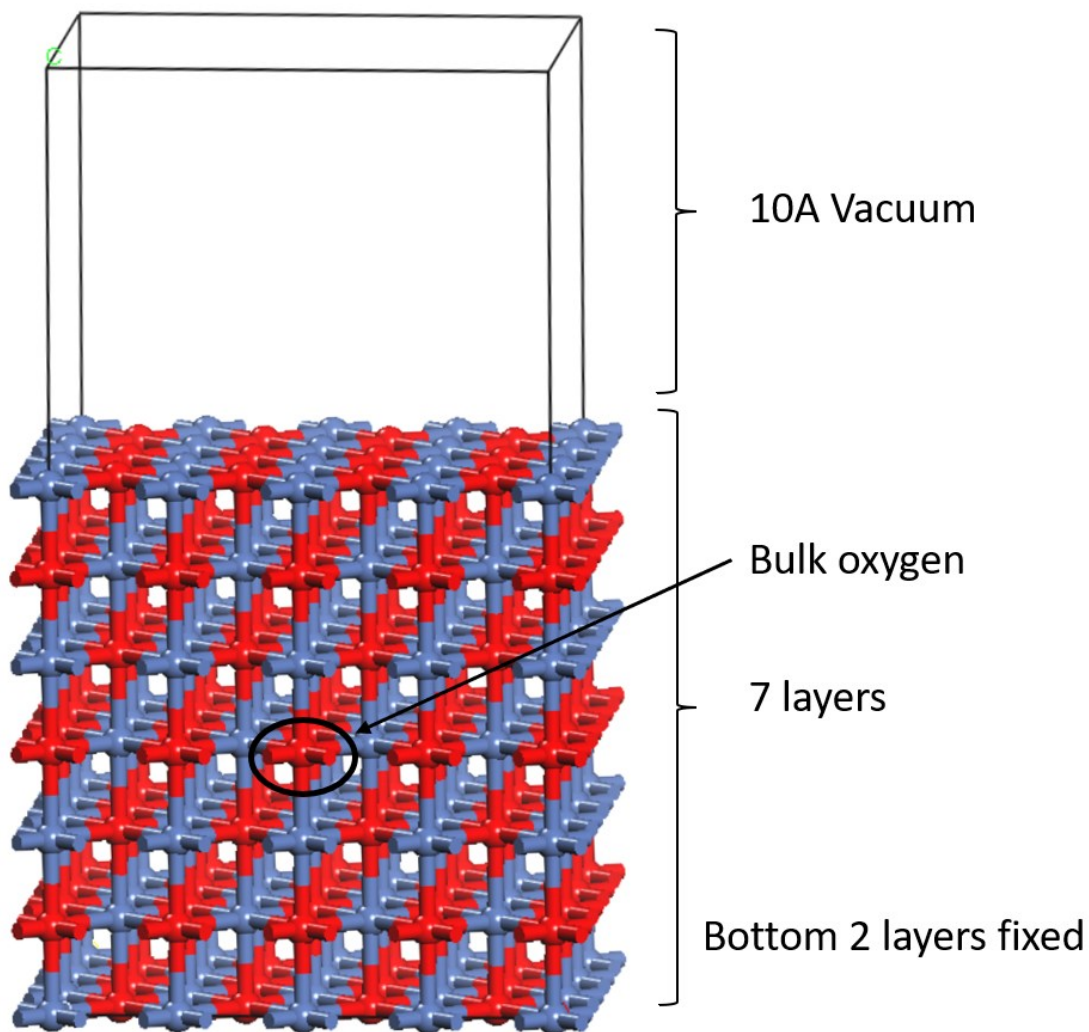


Figure 4.4. Representation of the system used to model NiO (100) surface, slab size, illustrating the number of layers and vacuum thickness. The oxygen atom in the central layers representing the bulk oxygen is highlighted. Dark blue and red balls represent nickel (Ni) and oxygen (O) atoms, respectively.



Table 4.1. The DFT calculated energy of the system of NiO with different k-point choices

KPOINT	Energy of the system (eV)
221	-859.011
241	-859.024
441	-859.024
331	-859.023
<b>341</b>	<b>-859.024</b>

#### 4.2 Benchmarking for computational parameters of Co<sub>3</sub>O<sub>4</sub> model

Similar benchmarking procedure were performed on Co<sub>3</sub>O<sub>4</sub> as well. Figure 4.5 shows the DFT calculated lattice parameter at various U value. Figure 4.6 shows the most stable magnetic arrangement. Figure 4.7 shows the convergence test to determine the thickness of the slab. Figure 4.8 shows the representation of Co<sub>3</sub>O<sub>4</sub> model used. The terminal layer of Co<sub>3</sub>O<sub>4</sub> (100) contains four cobalt atoms and eight oxygen atoms, and this termination is slightly more stable compared to the alternative, which only contains two cobalt atoms, according our DFT calculations. In summary, Co<sub>3</sub>O<sub>4</sub> was modelled as periodic ten-layer slabs and a 10 Å vacuum thickness above the top layer was used to prevent the interaction between repeated periodic unit cells. The top seven layers and the adsorbates were allowed to fully relax while the bottom three layers were fixed at the optimized bulk lattice parameters to reduce the computational cost without influencing the accuracy of simulations. The convergence criteria for total energy and interatomic forces were set to 10<sup>-6</sup> eV per unit cell and 0.01eV/Å, respectively. All the calculations were performed with spin polarization as the antiferromagnetic ground state of Co<sub>3</sub>O<sub>4</sub>. The 3 × 4 × 1 Monkhorst–Pack grid was used to sample the Brillouin zone (convergence test for k-points data is shown in table 4.2), and the tetrahedron method with Blöchl corrections was employed for all calculations.

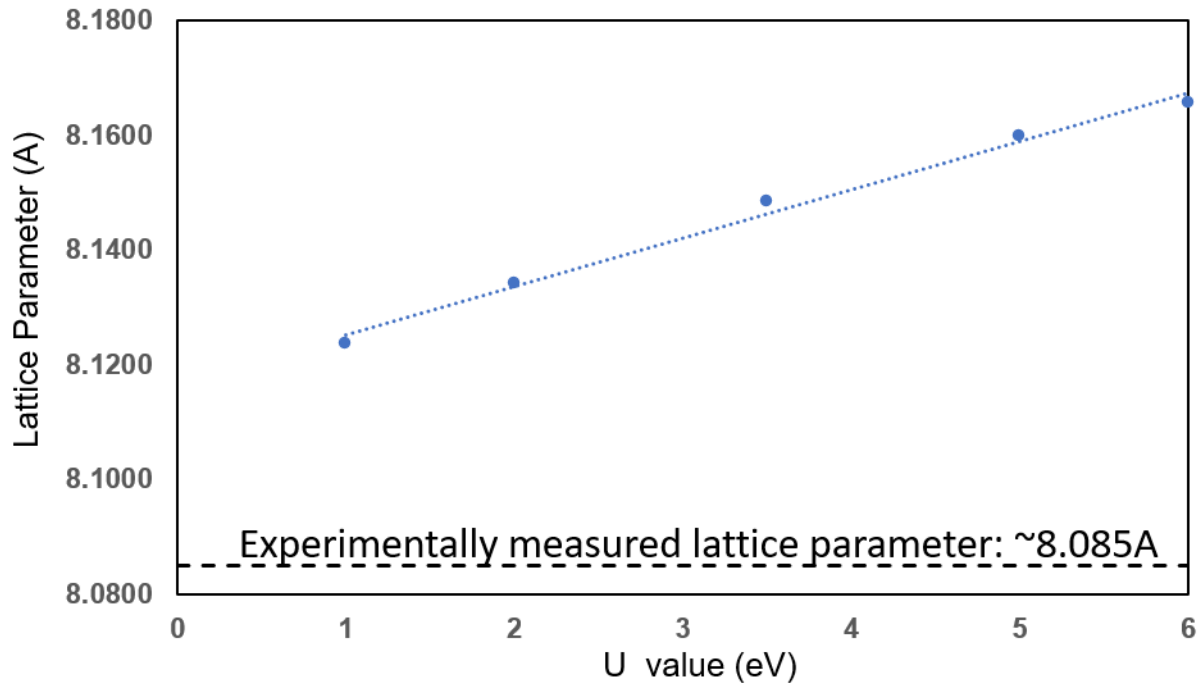


Figure 4.5. DFT+U optimized lattice parameter for  $\text{Co}_3\text{O}_4$  using different U values in comparison with experimentally measured lattice parameter

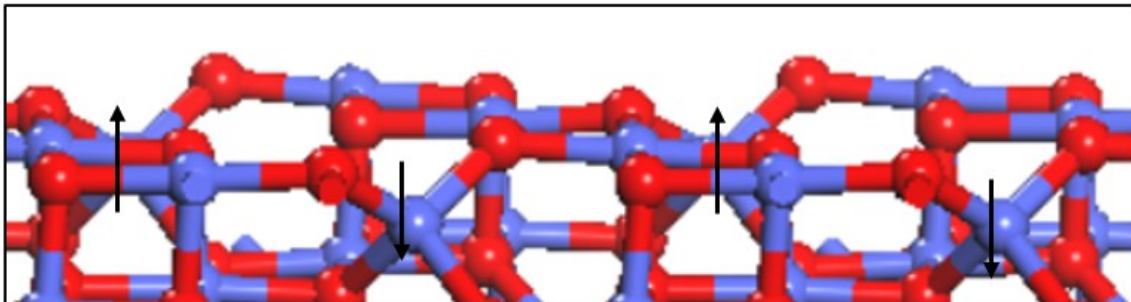


Figure 4.6. The most stable magnetic arrangement for  $\text{Co}_3\text{O}_4$  (100), showing magnetic spin ordering (where the alternating atoms of  $\text{Co}^{2+}$  in any particular layer have alternative magnetic spins, and  $\text{Co}^{3+}$  have 0 magnetic moment) The upward and downward arrows represent the positive and negative spin, respectively. Light blue and red balls represent cobalt (Co) and oxygen (O) atoms, respectively.

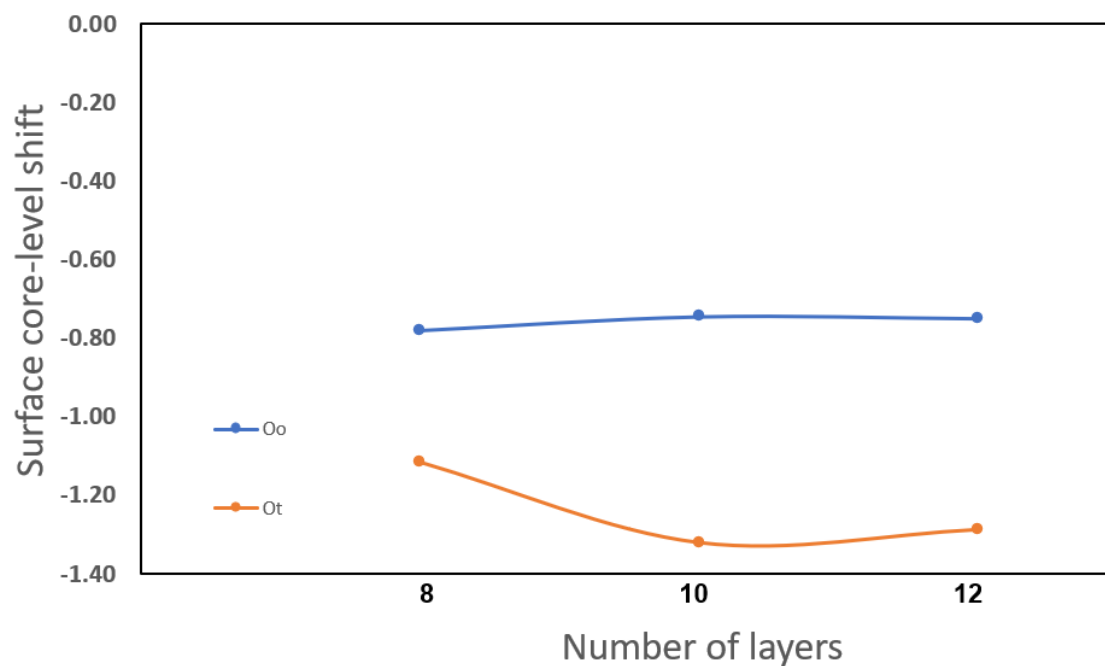


Figure 4.7. Convergence test showing the variation in calculated surface core level binding energy with the increasing slab thickness (number of layers) for surface oxygen on  $\text{Co}_3\text{O}_4$  (100) surface,  $\text{O}_o$  represents the octahedrally coordinated surface oxygen and  $\text{O}_t$  represents the tetrahedrally coordinated surface oxygen.

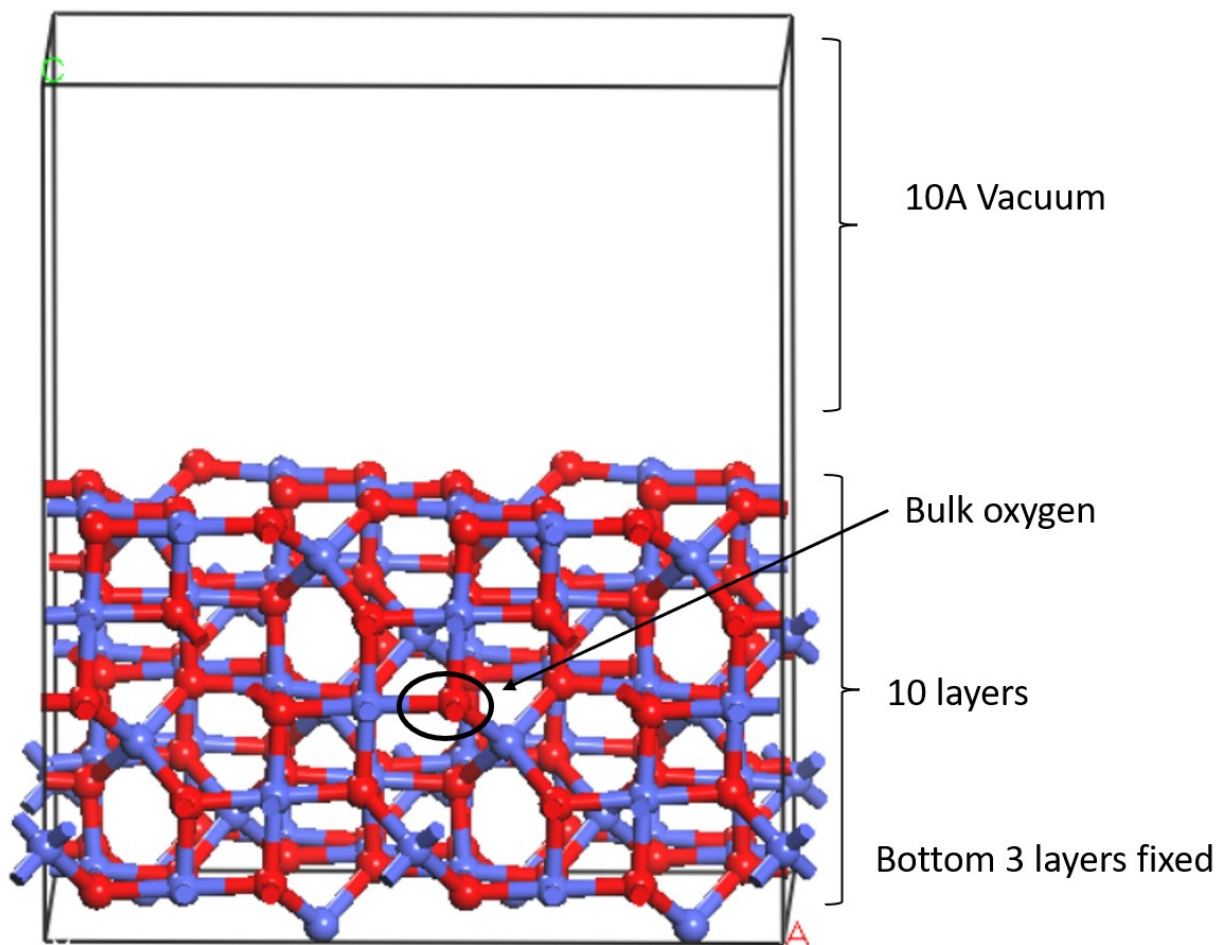


Figure 4.8. Representation of the system used to model  $\text{Co}_3\text{O}_4$  (100) surface, slab size, illustrating the number of layers and vacuum thickness. The oxygen atom in the central layers representing the bulk oxygen is highlighted. Light blue and red balls represent Cobalt (Co) and oxygen (O) atoms, respectively.

Table 4.2. The DFT calculated energy of the system of  $\text{Co}_3\text{O}_4$  with different k-point choices

KPOINT	Energy of the system (eV)
241	-413.163
441	-413.472
331	-413.242
<b>341</b>	<b>-413.470</b>

### 4.3 Screening of adsorbates on NiO (100) and Co<sub>3</sub>O<sub>4</sub> (100)

To screen the possible surface adsorbates, the most stable configuration for each adsorbate on TMO surfaces needs to be determined. The possible exposure of TMO samples to the atmosphere post-synthesis and during the surface characterization process would allow the molecules in the atmosphere (most likely oxygen and carbon dioxide) to adsorb on the surface. These molecules might further react with each other to form various surface species, such as carbonates and bicarbonates. Moreover, synthesized NiO materials might have intrinsic Ni Vacancy defects and intrinsic oxygen vacancy defects (especially under low oxygen concentrations); on the other hand, Co<sub>3</sub>O<sub>4</sub> is a reducible TMO with weak Co-O bond, which leads to the formation of reduced catalyst surface (stable O vacancies)<sup>127,128</sup>. Thus, the probable adsorbates and their adsorption configurations with clean or defective surfaces are considered and examined in this work. We checked the relative stability of each configuration for every surface adsorbate with possible vacancy sites. We chose the most stable configuration for core level binding energy calculations.

Figure 4.9 and 4.10 show the most stable DFT calculated configurations of clean surface, possible vacancy defects, and surface adsorbates on NiO (100) and Co<sub>3</sub>O<sub>4</sub> (100), respectively. The reason for choosing (100) facet for NiO is that it is the thermodynamically most stable facet, commonly reported in XRD results<sup>64</sup>. As for Co<sub>3</sub>O<sub>4</sub>, there are studies reporting that CO oxidation happens on (110)<sup>129</sup> and (111)<sup>130</sup> facets, yet more evidence shows that Co<sub>3</sub>O<sub>4</sub> (100) has better catalytic activity for oxygen evolution reaction, water dissociation, ammonia oxidation and nitrogen oxide reduction<sup>131-135</sup>. The termination of (100) facet was also tested in this study and B-termination (which contains octahedrally coordinated Co<sup>3+</sup> and O) was found to be the more stable termination, in agreement with the DFT results reported by Liu et al.<sup>131</sup> and Hashim et al.<sup>135</sup>.

According to Trinh et al.<sup>2</sup>, the DFT calculated core level binding energy changes for metal atoms across different U values are extremely small and not suitable for this approach. Hence, O1s core level binding energy for each individual oxygen atom in different surface species/configurations were calculated and presented in Table 4.3 and 4.4 for NiO(100) and Co<sub>3</sub>O<sub>4</sub> (100), respectively. The U values chosen in Table 4.3 and 4.4 are based on commonly established bulk property optimized U values and potential possible surface specific U values.

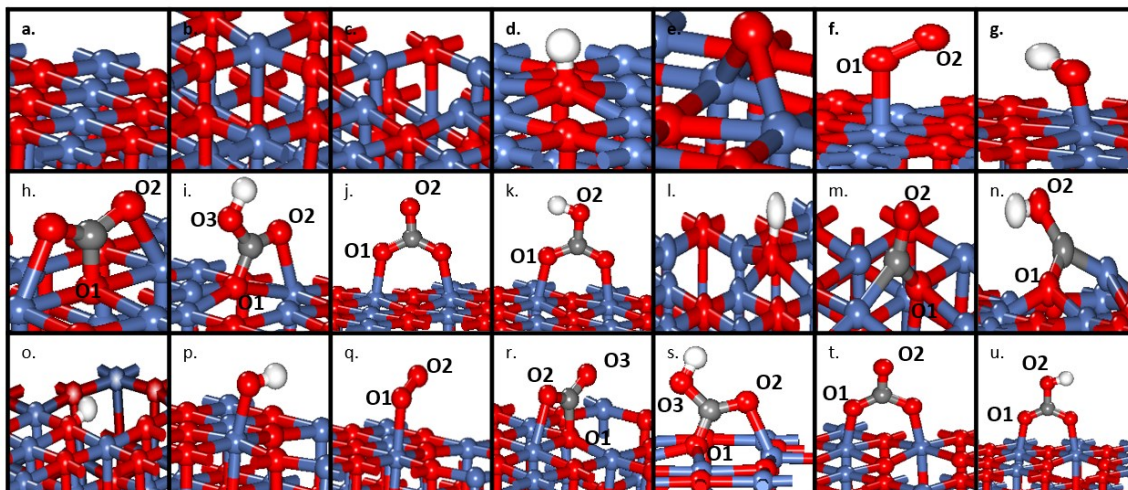


Figure 4.9. Structure of various surface adsorbates on NiO (100) surface evaluated to comparing with experimental XPS core level binding energy shifts. a.) clean surface, b.) Ni vacancy, c.) O vacancy, d.) adsorbed hydrogen, e.) adsorbed oxygen atom, f.) adsorbed oxygen molecule, g.) adsorbed hydroxyl group, h-k.) adsorbed carbonaceous species (adsCO<sub>2</sub>, adsHCO<sub>2</sub>, adsCO<sub>3</sub> and adsHCO<sub>3</sub>), l.) adsorbed hydrogen near O vacancy site, m-n.) adsorbed carbonaceous species near O vacancy site, o-q.) adsorbed hydrogen, adsorbed hydroxyl and adsorbed oxygen near Ni vacancy site, r-u.) adsorbed carbonaceous species near Ni Vacancy site. Dark blue, red, grey, and white balls represent nickel (Ni), oxygen (O), carbon (C) and hydrogen (H) atoms, respectively.

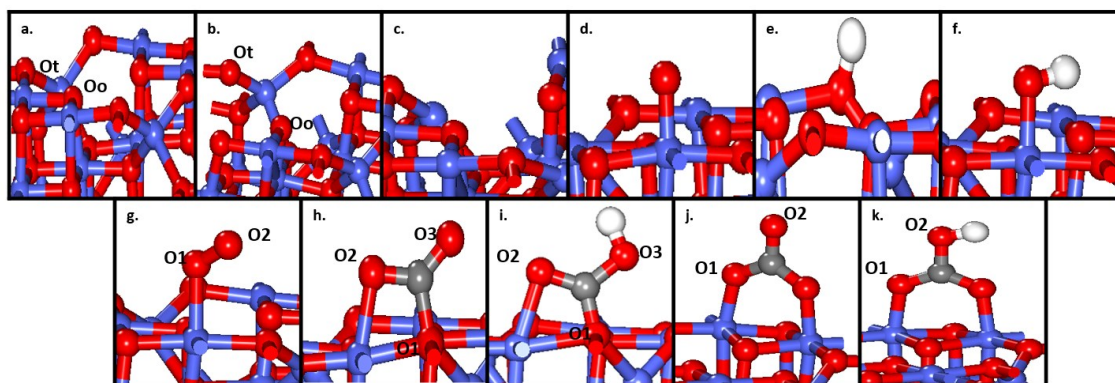


Figure 4.10 Structure of various surface adsorbates on Co<sub>3</sub>O<sub>4</sub> (100) surface evaluated to comparing with experimental XPS core level binding energy shifts. a.) clean surface, b.) Co vacancy, c.) O vacancy, d.) adsorbed oxygen atom, e.) adsorbed hydrogen, f.) adsorbed hydroxyl group, g.) adsorbed oxygen molecule, h-k.) adsorbed carbonaceous species (adsCO<sub>2</sub>, adsHCO<sub>2</sub>, adsCO<sub>3</sub> and adsHCO<sub>3</sub>). Light blue, red, grey, and white balls represent cobalt (Co), oxygen (O), carbon (C) and hydrogen (H) atoms, respective.

Table 4.3. O1s Core-level Binding Energy Shifts Relative to the O1s Core-level Binding Energy of Bulk Lattice Oxygen for Different Surface Adsorbates (corresponding to Fig. 4.9) on NiO (100) evaluated at U value of 5.3eV and 2eV. Values in bold are the shifts that can potentially match experimental data.

Adsorbate Corresponding to Figure 4.9	Structure	DFT-calculated O1s core-level binding energy shifts (eV) at different U values	
		U=5.3eV	U=2.0eV
a.	Clean surface	-2.53	-0.40
b.	Ni vac	-3.07	-1.16
c.	O <sub>vac</sub>	-0.26	-0.88
d.	<b>H<sub>ads</sub></b>	<b>0.73</b>	<b>2.36</b>
e.	O <sub>ads</sub>	-0.93	-2.61
f.	<b>O<sub>2 ads</sub> – O1</b>	<b>1.26</b>	<b>2.32</b>
	<b>O<sub>2 ads</sub> – O2</b>	<b>0.30</b>	<b>1.83</b>
g.	OH <sub>ads</sub>	-3.69	-1.55
h.	CO <sub>2 ads</sub> – O1	0.92	0.61
	CO <sub>2 ads</sub> – O2	0.43	0.82
	HCO <sub>2 ads</sub> – O1	-2.83	-1.40
i.	HCO <sub>2 ads</sub> – O2	-1.96	-1.30
	HCO <sub>2 ads</sub> – O3	3.14	2.81
	CO <sub>3 ads</sub> – O1	-1.80	-1.39
j.	CO <sub>3 ads</sub> – O2	-1.53	-1.03
	HCO <sub>3 ads</sub> – O1	-3.46	-0.95
k.	HCO <sub>3 ads</sub> – O2	-3.50	-0.81
	H <sub>ads</sub> @ O <sub>vac</sub>	-1.63	-1.91
m.	CO <sub>2 ads</sub> – O1 @ O <sub>vac</sub>	-1.27	0.68
	CO <sub>2 ads</sub> – O2 @ O <sub>vac</sub>	-1.77	0.45
n.	HCO <sub>2 ads</sub> – O1 @ O <sub>vac</sub>	1.70	-0.31
	HCO <sub>2 ads</sub> – O2 @ O <sub>vac</sub>	0.03	-0.60
o.	H <sub>ads</sub> @ Ni <sub>vac</sub>	-2.20	-0.60
p.	OH <sub>ads</sub> @ Ni <sub>vac</sub>	-3.01	0.01
q.	O <sub>2 ads</sub> – O1 @ Ni <sub>vac</sub>	1.01	0.07
	O <sub>2 ads</sub> – O2 @ Ni <sub>vac</sub>	0.51	-2.13
r.	CO <sub>2 ads</sub> – O1 @ Ni <sub>vac</sub>	-1.53	0.12
	CO <sub>2 ads</sub> – O2 @ Ni <sub>vac</sub>	-1.61	-1.18
	CO <sub>2 ads</sub> – O3 @ Ni <sub>vac</sub>	-2.83	-1.85
s.	HCO <sub>2 ads</sub> – O1 @ Ni <sub>vac</sub>	1.62	0.82
	HCO <sub>2 ads</sub> – O2 @ Ni <sub>vac</sub>	1.10	1.63
	<b>HCO<sub>2 ads</sub> – O3 @ Ni<sub>vac</sub></b>	<b>1.66</b>	<b>3.48</b>
t.	CO <sub>3 ads</sub> – O1 @ Ni <sub>vac</sub>	-1.29	0.35
	CO <sub>3 ads</sub> – O2 @ Ni <sub>vac</sub>	-2.86	-1.93
u.	HCO <sub>3 ads</sub> – O1 @ Ni <sub>vac</sub>	0.23	-0.91
	HCO <sub>3 ads</sub> – O2 @ Ni <sub>vac</sub>	0.80	-3.64

Table 4.4. O1s Core-level Binding Energy Shifts Relative to the O1s Core-level Binding Energy of Bulk Lattice Oxygen for Different Surface Adsorbates (corresponding to Fig. 4.10) on Co<sub>3</sub>O<sub>4</sub> (100) evaluated at U value of 6.0eV and 3.5eV. Values in bold are the shifts that can potentially match experimental data.

Corresponding in Figure 4.10.	Structure	DFT-calculated O1s core-level binding energy shifts (eV) at different U values	
		U=6.0eV	U=3.5eV
a.	clean surface - Ot	0.05	-1.32
	clean surface - Oo	-0.25	-0.74
b.	Co_vac - Ot	-0.44	-2.67
	Co_vac - Oo	-1.26	-2.39
c.	O_vac	-0.69	-0.28
d.	O <sub>ads</sub>	-0.51	-2.48
e.	<b>H<sub>ads</sub></b>	<b>3.76</b>	<b>2.02</b>
f.	OH <sub>ads</sub>	-0.13	-0.89
g.	O <sub>2 ads</sub> - O1	2.73	1.10
	O <sub>2 ads</sub> - O2	0.45	-0.10
h.	CO <sub>2 ads</sub> - O1	2.30	0.85
	CO <sub>2 ads</sub> - O2	1.31	0.31
	CO <sub>2 ads</sub> - O3	1.33	0.68
i.	<b>HCO<sub>2 ads</sub> - O1</b>	<b>4.74</b>	<b>2.74</b>
	<b>HCO<sub>2 ads</sub> - O2</b>	<b>3.98</b>	<b>2.49</b>
	HCO <sub>2 ads</sub> - O3	0.19	-1.10
j.	CO <sub>3 ads</sub> - O1	0.60	-0.05
	CO <sub>3 ads</sub> - O2	-0.47	-0.85
k.	<b>HCO<sub>3 ads</sub> - O1</b>	<b>2.26</b>	<b>1.61</b>
	HCO <sub>3 ads</sub> - O2	-1.15	-2.62

#### 4.4 The Rationale of Structure of Different Molecules Adsorbed on TMO surface

NiO has a typical rock-salt structure unit cell and NiO(100) terminal layer contains the equal number of nickel and oxygen atoms. All oxygen atoms on the clean surface layer are exactly the same therefore any surface oxygen could be chosen for O1s core level binding energy calculation, to compare with the lattice oxygen O1s core level binding energy. Co<sub>3</sub>O<sub>4</sub> has spinel structure, and the B-layer termination is more stable as discussed before, containing Co<sup>3+</sup> and O. The oxygen atoms in Co<sub>3</sub>O<sub>4</sub> are either connect to 2 Co<sup>3+</sup> and 1 Co<sup>2+</sup> or 3 Co<sup>3+</sup>. Therefore, the O1s core level binding energy of surface oxygen need to be calculated separately and compared to the bulk oxygen individually (all lattice oxygen atoms connect to 3 Co<sup>3+</sup> and 1 Co<sup>2+</sup>). The possible exposure of TMO samples to the atmosphere during the surface characterization process would allow the molecules in the atmosphere (most likely oxygen and carbon dioxide) to adsorb on the



surface. These molecules might further react with each other to form various surface species, such as carbonates and bicarbonates. Moreover, it is also possible that the synthesized TMO surfaces are not perfectly stoichiometric and may contain possible surface vacancies. Thus, the probable adsorbates and their adsorption configuration with clean or defect surfaces are considered and examined. When simulating various possible surface adsorbates on the TMO surface, we tested different configurations as many as possible and chose the most stable configuration for core level binding energy shift calculation.

**Oxygen Species on Oxygen Vacancy surface.** As discussed before, synthesized NiO materials might have intrinsic oxygen vacancy defects, especially under low oxygen concentrations, and  $\text{Co}_3\text{O}_4$  is a reducible TMO which leads to easily formation of oxygen vacancy defects on its surface. Thus, the probable adsorbates and their adsorption configuration with clean or defective surfaces are considered and examined at the same time. We checked the relative stability of each configuration for every surface adsorbate with possible vacancy site. We noticed that, for both TMO surfaces, when the oxygen species are interacting with the surface with oxygen defects site, one of the oxygen atoms in the specie would fill into the vacancy site to form the most stable adsorption configuration. For example, when  $\text{O}_2$  molecules is adsorbed on the surface with oxygen vacancy defects, the most stable configuration would be the same as atomic O adsorbed on the clean perfect surface. Similarly, a hydroxyl group adsorbed on oxygen defective surface would be like a hydrogen atom adsorbed on clean surface; adsorbed  $\text{CO}_3$  and  $\text{HCO}_3$  on oxygen defective surface would be the same as adsorbed  $\text{CO}_2$  and  $\text{HCO}_2$  on clean surface, respectively.

**The Choice of Oxygen for theoretical calculation.** Appendix A contains the detailed data and figures of configuration discussed in this section. After the most stable configuration is obtained, we chose the oxygens in the adsorbed species or the surface oxygen which is directly affected by surface adsorbates/vacancies to perform O1s core level binding energy calculations. The experimental XPS shifts could be referring to any possible oxygen on the sample surface. Hence, all potential oxygen candidates need to be tested. For  $\text{CO}_2$  adsorbed on NiO(100) surface (Figure A1a), using U values of 2eV and 5.3eV respectively, the calculated core level binding energy shifts difference between O2 and O2' are less than 0.05eV (Table A1). Due to the symmetric adsorption configuration, it is safe to assume that these two oxygen atoms have similar environment and only one of them need to be tested in the full range of DFT+U calculation.

Similar situations were found at  $\text{CO}_3$  and  $\text{HCO}_3$  adsorbed on NiO and  $\text{Co}_3\text{O}_4$  surface (Figure A1b-e, g, h), the calculated core level binding energy shifts for O1 and O1' in these cases are within the DFT accuracy (less than 0.1eV, as shown in Table A1 and A2), despite the choice of U value. The only exception is that  $\text{CO}_2$  on  $\text{Co}_3\text{O}_4(100)$  surface (Figure A1h), as we could notice in the adsorption configuration, that O2 and O3 are slightly different on the surface configuration. The calculated core level binding energy shifts using U value of 3.5eV is very similar ( $\sim 1.3\text{eV}$ ), yet when using U value of 6eV, the calculated shifts become 0.3eV and 0.7eV (as shown in Table A2). Thus, both oxygen atoms are reported, and this further confirms that the choice of U value is very important for surface sensitive phenomena.

#### 4.5 Comparison of experimental and computational core level binding energy shifts

After determining the configuration for each surface adsorbates on NiO (100), as shown in Figure 4.9, the O1s core level binding energy shifts with reference to bulk lattice oxygen were first calculated using the well-established U value of 5.3eV. As results are shown in Table 4.3, the widely used U value fails to predict any of the observed experimental O1s core-level shifts in any of the possible structures, similar to that observed by *Trinh et al.*<sup>2</sup> on CuO. Hence, different U values ranging from 1.0 to 6.0 eV are used to access its influence on the computed O 1s shifts. Moreover, we also notice that XPS shifts for some adsorbates cannot reproduce the experimentally observed values, irrespective of the choice of U value. For example, the adsorbed O atom's DFT computed shifts are negative at U values from 1.0-6.0eV. As mentioned before, the experimentally observed shifts are all positive values (+1.8, +2.2 and +3.6eV<sup>24-36</sup>). Therefore, it is unlikely that those adsorbates would correspond to the shifts observed experimentally. These results also assist in screening of the possible adsorbates on the catalytic surfaces, and these adsorbates can be ruled out while assigning adsorbates to the experimentally observed shifts.

Figure 4.11 shows the surface adsorbed  $\text{O}_2$ , surface adsorbed hydrogen and the surface adsorbed  $\text{HCO}_2$  structures. These structures are determined by comparing of experimental and theoretical core level binding energy shifts across the entire U value range from 1 to 6 eV and Figure 4.11 also shows the calculated shifts at different U values (blue dots) and experimental observed shifts in bold orange line. The computed core level binding energy shifts have a direct relationship with

the U values used, which is in agreement with what was observed on CuO surface as well. Due to NiO possessing a stronger metal-oxygen bond compared to CuO, it is predicted that a lower U value will be required (due to reduced electron delocalization). Additionally, because the surface atoms have a lower coordination number, the delocalization of electrons on the surface would be lower than in the bulk. Therefore, it is predicted that the surface U value would be smaller than the bulk property optimized U value to appropriately penalize the degree of electron delocalization on the TMO surface.

The surface adsorbed O<sub>2</sub>, surface adsorbed hydrogen and the surface adsorbed HCO<sub>2</sub> structures are the only structures that are able to reproduce the experimentally observed O1s core level binding energy shifts on NiO surface, at an appropriate U value. As shown in Figure 4.11a and b, one of the atoms of the adsorbed oxygen molecule which is not directly attached to the NiO surface could correctly predict the experimental core level binding energy shifts of +1.8eV when U value of 2eV is used, and the oxygen atom that directly attached to surface Ni of adsorbed oxygen molecule could predict the core level binding energy shift of +2.2eV using U values of 2-2.5eV. Similarly, Figure 4.11c also shows that the surface lattice oxygen attached to the adsorbed hydrogen could predict the core level binding energy of +2.2eV using U values of around 2eV. As for the shift of +3.6eV, it could be reproduced by the surface lattice oxygen which is attached to adsorbed HCO<sub>2</sub> closed to a Ni Vacancy site (Figure 4.11d), by using U values ranging around 1.5-2.0eV. Hence, a single U value of ~2eV gives the best overall prediction of experimental core level binding energy shifts (+1.8, +2.2 and +3.6eV). Concurrently, the corresponding adsorbed moieties are identified corresponding to the calculated shifts with surface specific U value. +1.8eV shift corresponds to the surface adsorbed oxygen molecules, +2.2eV shift corresponds to either the surface adsorbed oxygen molecule or the surface oxygen that is bonded to the adsorbed hydrogen atom, and +3.6eV shift corresponds to the adsorbed to HCO<sub>2</sub> near a Ni vacancy site on NiO surface.

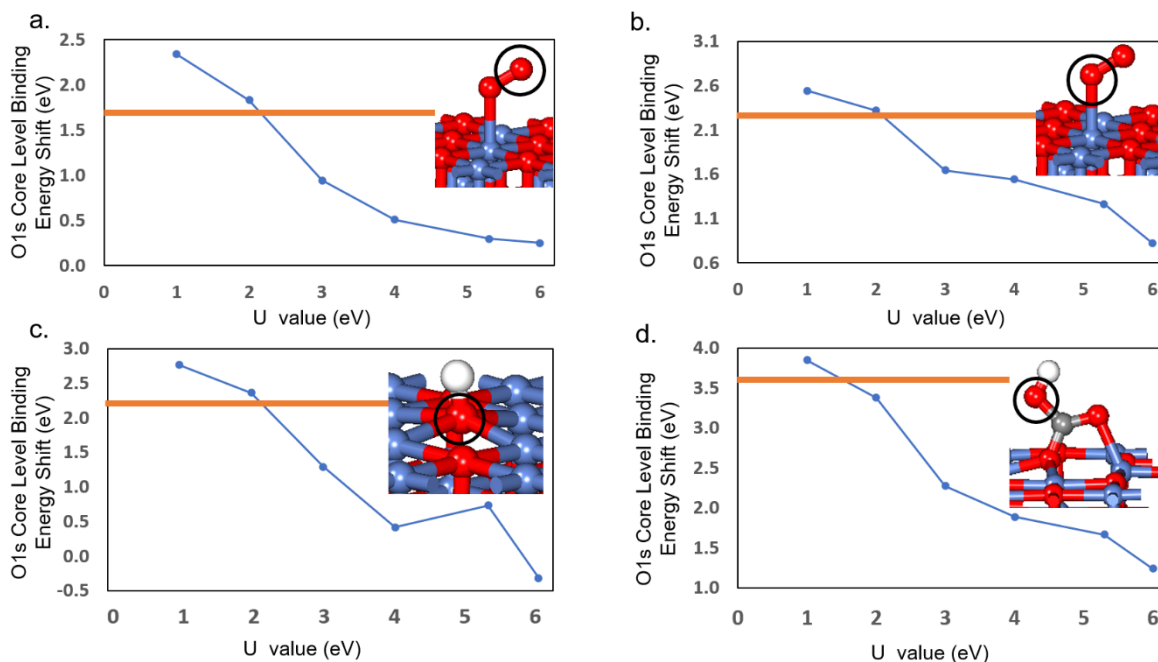


Figure 4.11. Variation of computed O1s core level binding energy shifts at different U values for a.)  $O_{2\text{ ads}} - O_2$ , b.)  $O_{2\text{ ads}} - O_1$ , c.) O attached with adsorbed H atom, d.)  $HCO_2\text{ ads} - O_3@Ni\_vac$  on NiO (100) surface. Experimental shifts are shown in bold orange line. Color code for atoms is the same as in Figure 4.9.

In the case of  $Co_3O_4$ , different U values are used to simulate bulk material properties. Hence, U values ranging from 1.0 to 6.0 eV were tested with the same approach. Table 4.4 summarizes the computational core level binding energy shifts for different adsorbates at U values of 6 eV and 3.5eV, as these values are used in previous studies<sup>54,83-88</sup>. Comparison of experimental and computational O1s core level binding energy shifts across the U value range from 1-6eV identifies surface adsorbed hydrogen atom, adsorbed  $HCO_3$  and  $HCO_2$  structures, as presented in Figure 4.12. Figure 4.12 also shows the calculated shifts at different U values in blue dots and experimental observed shifts in bold orange line. Similar to NiO, the computational shifts have a monotonic relationship with the U values used. These results also help screen the possible adsorbates, and most interestingly, we noticed that in surface Co vacancy or O vacancy case, the computed shifts are not able to reproduce the experimentally observed shifts at all, irrespective of the U value used. This indicates that despite the reduced  $Co_3O_4$  catalysts are often synthesized purposely<sup>127,128</sup>, experimentally observed positive XPS shifts on these catalysts do not correspond to the surface vacancy sites only. The surface species that can potentially correspond

to these shifts, as mentioned before, are surface adsorbed hydrogen atom, adsorbed  $\text{HCO}_3$  and  $\text{HCO}_2$ .

Figure 4.12 shows that surface adsorbed hydrogen atom, adsorbed  $\text{HCO}_3$  and  $\text{HCO}_2$  are potential structures that can be used to estimate the appropriate surface-specific  $U$  value that could accurately reproduce the experimental observed XPS O1s core level binding energy shifts on the  $\text{Co}_3\text{O}_4$  surface. As shown in Figure 4.12a and b, by using  $U$  values from 2.5-3eV, the surface oxygen that is attached to adsorbed hydrogen and the bottom oxygen connected to surface Co of adsorbed  $\text{HCO}_3$  on  $\text{Co}_3\text{O}_4$  surface could correctly reproduce the experimental core level binding energy of +1.5eV, respectively. Also, Figure 4.12c and d show that the oxygens connected with Co and C atom in surface adsorbed  $\text{HCO}_2$  are able to reproduce the experimental shift of +2.6eV. Using  $U$  value around 2.5-3eV, the surface lattice oxygen which is attached to adsorbed  $\text{HCO}_2$  could predict the experimental observed core level binding energy of 2.6eV; using  $U$  value around 3-3.5eV another oxygen that connected to surface cobalt and carbon atom in adsorbed  $\text{HCO}_2$  could reproduce 2.6eV experimental shifts. Hence, a single  $U$  value of  $\sim 3\text{eV}$  gives the best overall prediction of experimental core level binding energy shifts (+1.5 and +2.6eV). Interestingly, the surface specific  $U$  value determined here is in line with Selcuk and Selloni's work<sup>87</sup> as they conclude that  $U$  value of 3.0 eV provides a better description of surface reactivity based on calculated Bader's charge of surface Co atom, oxygen vacancy formation and water adsorption energy. Concurrently, the corresponding adsorbed moieties are identified. The +1.5eV shift corresponds to the surface oxygen that is attached to adsorbed hydrogen or the oxygen attached to surface Co in adsorbed  $\text{HCO}_3$  and +2.6eV shift corresponds to adsorbed  $\text{HCO}_2$ , either by surface oxygen connected to  $\text{HCO}_2$  or the oxygen that connected to carbon and surface Co atom on the  $\text{Co}_3\text{O}_4$  surface.

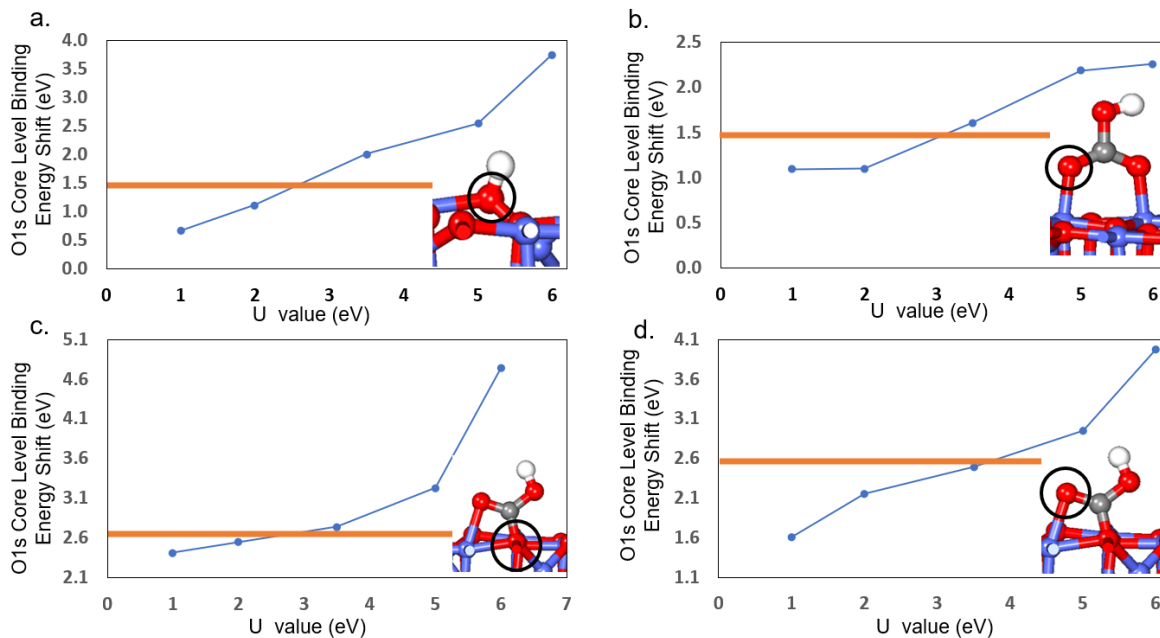


Figure 4.12. Variation of computed O1s core level binding energy shifts at different U values for a.) O attached with adsorbed H atom, b.) HCO<sub>3</sub> ads - O1, c.) HCO<sub>2</sub> ads - O1, d.) HCO<sub>2</sub> ads - O2 on Co<sub>3</sub>O<sub>4</sub> (100) surface. Experimental shifts are shown in bold orange line. Color code for atoms is the same as in Figure 4.10.

The surface U values purposed in this study, i.e., ~2.0eV for NiO and ~3.0eV for Co<sub>3</sub>O<sub>4</sub>, are benchmarked based on surface sensitive XPS data. Based on the previous studies regarding the U choice for CuO by Bhola et al.<sup>1</sup> and Trinh et al.<sup>2</sup>, it is suggested that these values will be able to accurately capture reaction and adsorption energies on NiO and Co<sub>3</sub>O<sub>4</sub> surfaces, respectively. This further reinforces that the bulk property optimized U values should not be used in the surface catalyzed reaction without further benchmarking. Additionally, we settled the debate regarding the choice of U value for Co<sub>3</sub>O<sub>4</sub>, regardless of multiple studies indicating that there is no “obvious best U value” to describe its properties<sup>54,87</sup>. The most suitable U value to describe its surface behavior is ~3eV, and this value could greatly help future investigations of surface catalyzed reactions, such as CO oxidation, oxygen evolution reaction, water dissociation, and nitrogen oxide reduction. Concurrently, we also settled the discrepancies about adsorbate surface species corresponding to the experimentally observed XPS core level binding energy shifts. It is important to point out that the previous assignments of these positive shifts on NiO and Co<sub>3</sub>O<sub>4</sub> surfaces to the surface vacancy sites are inaccurate. Based on DFT+U calculations, on NiO

surface, adsorbed oxygen molecules correspond to +1.8 or 2.2eV, the surface oxygen connected to adsorbed hydrogen correspond to +2.2eV and surface adsorbed HCO<sub>2</sub> near Ni deficiency site correspond to +3.6eV; on Co<sub>3</sub>O<sub>4</sub> surface, the surface oxygen connected to adsorbed hydrogen and surface adsorbed HCO<sub>3</sub> correspond to +1.5eV, and surface adsorbed HCO<sub>2</sub> correspond to +2.6eV. These assignments of experimental shifts to the surface adsorbates based on DFT+U calculation can provide guidelines for analyzing XPS shifts on NiO and Co<sub>3</sub>O<sub>4</sub> surfaces in the future. Moreover, the advanced experimental technique, in-situ XPS will be benefitted from this work as the shifts and corresponding adsorbates are assigned, to help identify the key surface adsorbates or intermediates during the reaction.

## 5. Low-temperature, water assisted tandem demethylenation of benzyl alcohol to phenol

The aromatic chemical industry has relied on petroleum as a primary chemical feedstock for more than half a century<sup>136,137</sup>. However, the recent goal towards the transition to a low-carbon society requires an alternate and sustainable carbon source<sup>138</sup>. In this context, emerging attention has been focused on the utilization of biomass<sup>139</sup>. The characteristic aromatic backbone of lignin in biomass makes it a potential feedstock for aromatic chemicals. The complex aromatic heterogeneity of lignin, however, makes it difficult to use as feedstock<sup>140-143</sup>. This also impacts the development of fundamentals and mechanistic understanding of lignin chemistry, which are crucial for its transformation to valuable aromatic moieties.<sup>144</sup> Lignin macromolecules contain methoxy and benzyl alcohol groups, among others, which have been reported to have major impact on lignin transformation<sup>145</sup>. Although a number of methods to activate benzyl alcohol groups in lignin are available, generally harsh reaction conditions such as strong acids or bases, alkali metals, or reducing or oxidizing reagents are employed and thus often results in undesired reaction by-products and complicated downstream processing<sup>146-149</sup>. Therefore, the development of new approaches for the activation of these functional groups is important, as these will play a crucial role in the implementation of lignocellulose as a renewable alternative to fossil carbon resources. Additionally, this will broaden the fundamental understanding of lignin transformation towards the lignin-first bio-refinery concepts.

In Section 5.1, all the experimental results are summarised. All computational investigations performed later are aimed to confirm the experimental observations and hypothesis. Appendix B contains supplementary figures and tables from the experimental result. From Section 5.2 to 5.6, the results of DFT+U investigations on sonochemical conversion of benzyl alcohol are discussed. Appendix C contains free energy profile figures for undesirable side reactions which are kinetically unfavourable according to computational results.

### 5.1 Summary of the experimental results of benzyl alcohol conversion on CuO

**CuO catalyst preparation and characterization.** A series of copper oxide catalysts were prepared with a leaf-like morphology at different ultrasound frequencies (578, 864 and 1140 kHz, wherein



referred to as CuO-578, CuO-864 and CuO-1140) following a sonochemical protocol developed in our group.<sup>90</sup> Detailed preparation protocol of the synthesized catalysts is described in the methods section. The fresh CuO-864 nanostructured catalyst was characterized by XRD, SEM, TEM, AFM and XPS techniques (Figure 5.1). XRD patterns (Figure 5.1a) with major peaks centered at  $2\theta = 35.5^\circ$  and  $38.8^\circ$  are indexed as CuO [-1 1 1] and CuO [1 1 1], respectively, which are characteristics of the pure monoclinic CuO crystallites phase. SEM analysis (Figure 5.1b) demonstrated the formation of a uniform leaf-shaped structure under ultrasound irradiation. TEM investigations (Figure 5.1c) revealed images that were consistent with the SEM observations and showed the leaf-like morphology of the as-synthesized CuO catalyst. This morphology was further confirmed by AFM investigations (Figure 5.1d), which also revealed a CuO nano-leaf structured samples surface roughness of  $0.85 \times 10^{-3} \pm 0.35 \mu\text{m}$ . The XPS analysis of the as-prepared CuO nanoleaves confirmed the formation of  $\text{Cu}^{2+}$  with binding energy centered at 933.6 eV, which is attributed to the core level of Cu 2p <sup>3/2</sup> (Figure 5.1e). Additional peaks occurring at 941 and 943 eV are due to the shakeup satellite peaks. Analysis of the Cu LMM spectra revealed a peak with kinetic energy centered at 918.2 eV (Figure 5.1f), characteristic of CuO nano-structured material, and significantly ruling out the possibility of the existence of a  $\text{Cu}_2\text{O}$  phase.<sup>103</sup>

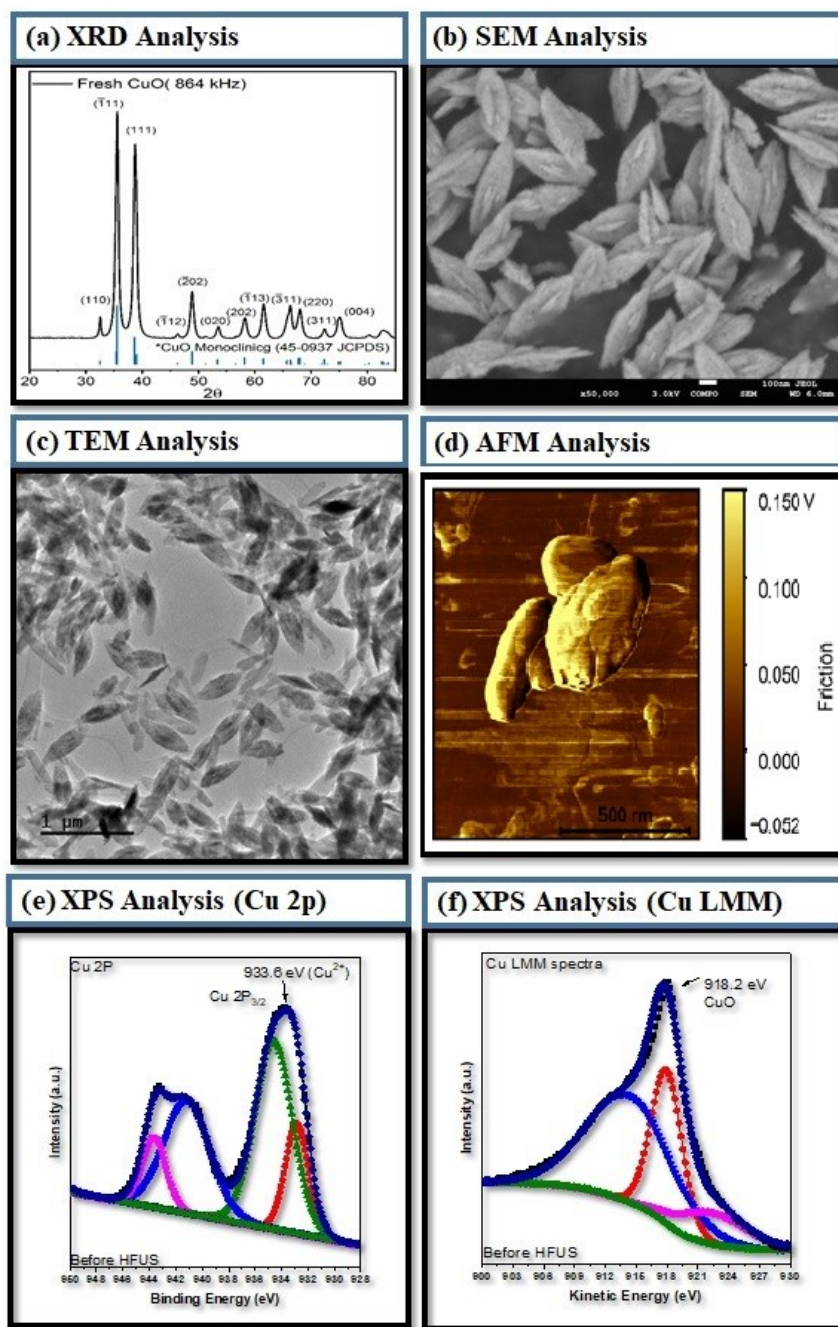


Figure 5.1 (a) XRD analysis (b) SEM analysis (c) TEM analysis (d) AFM analysis (e) XPS Cu<sub>2p</sub> analysis (f) XPS Cu LMM analysis, of as-prepared CuO catalyst.

**Sonocatalytic tandem demethylenation of phenol.** Prior to catalytic reactions, we investigated the *in-situ* production of hydrogen peroxide (H<sub>2</sub>O<sub>2</sub>) under an argon atmosphere during the irradiation of water by high-frequency ultrasound (578, 864 and 1140 kHz) as shown in Figure B1. During sonochemical irradiation of water under argon atmosphere, vapors of water trapped in the

cavitation bubbles can be pyrolyzed to yield  $\bullet\text{OH}$  and  $\bullet\text{H}$  radicals. These radical species can recombine to form  $\text{H}_2\text{O}_2$  and  $\text{H}_2$ , respectively.<sup>150</sup> Hence, pure water was sonicated at a controlled temperature of 25 °C, and the formation of  $\text{H}_2\text{O}_2$  was monitored using a standardized spectrophotometric method. After 90 min of irradiation,  $\sim 1.4 \text{ mmol.L}^{-1}$ ,  $\sim 1.1 \text{ mmol.L}^{-1}$  and  $1.0 \text{ mmol.L}^{-1}$  of  $\text{H}_2\text{O}_2$  concentrations were observed for 578, 864 and 1140 kHz ultrasonic frequencies, respectively, suggesting the successful *in-situ* formation of  $\text{H}_2\text{O}_2$  in neat water (Figure B2). Based on the concentrations of  $\text{H}_2\text{O}_2$  obtained, the ultrasound frequency of 578 kHz was selected for all other sono (catalytic) reactions, unless otherwise stated. To explore the possibility of (1) CuO catalyst acting as a nucleating agent in line with the principle of heterogeneous cavitation, i.e., the particles of CuO serve as nuclei for the formation and growth of cavitation bubbles, a great means to enhance the formation of inertial cavitation, and (2) the transfer of radicals produced inside the cavitation bubble onto a solid catalyst surface during cavitation bubbles implosion, we investigated (i) the acoustic response during irradiation of neat water both in the presence and absence of CuO-578 catalyst, and (ii) *in-situ* formation of  $\text{H}_2\text{O}_2$  in the presence of CuO-578 solid catalyst (Figure 5.2a and 5.2b), respectively. Catalysts prepared at different ultrasound frequencies were also investigated (Table B1). The acoustic response results demonstrated that CuO catalysts were acoustically responsive and capable of reducing the pressure requirement for inertial cavitation to occur (Figure 5.2a). From this result, the cavitation threshold (where the broadband cavitation probability was at least 50 %) was calculated as  $7.59 \pm 0.57 \text{ MPa}$ . Comparably, neat water did not cavitate through this pressure regime, indicating that CuO nanoleaves enabled gas nucleation on the particle surface for an enhanced cavitation response at reduced pressures. The frequency characteristics of the acoustic response were also quantified below and above the threshold of the nanoleaves (Figure 5.2b). From this, we observed an increasingly broadband noise composition as the peak negative pressure increased. This broadband noise is indicative of inertial cavitation, thus, it can be reasoned that the nanoleaves are capable of nucleating gas bubbles and promoting inertial cavitation events. Next, the formation rate of  $\text{H}_2\text{O}_2$  was investigated. After 90 min of irradiation in the presence of CuO solid catalysts, the concentrations of  $\text{H}_2\text{O}_2$  were observed to be  $\sim 0.3$  and  $0.25 \text{ mmol.L}^{-1}$  over CuO-578 and CuO-1140 catalysts, respectively. Whereas  $\text{H}_2\text{O}_2$  concentration observed over CuO-864 catalyst was only  $\sim 0.1 \text{ mmol.L}^{-1}$ , which is 93 % lower than that observed ( $1.4 \text{ mmol.L}^{-1}$ ) in pure water, in the absence of CuO. This suggests that radicals formed during the ultrasonic

irradiation of water interact with the surface of the CuO solid catalyst. The interaction with the catalyst significantly limits the diffusion of OH radicals into the bulk phase and their subsequent recombination to form H<sub>2</sub>O<sub>2</sub>. The recovered CuO-864 catalyst after ultrasound irradiation was dried overnight in an oven at 60 °C without any further post-treatment and again introduced into the ultrasound reactor to re-evaluate its impact on the production of H<sub>2</sub>O<sub>2</sub>. The observed rate of H<sub>2</sub>O<sub>2</sub> formation (Figure 5.2c) was strikingly similar to the fresh CuO-864 catalyst, suggesting that high-frequency ultrasound irradiation did not impact the structural integrity of the CuO catalyst. To further confirm this, x-ray diffraction (XRD), X-ray photoelectron spectroscopy (XPS) and scanning electron microscopic (SEM) analyses of the fresh and recycled CuO (after ultrasonic irradiation) were also performed (Figure B3).

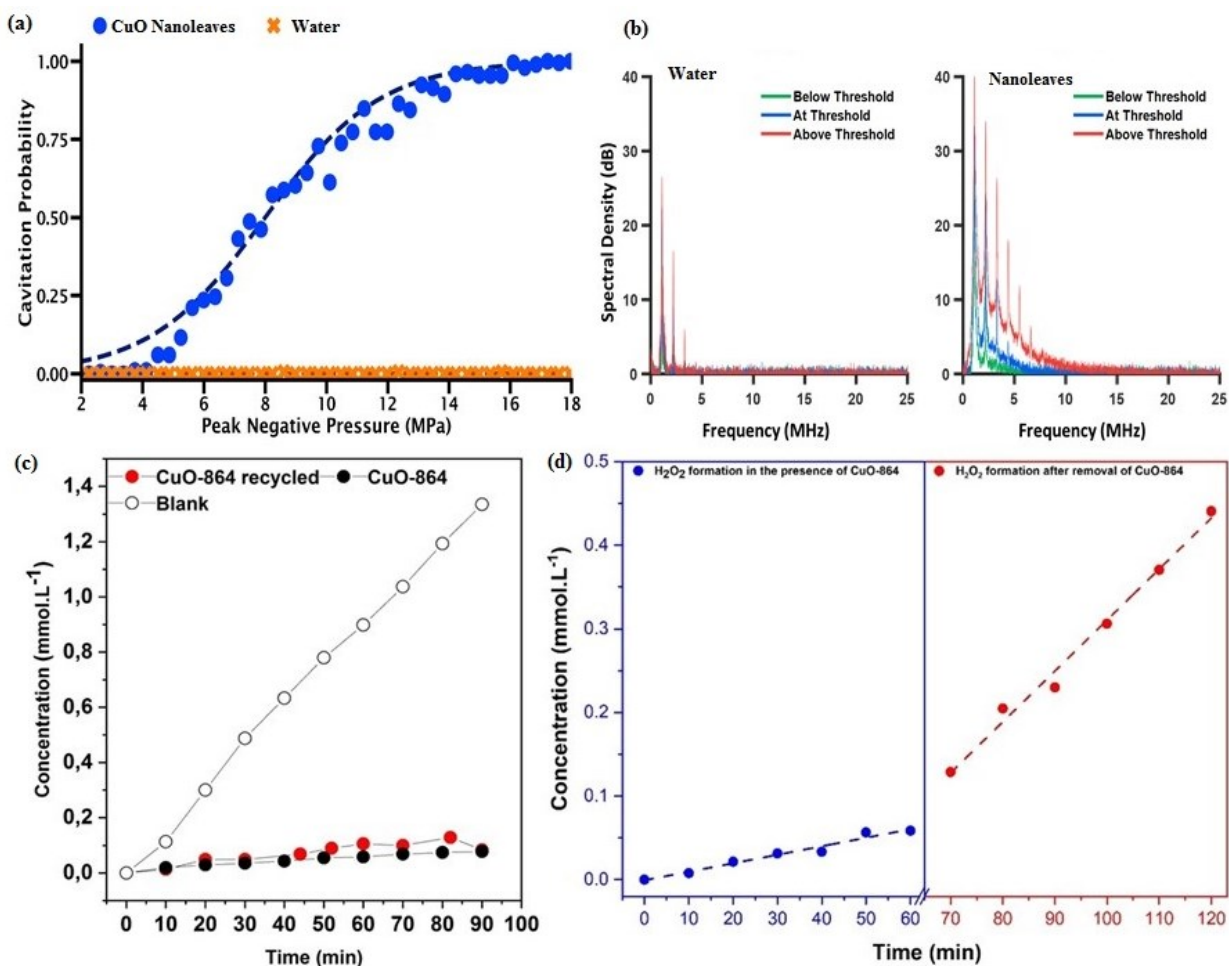


Figure 5.2 In-situ formation of H<sub>2</sub>O<sub>2</sub> in the presence and absence of CuO catalyst and In-situ formation of H<sub>2</sub>O<sub>2</sub> in the presence of CuO-864 catalyst (blue code), in-situ formation of H<sub>2</sub>O<sub>2</sub> during hot filtration test (red code). 578 kHz, 0.11 W.mL<sup>-1</sup>, 25 °C

After 60 min of irradiation in the presence of CuO catalyst, a hot filtration test was performed, where the CuO catalyst was filtered out of the solution and irradiation was initiated again on the blank water (Figure 5.2d). An increase in the rate of H<sub>2</sub>O<sub>2</sub> formation was observed, reaching 0.45 mmol.L<sup>-1</sup>, further confirming that the CuO solid catalyst indeed interacts with OH radicals generated during the irradiation, and suppresses their recombination to H<sub>2</sub>O<sub>2</sub> in the bulk solution.

Catalytic performance tests, with benzyl alcohol as the reactant were conducted in the high frequency (578 kHz) ultrasound reactor in the presence of argon bubbling (20 mL.min<sup>-1</sup>) at a controlled reaction temperature of 25 °C. Without adding a catalyst only < 15 % yield (maximum) of phenol was observed at a benzyl alcohol conversion of 33 %, within 1.5 h of reaction time. Extending irradiation time did not lead to any improved phenol formation (Figure B4). However, in the presence of CuO-864 nanoleaf catalyst, a steady increase in the yield of phenol with time was observed (Figure 5.3). Phenol yields were determined at a reaction irradiation time span of 0.5-4 h (Reaction conditions: 5 mmol.L<sup>-1</sup> of benzyl alcohol, 100 mL H<sub>2</sub>O, 578 kHz, Ar flow (20 mL/min), 25 °C, P<sub>acous.vol</sub> = 0.11 W·mL<sup>-1</sup>). A rapid increase in the conversion of benzyl alcohol was observed from 16 % to 80 %, after 0.5 h to 4 h of reaction time. However, the yield of phenol increased gradually from 13 % to 30 %, from 0.5 h to 2.5 h of irradiation time, then decreased steadily from 30 % to 14 %, from 2.5 h to 4 h. The initial increase in the yield of phenol demonstrates the synergy between the CuO catalyst and the ultrasound irradiation in driving the tandem demethylenation of benzyl alcohol and steering it away from an uncontrolled oxidation reaction. Detailed analysis of the reaction products revealed the formation of benzaldehyde, hydroxy-benzyl alcohol (*ortho*-hydroxy-benzyl alcohol, *meta*-hydroxy-benzyl alcohol and *para*-hydroxy-benzyl alcohol), hydroxy-benzaldehyde (*meta*-hydroxy-benzaldehyde and *para*-hydroxy-benzaldehyde), hydroquinone, catechol and benzoquinone (with a total yield of 3 % to 14 %, after 0.5 h to 4 h of reaction irradiation time). The identification and quantification of these products provided clues to the reaction mechanism for the formation of phenol and its subsequent reactions (after reaching a maximum at 2.5 h) with the increase in irradiation time.

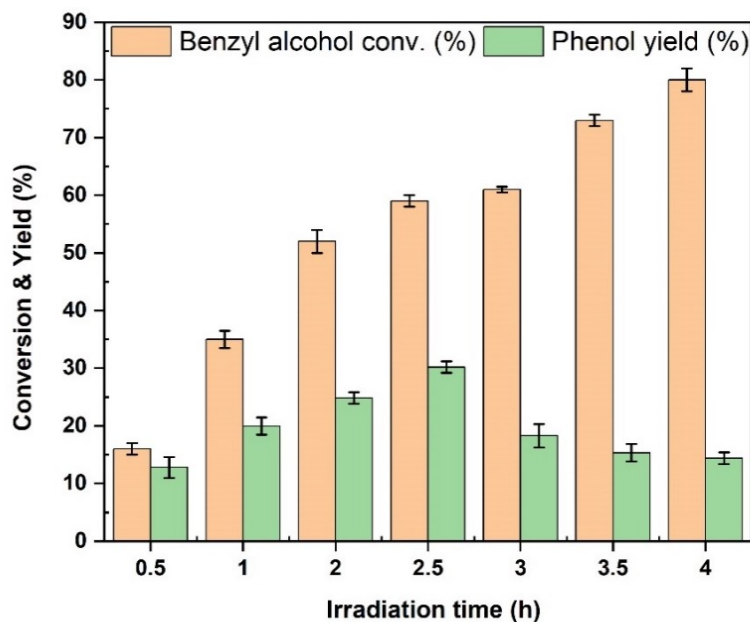


Figure 5.3 Conversion of benzyl alcohol and phenol yields in the ultrasound reactor, as a function of time. Reaction conditions: 5 mmol.L<sup>-1</sup> Benzyl alcohol, 5.4 mg CuO, 578 kHz, 0.11 W/mL, 25 °C

To identify the role of the radicals generated during irradiation in the overall reaction, we further conducted a series of inhibition and isotope-labelling experiments. First, *tert*-Butanol (TBA) and carbon tetrachloride (CCl<sub>4</sub>) were chosen as radical scavengers owing to their ability to effectively scavenge •OH and •H radicals, respectively.<sup>151</sup> Next, deuterated water (D<sub>2</sub>O) was chosen as the solvent to investigate the source of OH in the product phenol. The addition of TBA during the reaction caused a drastic decrease in the conversion of benzyl alcohol, i.e., 3 % to 39 % after 0.5 h and 4 h of reaction time, respectively. The formation of phenol in the initial stage of the reaction, and the rate of alcohol conversion are significantly impacted by the presence of TBA scavenger (Figure B5). At 0.5 h, 3 % of phenol was observed, reaching only 10 % after 2 h. Interestingly, phenol yield increased from 10 % to 22 %, after 2 h to 4 h of reaction irradiation. Presumably, TBA effectively (5 mmol.L<sup>-1</sup>) scavenged •OH radicals responsible for the formation of phenol at the initial stage of the reaction irradiation time. As the reaction progressed, TBA was consumed (confirmed by HPLC quantification), subsequently leading to the increase in phenol formation. An increase in the concentration of TBA (from 5 to 10 mmol.L<sup>-1</sup>) led to a total inhibition of phenol formation even after 4 h of reaction irradiation time, indicating the efficient

scavenging of •OH radicals responsible for the inhibition of the formation of phenol. Conversely, when CCl<sub>4</sub> was introduced into the ultrasound reactor (Figure B6), the conversion of benzyl alcohol increased steadily from 22 % at 0.5 h irradiation time to 74 % at 4 h irradiation time. The yields of phenol also saw a similar enhancement from 11 % at 0.5 h to 25 % at 4 h of reaction irradiation time, values significantly higher than those observed in the presence of TBA. These results indicate that •H radicals played no role in phenol formation. The quenching results reveal that •OH radicals significantly contribute to the selective demethylenation of benzyl alcohol to phenol, whereas •H radicals were merely spectators in formation of phenol. To further confirm the role of •OH radicals originating from the sonochemical dissociation of H<sub>2</sub>O in the reaction, deuterated water (D<sub>2</sub>O) was used as the solvent. A high resolution mass spectrometric (HR-MS) analysis of the crude reaction product revealed the appearance of a peak at  $m/z = 94.0412$  g/mol, confirming the incorporation of •OD in phenol (Figure B7).

The temperature of the ultrasound reactor was increased from 25 °C to 60 °C to investigate the impact of bulk liquid temperature on the sonocatalytic reaction. At 60 °C, phenol selectivity was not significantly impacted, however, the rate of benzyl alcohol conversion was slower (Figure B8) compared to the reactions at 25 °C (Figure 5.3). The increase in the bulk temperature of the solution lowers the threshold of cavitation bubble production, increases vapor pressure, and decreases surface tension, which can concomitantly weaken bubble collapse intensity. These results are in agreement with the sonoluminescence study reported by Didenko et al. and Pickworth et al.,<sup>152,153</sup> where sonoluminescence intensities (physical indication of hot-spot temperature created during cavity implosion) were found to decrease with the increase in temperature.

**Experimental insights into reaction mechanism.** To get insights into the reaction mechanism, first, benzaldehyde was tested as a reactant (Table 5.1, entry 1-4). In this case too, phenol was observed as the major product (~ 11.2 %) after 30 min, at a conversion of 23.2 %. The yield increased steadily to 23.1 % after 2.5 h, at a conversion of 66 %, along with trace amounts of *para*-hydroxy-benzaldehyde (< 1%). These results suggest that benzaldehyde is an intermediate species for the formation of phenol from benzyl alcohol. No benzoic acid was detected in reaction products. To assess the possibility of phenol formation *via para*-hydroxyl benzyl alcohol as an intermediate, *para*-hydroxyl benzyl alcohol was used as a reactant in the

sonocatalytic reaction (Table 5.1, entry 5-8). Hydroquinone was observed as the major product with yield of ~ 8 % at a conversion of ~ 26 % within 1 h of reaction irradiation (Table 5.11, entry 5), which further increased to 15 % yield at a conversion of 72 %, after 3 h reaction irradiation. Noteworthy, benzoquinone and *para*-hydroxyl benzaldehyde were formed alongside hydroquinone with yields of ~ 4 % and ~ 2 %, respectively. It is also interesting to state that, no phenol was formed when hydroxyl benzyl alcohol was used as substrate. This confirms that, (i) benzaldehyde is an intermediate species in the formation of phenol and (ii) the presence of an additional hydroxyl group in benzyl alcohol (*para*-hydroxyl benzyl alcohol) does not alter the reaction pathway and the activation of alcohol group.

To evaluate the role of high-frequency ultrasound irradiation, the reaction of benzyl alcohol catalyzed by CuO was performed under silent conditions (that is, in the absence of ultrasound) and also under low-frequency ultrasound (20 kHz) irradiation at a controlled temperature of 25 °C. Under silent conditions at 25 °C and 100 °C in argon flow, no product formation was observed (Table B2 entry 1 and 2). However, reactions performed in the presence of H<sub>2</sub>O<sub>2(aq)</sub> under silent conditions at 62 °C resulted in the formation of phenol (9 % yield) at a benzyl alcohol conversion of 9 % within 1 h of reaction time (Table B2, entry 3). Upon increasing the reaction time from 2h to 6h, the conversion of benzyl alcohol increased to ~ 35 % at 2 h and remained constant even up to 6 h reaction time. The yield towards phenol behaved similarly, with a phenol yield of ~ 13 % at 2h, which then plateaued from 3 h to 6 h. The depletion of H<sub>2</sub>O<sub>2</sub> under silent conditions during the course of the reaction explains the plateau in conversion and yield after 2h reaction time. These results further reinforce the importance of high-frequency ultrasound in the generation of *in-situ* OH radicals from water, crucial for the tandem demethylenation catalytic reaction.



Table 5.1 Product yields for the CuO catalyzed sonochemical oxidation of model substrate

Substrate	Gas atmosphere	Reaction time (h)	Conversion (%)	Benzaldehyde	Phenol	Hydroxybenzylalcohol	Benzoquinon	Hydroxybenzaldehyde	Hydroquinone
Benzaldehyde	Argon	0.5	23.2	-	11.2	0	0	0.5	0
		1	39.8	-	18.2	0	0	0.4	0
		2	54	-	19.3	0	0	0	0
		2.5	66.2	-	23.1	0	0	0	0
Hydroxybenzyl alcohol	Argon	1	25.7	0	0	-	1.6	2.1	8.2
		2	56.2	0	0	-	3.6	2.6	14.4
		3	72.4	0	0	-	3.7	2.2	15.4
		4	85.6	0	0	-	4.3	1.8.2	14.4
Reactions condition: 5 mmol.L <sup>-1</sup> of the substrate, 100 mL of H <sub>2</sub> O, 10 wt.% of CuO-864 catalyst, 578 kHz, Ar bubbling (20 mL.min <sup>-1</sup> ), 25 °C, $P_{\text{acous.vol}} = 0.11 \text{ W}\cdot\text{mL}^{-1}$									

## 5.2 DFT+U investigations into benzyl alcohol conversion to phenol on CuO (111)

As discussed before, the appropriate surface-specific U value is important for DFT+U calculations to accurately predict the surface reactions, pathways, and energetics, instead of U value optimized for bulk properties. According to *Bhola et al.*<sup>1</sup> and *Trinh et al.*<sup>2</sup>, the Hubbard U correction of 4.0 eV should be used as it could successfully capture the surface O1s core level binding energy and experimental surface adsorption enthalpy on CuO (111) surface. The investigation done in the following sections is an example of how such surface property optimized U value could be used in the TMO surface catalyzed reaction, to elucidate the experimental observations with theoretical evidence.

Density functional theory (DFT) calculations were performed to (i) elucidate the detailed reaction mechanism and compute activation free energy barriers and reaction free energies of the catalytic conversion of benzyl alcohol to phenol; ii) investigate the dissociation of water on the catalyst surface and the role of water and H<sub>2</sub>O<sub>2</sub> in the reaction; iii) confirm the postulated reaction mechanism of the catalytic conversion of benzaldehyde and *para*-hydroxy-benzyl alcohol, in line with the experiments performed in the presence of H<sub>2</sub>O<sub>2</sub> under silent conditions; and iv) elucidate the formation mechanism of the side product, ethylene glycol. CuO (111) was chosen for the computational investigation as it is the thermodynamically most stable facet of the pure monoclinic CuO and agrees with the experimental XRD data shown in Figure 5.1a. Figure 5.4 shows the pathways for the conversion of benzyl alcohol to phenol (catalyzed by lattice oxygen and by OH generated due to ultrasound induced water dissociation), including the O-H, C-H, and C-C activation and the corresponding free energy activation barriers for each elementary reaction step. The most favourable pathway is highlighted and its free energy profile with the transition state for each elementary reaction step is shown in Figure 5.5. All reported free energy barriers and reaction free energies are computed at 25 °C (the entropy, zero-point energy and enthalpy correction were all considered).

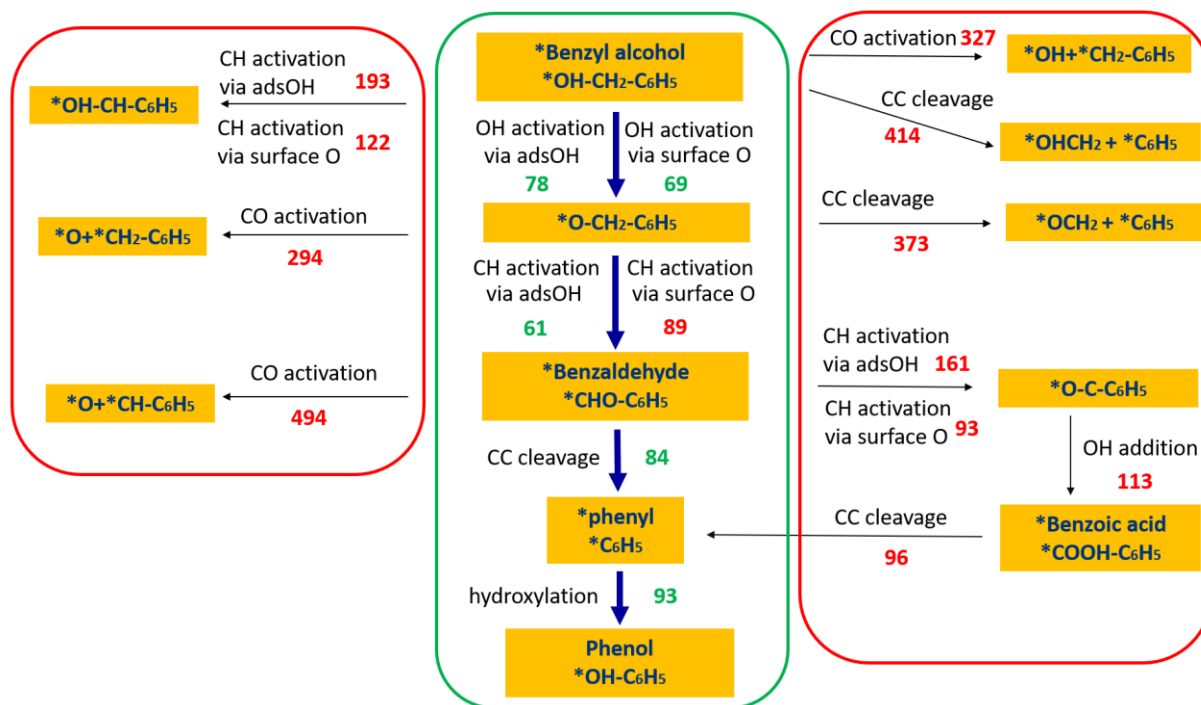


Figure 5.4 Mechanisms and energy profiles of the conversion of benzyl alcohol to phenol on CuO (111). Activation free energy barriers ( $E_a$ ) in kJ/mol are shown. Green values are activation barriers for the kinetically favourable reaction steps and red values indicate the activation barriers of reaction steps which are less favourable. Bold blue arrows indicate the preferred reaction pathway

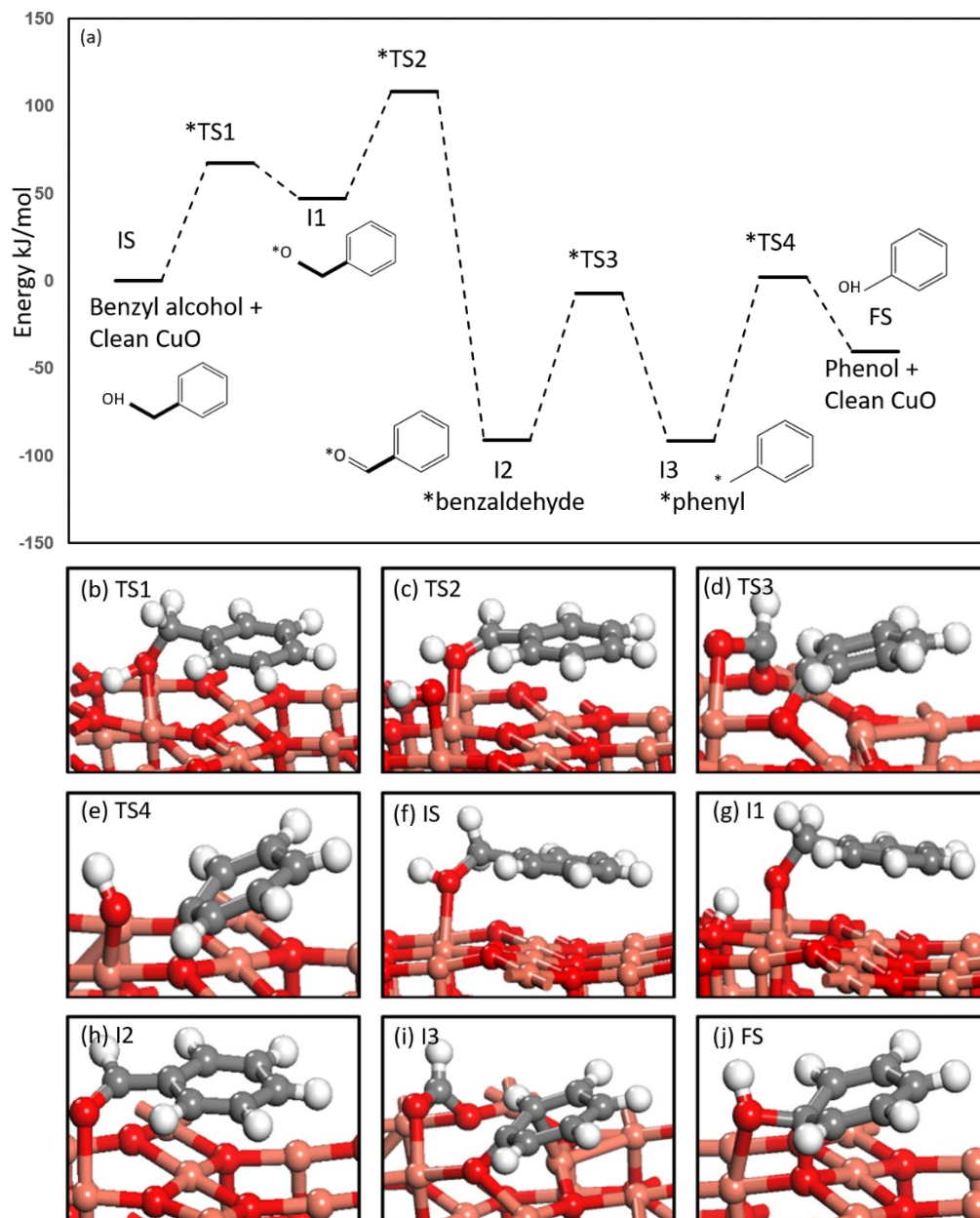


Figure 5.5 (a) Free Energy profile for the catalytic conversion of benzyl alcohol to phenol on CuO (111) surface; (b) transition state for initial O-H activation (\*TS1); (c) transition state for subsequent C-H activation to form benzaldehyde (\*TS2); (d) transition state for C-C cleavage from benzaldehyde (\*TS3); (e) transition state for hydroxylation to phenyl ring(\*TS4); (f) adsorbed benzyl alcohol (IS), (g) intermediate after initial O-H activation (IS), (h) key intermediate of benzaldehyde (I2), (i) intermediate after C-C cleavage from benzaldehyde (I3) and (j) adsorbed phenol (FS) on CuO (111) surface. Activation free energy barriers and reaction free energies are in kJ/mol. Salmon, red, grey, and white balls represent copper (Cu), oxygen (O), carbon (C) and hydrogen (H) atoms, respectively.

### 5.3 Benzyl alcohol to phenol reaction mechanism

As experimental results suggest, the OH group from water or H<sub>2</sub>O<sub>2</sub> plays a role in the conversion of benzyl alcohol to phenol. *Amaniampong et al.*<sup>125</sup> also suggested that OH groups on CuO (111) surface could lower the barrier for C-H activation in glycerol significantly. Thus, surface adsorbed hydroxyl groups assisted pathways are computed, as shown in Figure 5.4. On a clean CuO (111) surface, benzyl alcohol is activated via its alcohol group, and the activation free energy barriers for O-H cleavage are 78 and 69 kJ/mol via the surface adsorbed OH group and surface lattice oxygen, respectively. Alternate first activation pathways such as direct C-C cleavage, C-H activation (via surface oxygen and surface adsorbed hydroxyl group) or C-O activation have significantly higher activation barriers of 414, 122, 193 and 327 kJ/mol, respectively, as can be seen in Figure 5.4. O-H activation is slightly preferred via the surface lattice oxygen, both kinetically and thermodynamically, as shown in the transition state in Figure 5.5. As the OH of the benzyl alcohol group is activated, a bridge configuration is formed through the two surface copper atoms and oxygen in the intermediate structure II (Figure 5.5g). The most preferred reaction pathway after that is the activation of the C-H bond by surface adsorbed OH group to form adsorbed benzaldehyde (Figure 5.5h), with the activation barrier of 61 kJ/mol, as the transition state is shown in Figure 5.5c. In this reaction step, surface adsorbed hydroxyl group assisted C-H activation is preferred over the C-H activation via surface lattice oxygen. This suggests that the surface adsorbed hydroxyl group could alter reaction kinetics, confirming the experimental hypothesis. It is also important to mention that the reaction free energy of this step is -138kJ/mol (compared to -71kJ/mol for the C-H activation via surface oxygen), thus revealing that benzaldehyde is strongly adsorbed on the catalyst surface. The DFT calculated free energy barrier for benzaldehyde desorption is over 200 kJ/mol, which further explains why benzaldehyde is not observed as a product in the experiments though it is an intermediate in the reaction. Further, C-C cleavage between the aldehyde group and phenyl ring (the transition state is shown in Figure 5.5d) was favoured kinetically over C-O and C-H activation (activation barriers are shown in Figure 5.4). The dissociated aldehyde group on the catalytic surface can undergo C-C coupling to form ethylene glycol as a by-product. The reaction mechanism for ethylene glycol is presented and discussed later. The adsorbed phenyl group (\*C<sub>6</sub>H<sub>5</sub>) on the catalyst surface would undergo hydroxylation to form phenol, a major product observed in the

experiment (the transition state is shown in Figure 5.5e). The free energy barrier and reaction free energy of phenol formation are 93 and 51 kJ/mol, respectively. The free energy for phenol desorption from the catalyst surface was calculated to be only 21 kJ/mol. The DFT computed reaction pathway from benzyl alcohol to phenol is in agreement with the experimental results, as benzaldehyde is observed as an intermediate and OH group from water plays a role in facilitating the formation of phenol. The source of the surface OH group and the importance of benzaldehyde as an intermediate in the reaction pathway would be discussed further in the following sections.

#### **5.4 The role of water/hydrogen peroxide in the formation of phenol**

Water is suggested to be the source of the surface OH group, via high-frequency ultrasound induced dissociation. The activation energy barrier and reaction energy for water dissociation on CuO (111) are 218 kJ/mol and -30kJ/mol, respectively. The high reaction barrier indicates that without high-frequency ultrasound, it is unlikely for water to dissociate on the catalyst surface at 25 °C. The negative reaction free energy shows that the reaction is thermodynamically feasible. Also, it is significantly lower than non-catalytic dissociation energy of water, 492kJ/mol<sup>154</sup>, explaining that the presence of CuO significantly promotes water dissociation on its surface to form surface adsorbed H and OH groups, as shown in Figure 5.6. Since the hydroxyl in the reactant benzyl alcohol remains attached to the dissociated CHO group (in the DFT computed minimum energy pathway), the OH hydroxylating the phenyl ring to form phenol (in the final step of the pathway shown in Figure 5.5) has to originate from water, and the H from water is possibly utilized to form ethylene glycol via C-C coupling in the aldehyde groups, as elucidated later in the chapter 5.6. This is in agreement with the isotope labelling experiments that demonstrated the incorporation of OD from D<sub>2</sub>O into phenol. Hence, it can be conclusively said that in addition to catalyzing C-H activation, OH from water also incorporated itself into the aromatic ring after the C-C cleavage of benzaldehyde to form phenol.

According to *Amaniampong et al.*<sup>125</sup>, H<sub>2</sub>O<sub>2</sub> can also generate OH groups adsorbed on the CuO surface by dissociating into two OH fragments, catalyzed by CuO. The free energy of the formation of adsorbed OH species from hydrogen peroxide on CuO(111) is -28 kJ/mol and the activation barrier is only 22 kJ/mol, suggesting kinetic feasibility of the dissociation of H<sub>2</sub>O<sub>2</sub>

even without ultrasound irradiation. Hence, the reactions performed in the presence of  $\text{H}_2\text{O}_2$  under silent conditions at  $62^\circ\text{C}$  resulted in the formation of phenol ( $\sim 16\%$  yield) at a benzyl alcohol conversion of  $\sim 35\%$  within 2h of reaction irradiation time (Table B2, entry 3) and remained constant even up to 6 h the depletion of  $\text{H}_2\text{O}_2$ . The reaction free energies of dissociation of  $\text{H}_2\text{O}$  and  $\text{H}_2\text{O}_2$  on the catalyst surface indicate that the adsorbed OH group on the catalyst surface is highly exergonic and stable, which further confirms the experimental observation that the presence of CuO suppresses OH recombination (Figure 5.2) as OH would tend to be adsorbed on the catalyst surface.

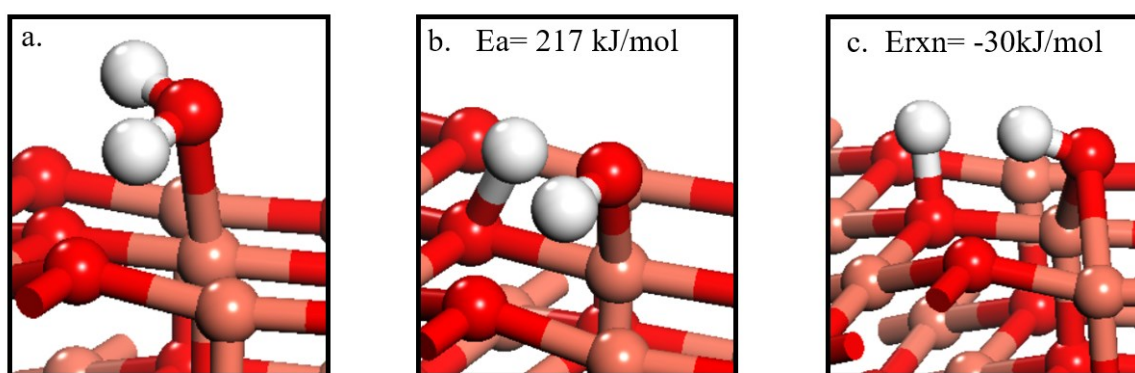


Figure 5.6 The configurations for (a) water molecule adsorbed on CuO (111); (b) transition state and (c) final state of water dissociation on CuO(111) surface. Activation free energy barriers and reaction free energies are indicated in kJ/mol. Salmon, red, and white balls represent copper (Cu), oxygen (O), and hydrogen (H) atoms, respectively

### 5.5 Benzaldehyde and hydroxy-benzyl alcohol reactions

Benzaldehyde and benzoic acid are often considered major products of benzyl alcohol oxidation<sup>99,102,155</sup>. However, a low yield of benzaldehyde ( $<3\%$ ) and no benzoic acid was observed in this work. Benzaldehyde is shown as a key intermediate species and phenol was still the major product with benzaldehyde as the reactant. An alternative pathway suggested for benzaldehyde is to form benzoic acid, as shown in Figure 5.4 and detailed reaction free energy diagram is presented in Appendix C. DFT computations were performed to investigate the pathway to phenol, via benzaldehyde oxidation to benzoic acid, followed by C-C cleavage between the acid group and the phenyl ring. The C-H activation barrier for benzaldehyde via

surface O is 93kJ/mol, followed by OH addition with the free energy barrier of 113kJ/mol, to form benzoic acid (Figure 5.4). Since these activation barriers are higher compared to the C-C cleavage pathway from benzaldehyde, it is unlikely for benzoic acid to be a reaction intermediate. However, if benzoic acid is the reactant, it would also convert to phenol via C-C cleavage on CuO, with the energy barrier of 96 kJ/mol, followed by the hydroxylation step, as shown before. The reason that C-C cleavage is more facile for both benzaldehyde and benzoic acid is that the aromatic ring is not able to interact strong enough with the metal oxide surface, and adsorption occurs via the aldehyde and acid groups.

With *para*-hydroxy-benzyl alcohol as the reactant, *para*-hydroxy-benzaldehyde and hydroquinone were observed as products in the experiments. This also suggests that hydroxy-benzyl alcohol goes through the same activation pathway as benzyl alcohol, irrespective of the additional hydroxyl group present on the aromatic ring. The adsorption configuration of *para*-hydroxy-benzyl alcohol on CuO (111) was investigated and the most stable adsorption configuration, as shown in Figure 5.7, was similar to the adsorption configuration for benzyl alcohol, via the alcohol group. The hydroxyl group on the aromatic ring does not interact with the catalyst surface and hence it would not affect the reaction mechanism.

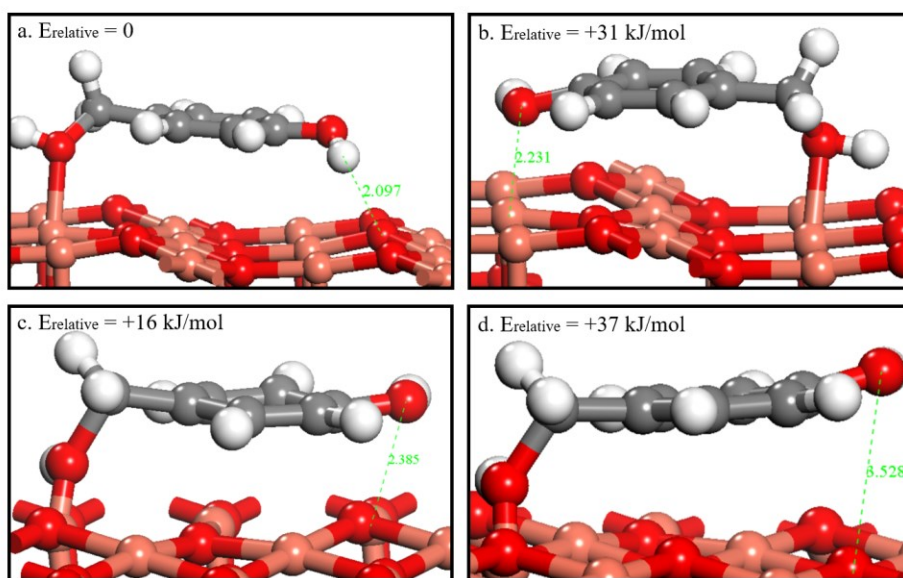


Figure 5.7. hydroxy-benzyl alcohol adsorption configurations on CuO (111) surface, as the relative energy reported compared to the most stable configuration as a., in kJ/mol. Salmon, red, grey, and white balls represent copper (Cu), oxygen (O), carbon (C) and hydrogen (H) atoms, respectively.



## 5.6 The formation of ethylene glycol as the side product

Figure 5.8 shows the free energy profile for the formation of ethylene glycol on CuO (111). The aldehyde group (CHO) left on the CuO (111) surface after the C-C cleavage of benzaldehyde would be hydrogenated first, with an activation barrier of 31kJ/mol and reaction energy of -20 kJ/mol, to form a CHOH group adsorbed on the catalytic surface. Then, two such groups with the staggered configurations (which is 38kJ/mol higher compared to the bridge configuration, in terms of the free energy, but it is feasible under the reaction conditions) would undergo C-C coupling to form (CHOH)<sub>2</sub>, with an energy barrier of 40kJ/mol and reaction energy of -94 kJ/mol. Two successive hydrogenations of (CHOH)<sub>2</sub> would result in the formation of ethylene glycol. Stoichiometrically, number of hydrogens needed to form ethylene glycol are more than what benzyl alcohol can provide and hence hydrogen atoms from water would be needed and will be incorporated in ethylene glycol. The first hydrogenation has a relatively high activation energy barrier of 284kJ/mol, whereas the second hydrogenation has a much lower activation barrier of 44kJ/mol and reaction free energy of -36kJ/mol, respectively.

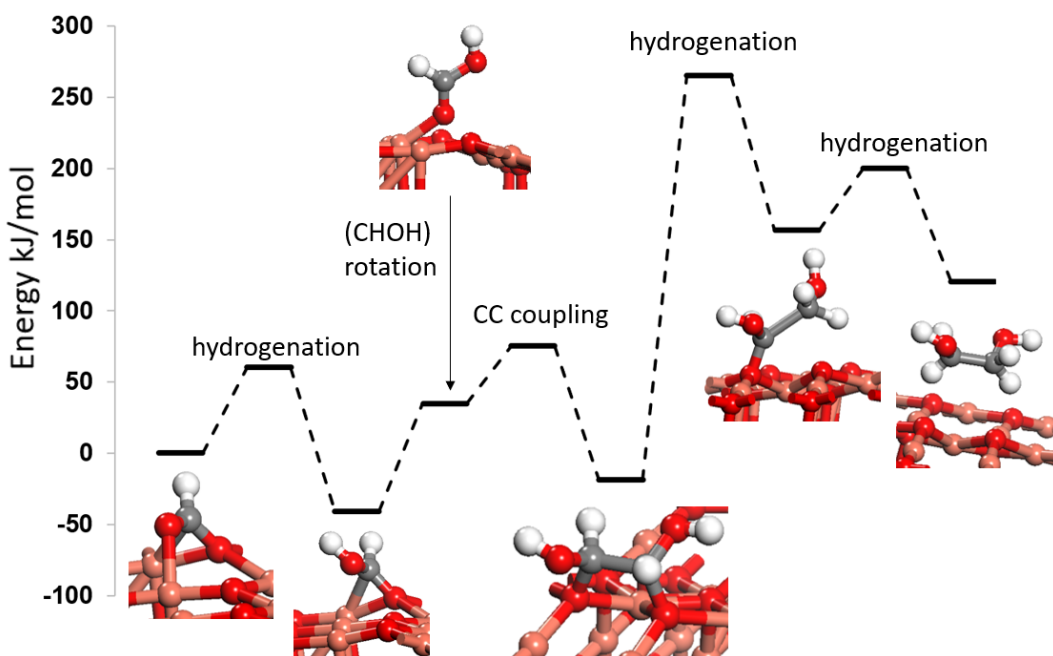


Figure 5.8. Free Energy profile for the formation ethylene glycol on CuO (111), from the aldehyde groups cleaved from benzaldehyde. Activation free energy barriers and reaction free energies are indicated in kJ/mol. Salmon, red, grey, and white balls represent copper (Cu), oxygen (O), carbon (C) and hydrogen (H) atoms, respectively.

In summary, using a synergistic combination of ultrasound and metal oxide catalysis, we demonstrated a novel approach to demethylate benzyl alcohol to phenol, at room temperature and using water as solvent. The reaction mechanism involves activation of OH and C-H bonds in benzyl alcohol to form adsorbed benzaldehyde as an intermediate, which further undergoes C-C cleavage to form the phenyl ring. The phenyl ring is then hydroxylated to form phenol. Unlike typical condensed phase catalytic chemistry where water is just a solvation medium and may play an indirect role in the chemistry by altering reaction kinetics and thermodynamics, we reveal that ultrasound induces water dissociation, and the copper oxide catalyst stabilizes the dissociated OH groups via adsorption. The adsorbed OH group plays a dual role; it activates the strong C-H bond and later gets incorporated into the phenyl ring during its hydroxylation. We also demonstrated that the reaction mechanism remains unchanged for *para*-hydroxyl-benzyl alcohol, producing hydroquinone.

## 6 Conclusions and Future Work

In Chapter 4, we combined experimental XPS data with the computational DFT+U method, to estimate the surface specific Hubbard U corrections for nickel and Cobalt oxide catalysts and to simultaneously screen and identify the adsorbate species corresponding to the binding energy shifts in the XPS spectra. U values of 2.0 eV and 3.0 eV can reproduce the experimental XPS O1s core level binding energy correctly for surface moieties on NiO and Co<sub>3</sub>O<sub>4</sub> surfaces. The bulk property optimized and commonly used U values fail to predict the experimentally observed XPS shifts and cannot identify adsorbates that correspond to those shifts. For both metal oxides, the DFT+U computed core level binding energy shifts have a monotonic relationship with the U values used. By comparing experimental and theoretical core level binding energy shifts across the entire U value range from 1 to 6 eV, the surface U value for NiO, 2eV helps to assign the experimentally observed shifts to adsorbed oxygen (+1.8 and +2.2eV), the surface oxygen connected to adsorbed hydrogen (+2.2eV) and adsorbed HCO<sub>2</sub> closed to a Ni vacancy site on NiO (100) surface. As for Co<sub>3</sub>O<sub>4</sub>, despite the disagreement on the bulk property optimized U value, ~3eV of U value could successfully predict the experimentally observed XPS shifts, and these shifts are also identified to the surface oxygen connected to adsorbed hydrogen, the oxygen connected to surface Co in adsorbed HCO<sub>3</sub> for +1.5eV and oxygens connected to C and Co in adsorbed HCO<sub>2</sub> for +2.6eV. The surface specific U values determined in this work should be adopted in the future investigation of surface catalyzed reactions on NiO and Co<sub>3</sub>O<sub>4</sub> surfaces, in order to accurately capture various surface-adsorbate interactions on the specific TMO catalyst surface. Meanwhile, the previously observed XPS shifts assigned based on DFT+U calculations can provide reliable guidelines for future investigations.

In Chapter 5, We utilized the U value optimized with the very same approach, 4eV for CuO, to investigate the water assisted sonocatalytic transformation of benzyl alcohol to phenol. We demonstrated that using a sonochemically synthesized CuO catalyst and water at 25 °C, benzyl alcohol oxidation reaction can be systematically steered towards a demethylenation to form phenol with synergistic experimental and theoretical methods. The synergistic combination of experimental and computational investigation provided insights on (i) the reaction mechanism of initial activation of O-H and C-H bonds in benzyl alcohol to form adsorbed benzaldehyde as an

intermediate, which further undergoes C-C cleavage and hydroxylation to form phenol; (ii) water dissociation induced by ultrasound, producing OH groups which are stabilized by CuO catalyst surface; (iii) the dual role of OH groups adsorbed on CuO surface, reducing the free energy barrier for C-H activation and incorporating itself into phenyl ring to form phenol.

The synergistic approach utilized in this work can be extended to advanced XPS techniques, such as in-situ XPS, for the identification of surface species present at reaction conditions throughout the reaction. Moreover, this work also shows such synergistic approach combining experimental XPS and computational DFT+U methods is applicable to different TMO surfaces, and potentially can be extended to complex mixed transition metal oxide systems. Also, the CuO catalyzed, environment friendly transformation of demethylation of benzyl alcohol reported can open avenues to demethylate lignin, which will make it more hydrophilic and will increase its reactivity to make its use as a feedstock for polymers and resins production more amenable.

## References

- 1 Bhola, K., Varghese, J. J., Dapeng, L., Liu, Y. & Mushrif, S. H. Influence of Hubbard U Parameter in Simulating Adsorption and Reactivity on CuO: Combined Theoretical and Experimental Study. *The Journal of Physical Chemistry C* **121**, 21343-21353 (2017).
- 2 Trinh, Q. T., Bhola, K., Amaniampong, P. N., Jérôme, F. & Mushrif, S. H. Synergistic Application of XPS and DFT to Investigate Metal Oxide Surface Catalysis. *The Journal of Physical Chemistry C* **122**, 22397-22406 (2018).
- 3 Hassan-Legault, K., Mohan, O. & Mushrif, S. H. Molecular insights into the activity and stability of popular methane reforming catalysts using quantum mechanical tools. *Current Opinion in Chemical Engineering* **26**, 38-45 (2019).
- 4 Ruiz Puigdollers, A., Schlexer, P., Tosoni, S. & Pacchioni, G. Increasing Oxide Reducibility: The Role of Metal/Oxide Interfaces in the Formation of Oxygen Vacancies. *ACS Catalysis* **7**, 6493-6513 (2017).
- 5 Korpelin, V., Melander, M. M. & Honkala, K. Reducing the Irreducible: Dispersed Metal Atoms Facilitate Reduction of Irreducible Oxides. *The Journal of Physical Chemistry C* **126**, 933-945 (2022).
- 6 Daelman, N. *et al.* Quasi-degenerate states and their dynamics in oxygen deficient reducible metal oxides. *The Journal of Chemical Physics* **152**, 050901 (2020).
- 7 Powell, C. J., Jablonski, A., Tilinin, I. S., Tanuma, S. & Penn, D. R. Surface sensitivity of Auger-electron spectroscopy and X-ray photoelectron spectroscopy. *Journal of Electron Spectroscopy and Related Phenomena* **98-99**, 1-15 (1999).
- 8 Teschner, D. *et al.* The roles of subsurface carbon and hydrogen in palladium-catalyzed alkyne hydrogenation.
- 9 Tao, F. F. & Salmeron, M. In situ studies of chemistry and structure of materials in reactive environments.
- 10 Trinh, Q. T., Tan, K. F., Borgna, A. & Saeys, M. Evaluating the Structure of Catalysts Using Core-Level Binding Energies Calculated from First Principles. *The Journal of Physical Chemistry C* **117**, 1684-1691 (2013).
- 11 Cohen, A. J., Mori-Sánchez, P. & Yang, W. Challenges for Density Functional Theory. *Chemical Reviews* **112**, 289-320 (2012).
- 12 Dudarev, S. L., Botton, G. A., Savrasov, S. Y., Humphreys, C. J. & Sutton, A. P. Electron-energy-loss spectra and the structural stability of nickel oxide: An LSDA+U study. *Physical Review B* **57**, 1505-1509 (1998).
- 13 Anisimov, V. I., Zaanen, J. & Andersen, O. K. Band theory and Mott insulators: Hubbard U instead of Stoner I. *Physical Review B* **44**, 943-954 (1991).
- 14 Capdevila-Cortada, M., Łodziana, Z. & López, N. Performance of DFT+U Approaches in the Study of Catalytic Materials. *ACS Catalysis* **6**, 8370-8379 (2016).
- 15 Nakamura, K., Arita, R., Yoshimoto, Y. & Tsuneyuki, S. First-principles calculation of effective onsite Coulomb interactions of 3d transition metals: Constrained local density functional approach with maximally localized Wannier functions. *Physical Review B* **74**, 235113 (2006).
- 16 Qiu, R., Ao, B. & Huang, L. Effective Coulomb interaction in actinides from linear response approach. *Computational Materials Science* **171**, 109270 (2020).
- 17 Deraz, N. M., Selim, M. M. & Ramadan, M. Processing and properties of nanocrystalline Ni and NiO catalysts. *Materials Chemistry and Physics* **113**, 269-275 (2009).

- 18 Liu, L. *et al.* Activating peroxydisulfate by morphology-dependent NiO catalysts: Structural origin of different catalytic properties. *Applied Catalysis B: Environmental* **256**, 117806 (2019).
- 19 Zhu, H. *et al.* Metal oxides modified NiO catalysts for oxidative dehydrogenation of ethane to ethylene. *Catalysis Today* **228**, 58-64 (2014).
- 20 Meshkani, F. & Rezaei, M. Mesoporous Ba-promoted chromium free Fe<sub>2</sub>O<sub>3</sub>-Al<sub>2</sub>O<sub>3</sub>-NiO catalyst with low methanation activity for high temperature water gas shift reaction. *Catalysis Communications* **58**, 26-29 (2015).
- 21 He, Z. *et al.* Water-Enhanced Synthesis of Higher Alcohols from CO<sub>2</sub> Hydrogenation over a Pt/Co<sub>3</sub>O<sub>4</sub> Catalyst under Milder Conditions. *Angewandte Chemie International Edition* **55**, 737-741 (2016).
- 22 Ma, C. Y. *et al.* Mesoporous Co<sub>3</sub>O<sub>4</sub> and Au/Co<sub>3</sub>O<sub>4</sub> Catalysts for Low-Temperature Oxidation of Trace Ethylene. *Journal of the American Chemical Society* **132**, 2608-2613 (2010).
- 23 Yao, J. *et al.* Facet-Dependent Activity of Co<sub>3</sub>O<sub>4</sub> Catalyst for C<sub>3</sub>H<sub>8</sub> Combustion. *ChemCatChem* **11**, 5570-5579 (2019).
- 24 Kim, K. S. & Davis, R. E. Electron spectroscopy of the nickel-oxygen system. *Journal of Electron Spectroscopy and Related Phenomena* **1**, 251-258 (1972).
- 25 Kim, K. S. & Winograd, N. X-ray photoelectron spectroscopic studies of nickel-oxygen surfaces using oxygen and argon ion-bombardment. *Surface Science* **43**, 625-643 (1974).
- 26 Furstenau, R. P., McDougall, G. & Langell, M. A. Initial stages of hydrogen reduction of NiO(100). *Surface Science* **150**, 55-79 (1985).
- 27 Wulser, K. W. & Langell, M. A. Carboxylic acid adsorption on NiO(100) characterized by X-ray photoelectron and high resolution electron energy loss spectroscopies. *Catalysis Letters* **15**, 39-50 (1992).
- 28 Mansour, A. N. Characterization of NiO by XPS. *Surface Science Spectra* **3**, 231-238, doi:10.1116/1.1247751 (1994).
- 29 Peck, M. A. & Langell, M. A. Comparison of Nanoscaled and Bulk NiO Structural and Environmental Characteristics by XRD, XAFS, and XPS. *Chemistry of Materials* **24**, 4483-4490 (2012).
- 30 Uhlenbrock, S., Scharfschwerdt, C., Neumann, M., Illing, G. & Freund, H. J. The influence of defects on the Ni 2p and O 1s XPS of NiO. *Journal of Physics: Condensed Matter* **4**, 7973-7978 (1992).
- 31 Dupin, J.-C., Gonbeau, D., Vinatier, P. & Levasseur, A. Systematic XPS studies of metal oxides, hydroxides and peroxides. *Physical Chemistry Chemical Physics* **2**, 1319-1324 (2000).
- 32 Fleisch, T., Winograd, N. & Delgass, W. N. Chemisorption of oxygen on Ni(100) by SIMS and XPS. *Surface Science* **78**, 141-158 (1978).
- 33 Zhang, T. *et al.* Engineering oxygen vacancy on NiO nanorod arrays for alkaline hydrogen evolution. *Nano Energy* **43**, 103-109 (2018).
- 34 Biesinger, M. C., Payne, B. P., Lau, L. W. M., Gerson, A. & Smart, R. S. C. X-ray photoelectron spectroscopic chemical state quantification of mixed nickel metal, oxide and hydroxide systems. *Surface and Interface Analysis* **41**, 324-332 (2009).
- 35 Roberts, M. W. & Smart, R. S. C. The defect structure of nickel oxide surfaces as revealed by photoelectron spectroscopy. *Journal of the Chemical Society, Faraday Transactions 1: Physical Chemistry in Condensed Phases* **80**, 2957-2968 (1984).

- 36 Tomellini, M. X-ray photoelectron spectra of defective nickel oxide. *Journal of the Chemical Society, Faraday Transactions 1: Physical Chemistry in Condensed Phases* **84**, 3501-3510 (1988).
- 37 Kolotykin, Y. M. *et al.* High-spin configuration of Co(III) in nonstoichiometric Co<sub>3</sub>O<sub>4</sub> films. XPS investigations. *Materials Chemistry and Physics* **11**, 29-48 (1984).
- 38 Haber, J., Stoch, J. & Ungier, L. X-ray photoelectron spectra of oxygen in oxides of Co, Ni, Fe and Zn. *Journal of Electron Spectroscopy and Related Phenomena* **9**, 459-467 (1976).
- 39 Chuang, T. J., Brundle, C. R. & Rice, D. W. Interpretation of the x-ray photoemission spectra of cobalt oxides and cobalt oxide surfaces. *Surface Science* **59**, 413-429 (1976).
- 40 Petitto, S. C. & Langell, M. A. Surface composition and structure of Co<sub>3</sub>O<sub>4</sub>(110) and the effect of impurity segregation. *Journal of Vacuum Science & Technology A* **22**, 1690-1696 (2004).
- 41 McIntyre, N. S., Johnston, D. D., Coatsworth, L. L., Davidson, R. D. & Brown, J. R. X-ray photoelectron spectroscopic studies of thin film oxides of cobalt and molybdenum. *Surface and Interface Analysis* **15**, 265-272 (1990).
- 42 Gajardo, P., Pirotte, D., Defosse, C., Grange, P. & Delmon, B. XPS study of the supported phase — SiO<sub>2</sub> interaction in Mo/SiO<sub>2</sub> and CoMo/SiO<sub>2</sub> hydrodesulphurization catalysts in their oxidic precursor form. *Journal of Electron Spectroscopy and Related Phenomena* **17**, 121-135 (1979).
- 43 Wagner, C. D., Zatko, D. A. & Raymond, R. H. Use of the oxygen KLL Auger lines in identification of surface chemical states by electron spectroscopy for chemical analysis. *Analytical Chemistry* **52**, 1445-1451 (1980).
- 44 Tyuliev, G. & Angelov, S. The nature of excess oxygen in Co<sub>3</sub>O<sub>4</sub>+ $\epsilon$ . *Applied Surface Science* **32**, 381-391 (1988).
- 45 Tan, B. J., Klabunde, K. J. & Sherwood, P. M. A. XPS studies of solvated metal atom dispersed (SMAD) catalysts. Evidence for layered cobalt-manganese particles on alumina and silica. *Journal of the American Chemical Society* **113**, 855-861 (1991).
- 46 Edla, R. *et al.* Study of Gaseous Interactions on Co<sub>3</sub>O<sub>4</sub> Thin Film Coatings by Ambient Pressure Soft X-ray Absorption Spectroscopy. *The Journal of Physical Chemistry C* **123**, 24511-24519 (2019).
- 47 Xu, H. *et al.* Synthesis and Microwave Absorption Properties of Core-Shell Structured Co<sub>3</sub>O<sub>4</sub>-PANI Nanocomposites. *Journal of Nanomaterials* **2015**, 845983 (2015).
- 48 Mate, V. R., Shirai, M. & Rode, C. V. Heterogeneous Co<sub>3</sub>O<sub>4</sub> catalyst for selective oxidation of aqueous veratryl alcohol using molecular oxygen. *Catalysis Communications* **33**, 66-69 (2013).
- 49 Xu, J. *et al.* Co<sub>3</sub>O<sub>4</sub> nanocubes homogeneously assembled on few-layer graphene for high energy density lithium-ion batteries. *Journal of Power Sources* **274**, 816-822 (2015).
- 50 Zheng, Y., Liu, Y., Zhou, H., Huang, W. & Pu, Z. Complete combustion of methane over Co<sub>3</sub>O<sub>4</sub> catalysts: Influence of pH values. *Journal of Alloys and Compounds* **734**, 112-120 (2018).
- 51 Cole, K. M., Kirk, D. W. & Thorpe, S. J. Co<sub>3</sub>O<sub>4</sub> nanoparticles characterized by XPS and UPS. *Surface Science Spectra* **28**, 014001 (2021).

- 52 Bennett, L. J. & Jones, G. The influence of the Hubbard U parameter in simulating the catalytic behaviour of cerium oxide. *Physical Chemistry Chemical Physics* **16**, 21032-21038 (2014).
- 53 Huang, M. & Fabris, S. CO Adsorption and Oxidation on Ceria Surfaces from DFT+U Calculations. *The Journal of Physical Chemistry C* **112**, 8643-8648 (2008).
- 54 Hu, W., Cao, X.-M. & Hu, P. DFT+U Study on Catalysis by Co<sub>3</sub>O<sub>4</sub>: Influence of U Value and a Surface–Bulk Bi-U Strategy. *The Journal of Physical Chemistry C* **122**, 19593-19602 (2018).
- 55 Maimaiti, Y., Nolan, M. & Elliott, S. D. Reduction mechanisms of the CuO(111) surface through surface oxygen vacancy formation and hydrogen adsorption. *Physical Chemistry Chemical Physics* **16**, 3036-3046 (2014).
- 56 Mishra, A. K., Roldan, A. & de Leeuw, N. H. CuO Surfaces and CO<sub>2</sub> Activation: A Dispersion-Corrected DFT+U Study. *The Journal of Physical Chemistry C* **120**, 2198-2214 (2016).
- 57 Nolan, M. & Elliott, S. D. The p-type conduction mechanism in Cu<sub>2</sub>O: a first principles study. *Physical Chemistry Chemical Physics* **8**, 5350-5358 (2006).
- 58 Wang, L., Maxisch, T. & Ceder, G. Oxidation energies of transition metal oxides within the GGA+U framework. *Physical Review B* **73**, 195107 (2006).
- 59 Song, Y.-Y. & Wang, G.-C. A DFT Study and Microkinetic Simulation of Propylene Partial Oxidation on CuO (111) and CuO (100) Surfaces. *The Journal of Physical Chemistry C* **120**, 27430-27442 (2016).
- 60 Latimer, A. A. *et al.* Understanding trends in C-H bond activation in heterogeneous catalysis.
- 61 Tyo, E. C. *et al.* Oxidative Dehydrogenation of Cyclohexane on Cobalt Oxide (Co<sub>3</sub>O<sub>4</sub>) Nanoparticles: The Effect of Particle Size on Activity and Selectivity. *ACS Catalysis* **2**, 2409-2423 (2012).
- 62 Atzkern, S. *et al.* Valence-band excitations in  $\{\mathrm{V}\}_2\{\mathrm{O}\}_5$ . *Physical Review B* **61**, 12792-12798 (2000).
- 63 Fu, G., Chen, Z.-N., Xu, X. & Wan, H.-L. Understanding the Reactivity of the Tetrahedrally Coordinated High-Valence d<sub>0</sub> Transition Metal Oxides toward the C–H Bond Activation of Alkanes: A Cluster Model Study. *The Journal of Physical Chemistry A* **112**, 717-721 (2008).
- 64 Varghese, J. J. & Mushrif, S. H. Insights into the C–H Bond Activation on NiO Surfaces: The Role of Nickel and Oxygen Vacancies and of Low Valent Dopants on the Reactivity and Energetics. *The Journal of Physical Chemistry C* **121**, 17969-17981, doi:10.1021/acs.jpcc.7b05226 (2017).
- 65 Ghosh, P., Senthilarasu, S., Nixon, T. & Krishnamurthy, S. in *Reference Module in Materials Science and Materials Engineering* (Elsevier, 2016).
- 66 Mishra, R., Militky, J. & Venkataraman, M. in *Nanotechnology in Textiles* (eds Rajesh Mishra & Jiri Militky) 35-161 (Woodhead Publishing, 2019).
- 67 Fang, H., Haibin, L. & Zengli, Z. Advancements in Development of Chemical-Looping Combustion: A Review. *International Journal of Chemical Engineering* **2009**, 710515 (2009).
- 68 Dong, H. *et al.* Excellent oxygen evolution reaction of NiO with a layered nanosphere structure as the cathode of lithium–oxygen batteries. *RSC Advances* **8**, 3357-3363 (2018).



- 69 Silvester, L. *et al.* NiO supported on Al<sub>2</sub>O<sub>3</sub> and ZrO<sub>2</sub> oxygen carriers for chemical looping steam methane reforming. *International Journal of Hydrogen Energy* **40**, 7490-7501 (2015).
- 70 Li, L. & Kanai, Y. Antiferromagnetic structures and electronic energy levels at reconstructed NiO(111) surfaces: A  $\text{DFT}+\text{U}$  study. *Physical Review B* **91**, 235304 (2015).
- 71 Rohrbach, A., Hafner, J. & Kresse, G. Molecular adsorption on the surface of strongly correlated transition-metal oxides: A case study for CO/NiO(100). *Physical Review B* **69**, 075413 (2004).
- 72 Ebensperger, C. & Meyer, B. First-principles study of the reconstruction and hydroxylation of the polar NiO(111) surface. *physica status solidi (b)* **248**, 2229-2241 (2011).
- 73 Zhang, W.-B. & Tang, B.-Y. Stability of the polar NiO(111) surface. *The Journal of Chemical Physics* **128**, 124703 (2008).
- 74 Kwapien, K., Piccinin, S. & Fabris, S. Energetics of Water Oxidation Catalyzed by Cobalt Oxide Nanoparticles: Assessing the Accuracy of DFT and DFT+U Approaches against Coupled Cluster Methods. *The Journal of Physical Chemistry Letters* **4**, 4223-4230 (2013).
- 75 Dalverny, A. L., Filhol, J. S., Lemoigno, F. & Doublet, M. L. Interplay between Magnetic and Orbital Ordering in the Strongly Correlated Cobalt Oxide: A DFT+U Study. *The Journal of Physical Chemistry C* **114**, 21750-21756 (2010).
- 76 Wöllenstein, J. *et al.* Cobalt oxide based gas sensors on silicon substrate for operation at low temperatures. *Sensors and Actuators B: Chemical* **93**, 442-448 (2003).
- 77 Jin, S. *et al.* Thousandfold Change in Resistivity in Magnetoresistive La-Ca-Mn-O Films. *Science* **264**, 413-415 (1994).
- 78 Raquet, B. *et al.* Preparation and magnetic properties of the CoO/Co bilayer. *Journal of Magnetism and Magnetic Materials* **184**, 41-48 (1998).
- 79 Poizot, P., Laruelle, S., Grugeon, S., Dupont, L. & Tarascon, J. M. Nano-sized transition-metal oxides as negative-electrode materials for lithium-ion batteries. *Nature* **407**, 496-499 (2000).
- 80 Haneda, M., Kintaichi, Y., Bion, N. & Hamada, H. Alkali metal-doped cobalt oxide catalysts for NO decomposition. *Applied Catalysis B: Environmental* **46**, 473-482 (2003).
- 81 Thormählen, P., Skoglundh, M., Fridell, E. & Andersson, B. Low-Temperature CO Oxidation over Platinum and Cobalt Oxide Catalysts. *Journal of Catalysis* **188**, 300-310 (1999).
- 82 Pollard, M. J. *et al.* A mechanistic study of the low-temperature conversion of carbon monoxide to carbon dioxide over a cobalt oxide catalyst. *Journal of Catalysis* **254**, 218-225 (2008).
- 83 Chen, J. & Selloni, A. Water Adsorption and Oxidation at the Co<sub>3</sub>O<sub>4</sub> (110) Surface. *The Journal of Physical Chemistry Letters* **3**, 2808-2814 (2012).
- 84 Chen, J., Wu, X. & Selloni, A. Electronic structure and bonding properties of cobalt oxide in the spinel structure. *Physical Review B* **83**, 245204 (2011).
- 85 Chen, J. & Selloni, A. Electronic states and magnetic structure at the Co<sub>3</sub>O<sub>4</sub>(110) surface: A first-principles study. *Physical Review B* **85**, 085306 (2012).
- 86 Yan, G. & Sautet, P. Surface Structure of Co<sub>3</sub>O<sub>4</sub> (111) under Reactive Gas-Phase Environments. *ACS Catalysis* **9**, 6380-6392 (2019).

- 87 Selcuk, S. & Selloni, A. DFT+U Study of the Surface Structure and Stability of Co<sub>3</sub>O<sub>4</sub>(110): Dependence on U. *The Journal of Physical Chemistry C* **119**, 9973-9979 (2015).
- 88 Pang, X.-Y., Liu, C., Li, D.-C., Lv, C.-Q. & Wang, G.-C. Structure Sensitivity of CO Oxidation on Co<sub>3</sub>O<sub>4</sub>: A DFT Study. *ChemPhysChem* **14**, 204-212 (2013).
- 89 Singh, V., Kosa, M., Majhi, K. & Major, D. T. Putting DFT to the Test: A First-Principles Study of Electronic, Magnetic, and Optical Properties of Co<sub>3</sub>O<sub>4</sub>. *Journal of Chemical Theory and Computation* **11**, 64-72 (2015).
- 90 Amaniampong, P. N. *et al.* Synergistic effect of high-frequency ultrasound with cupric oxide catalyst resulting in a selectivity switch in glucose oxidation under argon. *Journal of the American Chemical Society* **141**, 14772-14779 (2019).
- 91 Bhangu, S. K., Bocchinfuso, G., Ashokkumar, M. & Cavalieri, F. Sound-driven dissipative self-assembly of aromatic biomolecules into functional nanoparticles. *Nanoscale Horizons* **5**, 553-563 (2020).
- 92 Manariotis, I. D., Karapanagioti, H. K. & Chrysikopoulos, C. V. Degradation of PAHs by high frequency ultrasound. *Water Research* **45**, 2587-2594 (2011).
- 93 Juliano, P. *et al.* Extraction of olive oil assisted by high-frequency ultrasound standing waves. *Ultrasonics sonochemistry* **38**, 104-114 (2017).
- 94 Amaniampong, P. N. *et al.* Selective and catalyst-free oxidation of D-glucose to D-glucuronic acid induced by high-frequency ultrasound. *Scientific reports* **7**, 1-8 (2017).
- 95 Amaniampong, P. N. *et al.* Catalyst-Free Synthesis of Alkylpolyglycosides Induced by High-Frequency Ultrasound. *ChemSusChem* **11**, 2673-2676 (2018).
- 96 Amaniampong, P. N. & Jérôme, F. Catalysis under ultrasonic irradiation: a sound synergy. *Current opinion in green and sustainable chemistry* **22**, 7-12 (2020).
- 97 Mei, H. *et al.* Sono-Fenton Chemistry Converts Phenol and Phenyl Derivatives into Polyphenols for Engineering Surface Coatings. *Angewandte Chemie* **133**, 21699-21705 (2021).
- 98 Humblot, A. *et al.* Conversion of Ammonia to Hydrazine Induced by High-Frequency Ultrasound. *Angewandte Chemie* **133**, 25434-25438 (2021).
- 99 Li, H. *et al.* New reaction pathway induced by plasmon for selective benzyl alcohol oxidation on BiOCl possessing oxygen vacancies. *Journal of the American Chemical Society* **139**, 3513-3521 (2017).
- 100 Seddon, K. R. & Stark, A. Selective catalytic oxidation of benzyl alcohol and alkylbenzenes in ionic liquids. *Green chemistry* **4**, 119-123 (2002).
- 101 Vannucci, A. K. *et al.* Water oxidation intermediates applied to catalysis: Benzyl alcohol oxidation. *J.AM.Chem.Soc* **134**, 3972-3975 (2012).
- 102 Marinescu, L. G. & Bols, M. Very high rate enhancement of benzyl alcohol oxidation by an artificial enzyme. *Angewandte Chemie* **118**, 4706-4709 (2006).
- 103 Amaniampong, P. N. *et al.* Unraveling the mechanism of the oxidation of glycerol to dicarboxylic acids over a sonochemically synthesized copper oxide catalyst. *Green Chemistry* **20**, 2730-2741 (2018).
- 104 Amaniampong, P. N., Trinh, Q. T., Bahry, T., Zhang, J. & Jérôme, F. Ultrasonic-assisted oxidation of cellulose to oxalic acid over gold nanoparticles supported on iron-oxide. *Green Chemistry* **24**, 4800-4811 (2022).
- 105 Amaniampong, P. N. *et al.* Synergistic Effect of High-Frequency Ultrasound with Cupric Oxide Catalyst Resulting in a Selectivity Switch in Glucose Oxidation under Argon.

- Journal of the American Chemical Society* **141**, 14772-14779, doi:10.1021/jacs.9b06824 (2019).
- 106 Hohenberg, P. & Kohn, W. Inhomogeneous Electron Gas. *Physical Review* **136**, B864-B871 (1964).
- 107 Thomas, L. H. The calculation of atomic fields. *Mathematical Proceedings of the Cambridge Philosophical Society* **23**, 542-548 (1927).
- 108 Fermi, E. Un metodo statistico per la determinazione di alcune priorieta dell'atomo. *Rend Accad Naz Lincei* **6**, 602-607 (1927).
- 109 Kohn, W. & Sham, L. J. Self-Consistent Equations Including Exchange and Correlation Effects. *Physical Review* **140**, A1133-A1138 (1965).
- 110 Perdew, J. P., Burke, K. & Ernzerhof, M. Generalized Gradient Approximation Made Simple. *Physical Review Letters* **77**, 3865-3868 (1996).
- 111 Evarestov, R. A. & Smirnov, V. P. Special points of the brillouin zone and their use in the solid state theory. *physica status solidi (b)* **119**, 9-40 (1983).
- 112 Seidl, A., Görling, A., Vogl, P., Majewski, J. A. & Levy, M. Generalized Kohn-Sham schemes and the band-gap problem. *Physical Review B* **53**, 3764-3774 (1996).
- 113 Himmetoglu, B., Floris, A., de Gironcoli, S. & Cococcioni, M. Hubbard-corrected DFT energy functionals: The LDA+U description of correlated systems. *International Journal of Quantum Chemistry* **114**, 14-49 (2014).
- 114 Rohrbach, A., Hafner, J. & Kresse, G. Electronic correlation effects in transition-metal sulfides. *Journal of Physics Condensed Matter* **15**, 979-996 (2003).
- 115 Kresse, G. & Furthmüller, J. Efficiency of ab-initio total energy calculations for metals and semiconductors using a plane-wave basis set. *Computational Materials Science* **6**, 15-50 (1996).
- 116 Kresse, G. & Furthmüller, J. Efficient iterative schemes for ab initio total-energy calculations using a plane-wave basis set. *Physical Review B* **54**, 11169-11186 (1996).
- 117 Kresse, G. & Hafner, J. Norm-conserving and ultrasoft pseudopotentials for first-row and transition elements. *Journal of Physics: Condensed Matter* **6**, 8245-8257 (1994).
- 118 Kresse, G. & Joubert, D. From ultrasoft pseudopotentials to the projector augmented-wave method. *Physical Review B* **59**, 1758-1775 (1999).
- 119 Kresse, G. & Hafner, J. Ab initio molecular dynamics for liquid metals. *Physical Review B* **47**, 558-561, doi:10.1103/PhysRevB.47.558 (1993).
- 120 Blöchl, P. E. Projector augmented-wave method. *Physical Review B* **50**, 17953-17979 (1994).
- 121 Henkelman, G. & Jónsson, H. Improved tangent estimate in the nudged elastic band method for finding minimum energy paths and saddle points. *The Journal of Chemical Physics* **113**, 9978-9985 (2000).
- 122 Jónsson, H., Mills, G. & Jacobsen, K. W. Nudged elastic band method for finding minimum energy paths of transitions. (1998).
- 123 Henkelman, G., Uberuaga, B. P. & Jónsson, H. A climbing image nudged elastic band method for finding saddle points and minimum energy paths. *The Journal of Chemical Physics* **113**, 9901-9904 (2000).
- 124 Sheppard, D., Terrell, R. & Henkelman, G. Optimization methods for finding minimum energy paths. *The Journal of Chemical Physics* **128**, 134106 (2008).

- 125 Amaniampong, P. N. *et al.* Biomass Oxidation: Formyl C-H Bond Activation by the Surface Lattice Oxygen of Regenerative CuO Nanoleaves. *Angewandte Chemie* **127**, 9056-9061 (2015).
- 126 Malcolm W. Chase, Jr. *NIST-JANAF thermochemical tables*. (Fourth edition. Washington, DC : American Chemical Society ; New York : American Institute of Physics for the National Institute of Standards and Technology, 1998., 1998).
- 127 Wang, Y. *et al.* Reduced Mesoporous Co<sub>3</sub>O<sub>4</sub> Nanowires as Efficient Water Oxidation Electrocatalysts and Supercapacitor Electrodes. *Advanced Energy Materials* **4**, 1400696 (2014).
- 128 Cai, Z. *et al.* Single-Crystalline Ultrathin Co<sub>3</sub>O<sub>4</sub> Nanosheets with Massive Vacancy Defects for Enhanced Electrocatalysis. *Advanced Energy Materials* **8**, 1701694 (2018).
- 129 Xie, X., Li, Y., Liu, Z.-Q., Haruta, M. & Shen, W. Low-temperature oxidation of CO catalysed by Co<sub>3</sub>O<sub>4</sub> nanorods. *Nature* **458**, 746-749 (2009).
- 130 Teng, Y., Kusano, Y., Azuma, M., Haruta, M. & Shimakawa, Y. Morphology effects of Co<sub>3</sub>O<sub>4</sub> nanocrystals catalyzing CO oxidation in a dry reactant gas stream. *Catalysis Science & Technology* **1**, 920-922 (2011).
- 131 Liu, Y. *et al.* Surface oxygen Vacancies on Reduced Co<sub>3</sub>O<sub>4</sub>(100): Superoxide Formation and Ultra-Low-Temperature CO Oxidation. *Angewandte Chemie International Edition* **60**, 16514-16520 (2021).
- 132 Zasada, F. *et al.* Reactive Oxygen Species on the (100) Facet of Cobalt Spinel Nanocatalyst and their Relevance in 16O<sub>2</sub>/18O<sub>2</sub> Isotopic Exchange, deN<sub>2</sub>O, and deCH<sub>4</sub> Processes—A Theoretical and Experimental Account. *ACS Catalysis* **5**, 6879-6892 (2015).
- 133 Zhang, Z. *et al.* Facet-Dependent Cobalt Ion Distribution on the Co<sub>3</sub>O<sub>4</sub> Nanocatalyst Surface. *The Journal of Physical Chemistry Letters* **11**, 9913-9919 (2020).
- 134 Arman, M. A., Merte, L. R., Lundgren, E. & Knudsen, J. Co<sub>3</sub>O<sub>4</sub>(100) films grown on Ag(100): Structure and chemical properties. *Surface Science* **657**, 90-95 (2017).
- 135 Hashim, A. H., Zayed, A. O. H., Zain, S. M., Lee, V. S. & Said, S. M. Electronic, magnetic and structural properties of Co<sub>3</sub>O<sub>4</sub> (100) surface: a DFT+U study. *Applied Surface Science* **427**, 1090-1095 (2018).
- 136 Ragauskas, A. J. *et al.* Lignin valorization: improving lignin processing in the biorefinery. *science* **344**, 1246843 (2014).
- 137 Zakzeski, J., Bruijninx, P. C., Jongerius, A. L. & Weckhuysen, B. M. The catalytic valorization of lignin for the production of renewable chemicals. *Chemical reviews* **110**, 3552-3599 (2010).
- 138 Xu, C., Arancon, R. A. D., Labidi, J. & Luque, R. Lignin depolymerisation strategies: towards valuable chemicals and fuels. *Chemical Society Reviews* **43**, 7485-7500 (2014).
- 139 Tuck, C. O., Pérez, E., Horváth, I. T., Sheldon, R. A. & Poliakoff, M. Valorization of biomass: deriving more value from waste. *Science* **337**, 695-699 (2012).
- 140 Hanson, S. K. *et al.* Aerobic oxidation of pinacol by vanadium (V) dipicolinate complexes: evidence for reduction to vanadium (III). *J.AM.Chem.Soc* **131**, 428-429 (2009).
- 141 Nichols, J. M., Bishop, L. M., Bergman, R. G. & Ellman, J. A. Catalytic C–O bond cleavage of 2-aryloxy-1-arylethanol and its application to the depolymerization of lignin-related polymers. *J.AM.Chem.Soc* **132**, 12554-12555 (2010).

- 142 Son, S. & Toste, F. D. Non-Oxidative Vanadium-Catalyzed C–O Bond Cleavage: Application to Degradation of Lignin Model Compounds. *Angewandte Chemie International Edition* **49**, 3791-3794 (2010).
- 143 Sanderson, K. Lignocellulose: a chewy problem. *Nature* **474**, S12-S14 (2011).
- 144 Kim, K. H. *et al.* Tandem conversion of lignin to catechols via demethylation and catalytic hydrogenolysis. *Industrial Crops and Products* **159**, 113095 (2021).
- 145 Santos, R. B., Hart, P., Jameel, H. & Chang, H.-m. Wood based lignin reactions important to the biorefinery and pulp and paper industries. *BioResources* **8**, 1456-1477 (2013).
- 146 Partenheimer, W. The aerobic oxidative cleavage of lignin to produce hydroxyaromatic benzaldehydes and carboxylic acids via metal/bromide catalysts in acetic acid/water mixtures. *Advanced Synthesis & Catalysis* **351**, 456-466 (2009).
- 147 Chan, J. M. *et al.* Studies on the vanadium-catalyzed nonoxidative depolymerization of *Miscanthus giganteus*-derived lignin. *Acs Catalysis* **3**, 1369-1377 (2013).
- 148 Lundquist, K. in *Methods in lignin chemistry* 289-300 (Springer, 1992).
- 149 Kobayashi, H., Ohta, H. & Fukuoka, A. Conversion of lignocellulose into renewable chemicals by heterogeneous catalysis. *Catalysis Science & Technology* **2**, 869-883 (2012).
- 150 Gong, C. & Hart, D. P. Ultrasound induced cavitation and sonochemical yields. *The Journal of the Acoustical Society of America* **104**, 2675-2682 (1998).
- 151 Haouache, S. *et al.* Selective radical depolymerization of cellulose to glucose induced by high frequency ultrasound. *Chemical science* **11**, 2664-2669 (2020).
- 152 Didenko, Y. T., Nastich, D., Pugach, S., Polovinka, Y. & Kvochka, V. The effect of bulk solution temperature on the intensity and spectra of water sonoluminescence. *Ultrasonics* **32**, 71-76 (1994).
- 153 Beguin, E. *et al.* Direct Evidence of Multibubble Sonoluminescence Using Therapeutic Ultrasound and Microbubbles.
- 154 Boyarkin, O. V. *et al.* Accurate bond dissociation energy of water determined by triple-resonance vibrational spectroscopy and ab initio calculations. *Chemical Physics Letters* **568-569**, 14-20 (2013).
- 155 Crombie, C. M. *et al.* Enhanced selective oxidation of benzyl alcohol via in situ H<sub>2</sub>O<sub>2</sub> production over supported Pd-based catalysts. *ACS Catalysis* **11**, 2701-2714 (2021).

## Appendix A Figures and tables regarding the Oxygen in Surface Adsorbates

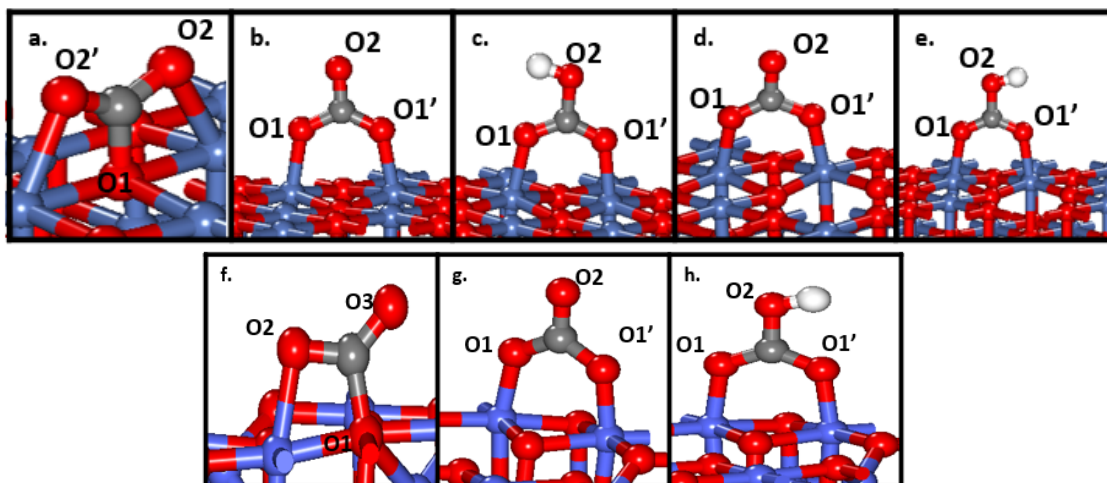


Figure A1. Structure of various surface adsorbates on NiO (100) surface evaluated to comparing with experimental XPS core level binding energy shifts. (a)adsCO<sub>2</sub> (b)adsCO<sub>3</sub>, (c)adsHCO<sub>3</sub> and (d)adsCO<sub>3</sub> near Ni vacancy site (e)adsHCO<sub>3</sub> near Ni vacancy site. Structure of various surface adsorbates on Co<sub>3</sub>O<sub>4</sub> (100) surface evaluated to comparing with experimental XPS core level binding energy shifts. (f)adsCO<sub>2</sub> (g)adsCO<sub>3</sub> and (h)adsHCO<sub>3</sub>. Dark blue, light blue, red, grey, and white balls represent nickel (Ni), cobalt (Co), oxygen (O), carbon (C) and hydrogen (H) atoms, respectively.

Table A1. O1s Core-level Binding Energy Shifts Relative to the O1s Core-level Binding Energy of Bulk Lattice Oxygen for Different Surface Adsorbates (corresponding to Fig. A1) on NiO (100) evaluated at U value of 5.3eV and 2eV

Structure	Specific oxygen that are used in for DFT calculation (Labelling indicated in Figure A1.)	DFT-calculated O1s core-level binding energy shifts (eV) at different U values	
		U=5.3eV	U=2.0eV
CO <sub>2</sub> ads	O2	0.43	0.82
	O2'	0.41	0.81
CO <sub>3</sub> ads	O1	-1.80	-1.39
	O1'	-1.82	-1.36
HCO <sub>3</sub> ads	O1	-3.46	-0.95
	O1'	-3.47	-0.95
CO <sub>3</sub> ads @Ni_vac	O1	-1.29	0.35
	O1'	-1.30	0.31
HCO <sub>3</sub> ads @Ni_vac	O1	0.23	-0.91
	O1'	0.23	-0.90

Table A2. O1s Core-level Binding Energy Shifts Relative to the O1s Core-level Binding Energy of Bulk Lattice Oxygen for Different Surface Adsorbates (corresponding to Fig. A1) on  $\text{Co}_3\text{O}_4$  (100) evaluated at U value of 6.0eV and 3.5eV

Structure	Specific oxygen that are used in for DFT calculation (Labelling indicated in Figure A1.)	DFT-calculated O1s core-level binding energy shifts (eV) at different U values	
		U=6.0eV	U=3.5eV
$\text{CO}_2$ ads	O2	1.31	0.31
	O3	1.33	0.68
$\text{CO}_3$ ads	O1	0.60	-0.05
	O1'	0.56	-0.02
$\text{HCO}_3$ ads	O1	2.26	1.61
	O1'	2.25	1.61

## Appendix B Figures and Tables of Experimental Investigation

Appendix B contains tables and figures that referred in Chapter 5.1, containing information regarding the experimental investigation on low-temperature, water-assisted tandem demethylation of benzyl alcohol to phenol.

Table B1. Particle Size Distribution (PSD) of the synthesized CuO-864 showing the mean radius in nm.

Sample Name	Average size (r.nm)	Size at the peak (r.nm)	Polydispersity
CuO-578	692	518	0.4
CuO-864	146	160	0.13
CuO-1140	1699	798	0.4

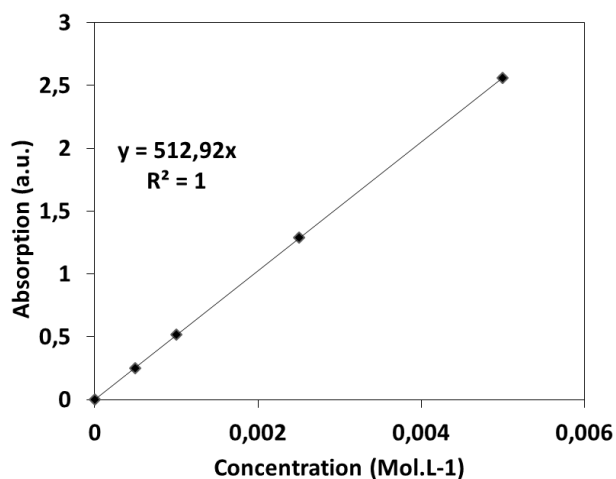


Figure B1. Hydrogen peroxide calibration curve

Hydrogen Peroxide ( $H_2O_2$ ) quantification: Reaction samples were taken directly in the solution from the ultrasound reactor and mixed with the titanium oxysulfate solution in 1/1 v/v (the same conditions as the standards solution). The absorbance is measured at the same wavelength as the one used for the calibration.



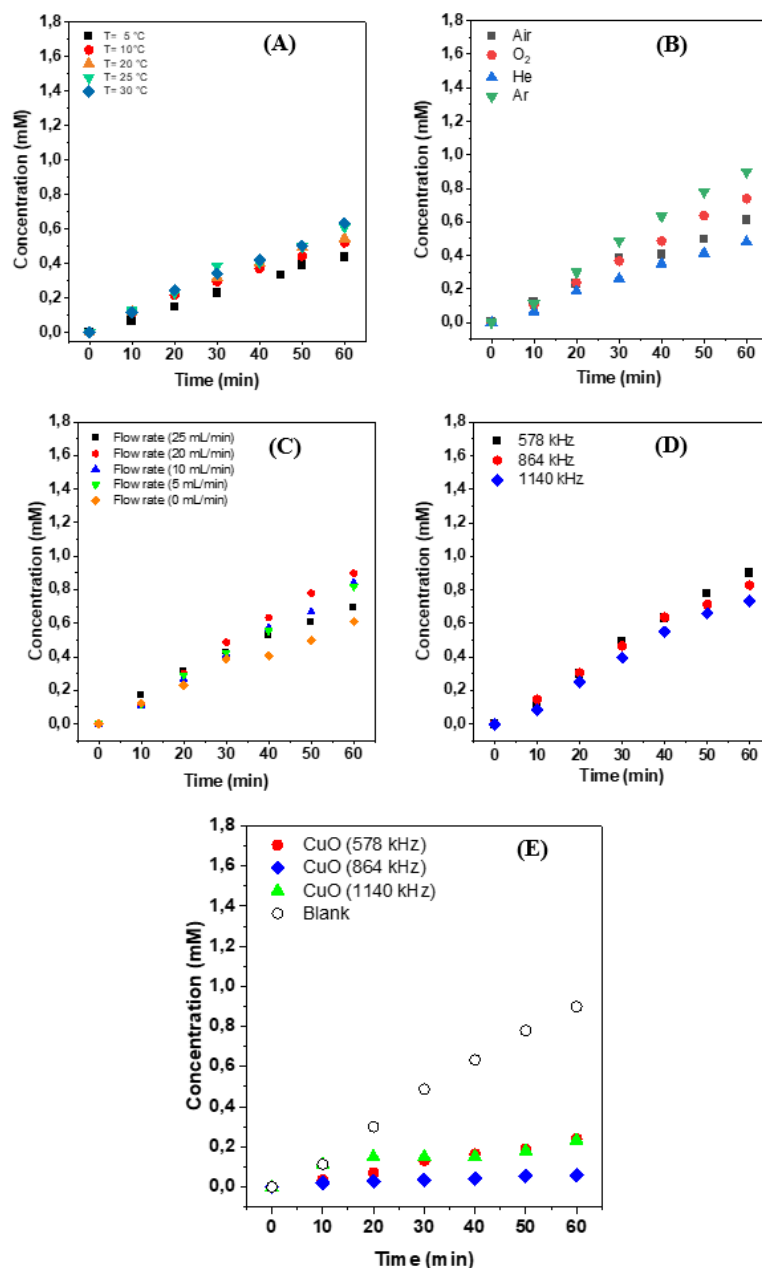


Figure B2. In-situ production of hydrogen peroxide (H<sub>2</sub>O<sub>2</sub>) in 100 mL under different reaction conditions: A) different bulk liquid temperature at 578 kHz ultrasound frequency under air; B) different gas atmospheres with flow rate 20 mL.min<sup>-1</sup> at 578 kHz ultrasound frequency and at controlled temperature 25 °C; C) different argon flow rate at 578 kHz ultrasound frequency atmosphere and at controlled temperature 25 °C; D) different ultrasound frequency under argon 20 mL.min<sup>-1</sup> at controlled temperature 25 °C; E) different CuO (50 mg) catalysts at 578 kHz ultrasound frequency under argon 20 mL.min<sup>-1</sup> at controlled temperature 25 °C.

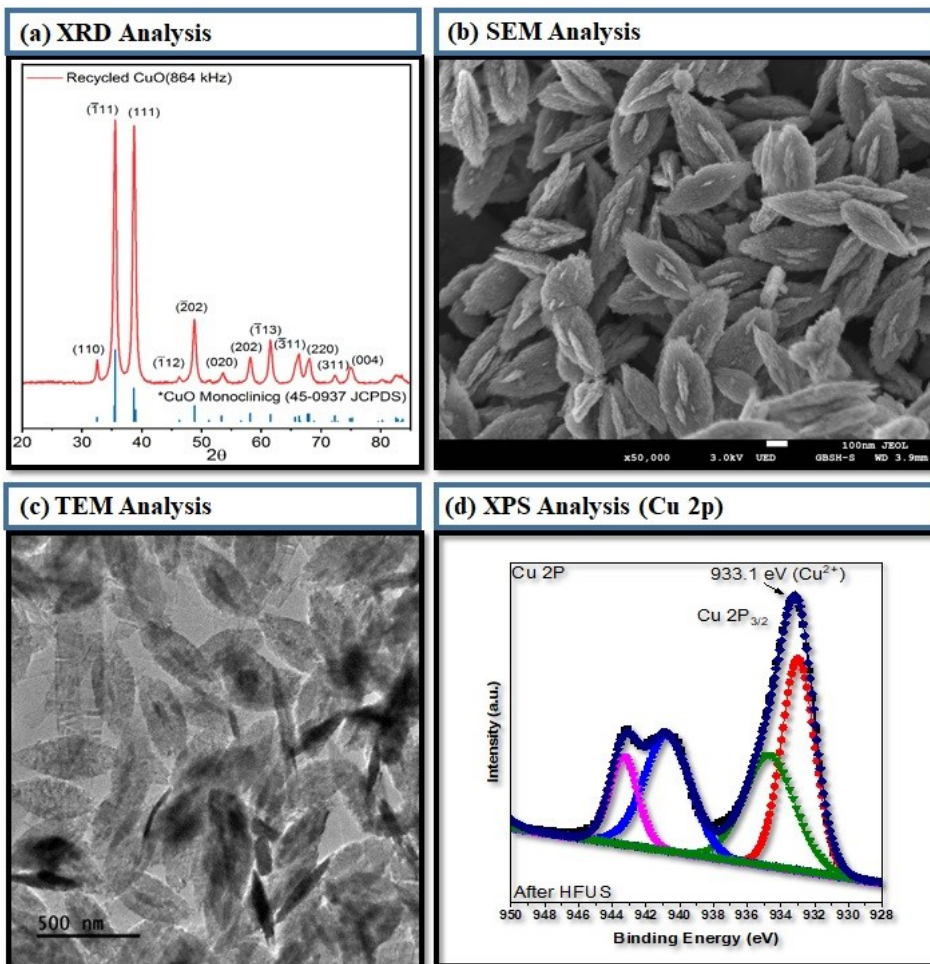


Figure B3. (a) XRD analysis (b) SEM analysis (c) TEM analysis (d) XPS Cu<sub>2</sub>p analysis of recovered CuO catalyst.

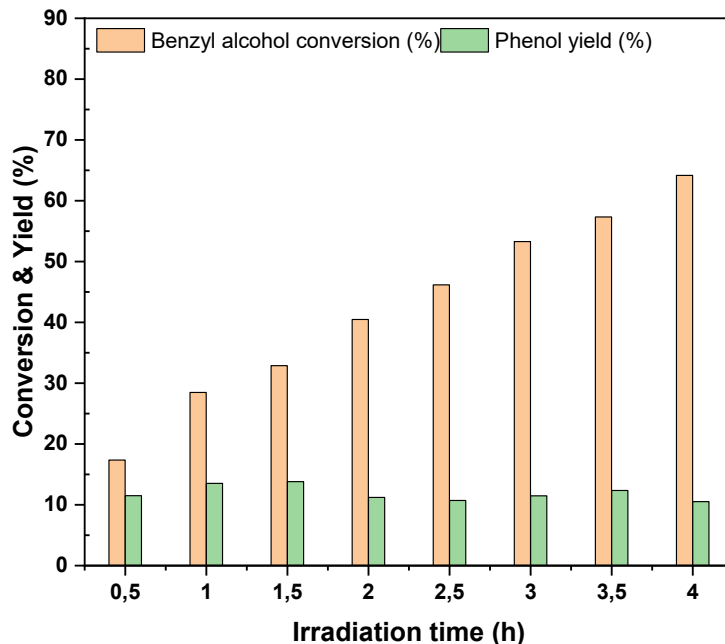


Figure B4. Ultrasonic irradiation time course for benzyl alcohol oxidation. Reaction conditions: 5 mmol.L<sup>-1</sup> Benzyl alcohol, 578 kHz, 0.11 W.mL<sup>-1</sup>, 25 °C

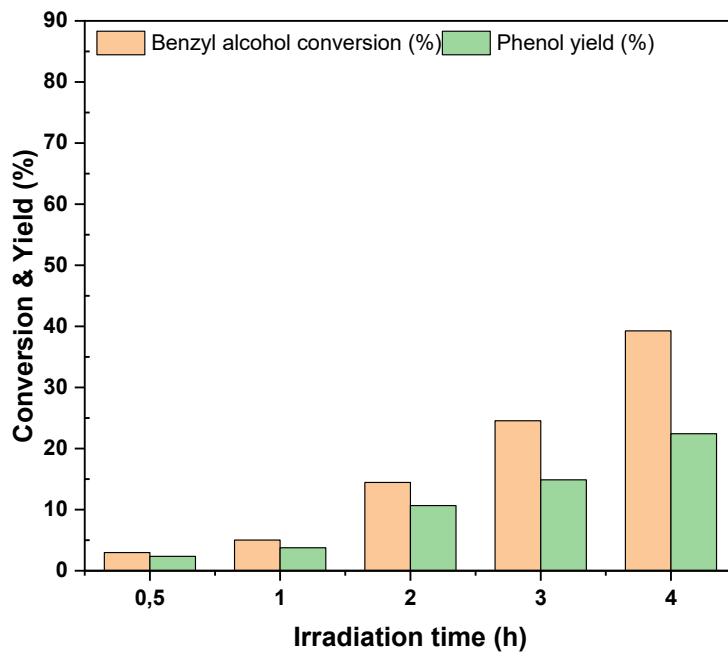


Figure B5. Ultrasonic irradiation time course for benzyl alcohol oxidation over CuO catalyst in the presence of TBA. Reaction conditions: 5 mmol.L<sup>-1</sup> Benzyl alcohol, 5 mmol.L<sup>-1</sup> TBA, 578 kHz, 0.11 W.mL<sup>-1</sup>, 25 °C.

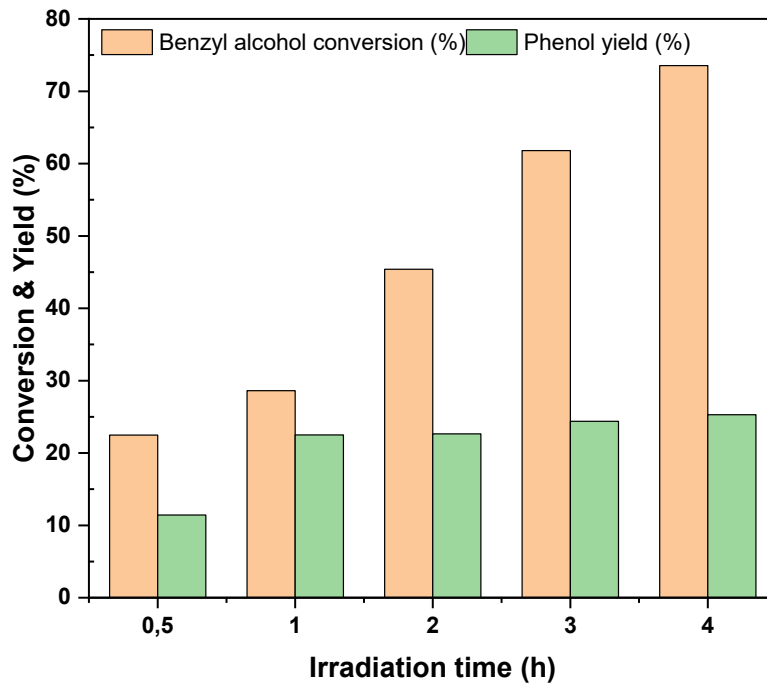


Figure B6. Ultrasonic irradiation time course for benzyl alcohol oxidation over CuO catalyst in the presence of CCl<sub>4</sub>. Reaction conditions: 5 mmol.L<sup>-1</sup> Benzyl alcohol, 5 mmol.L<sup>-1</sup> CCl<sub>4</sub>, 578 kHz, 0.11 W.mL<sup>-1</sup>, 25 °C.

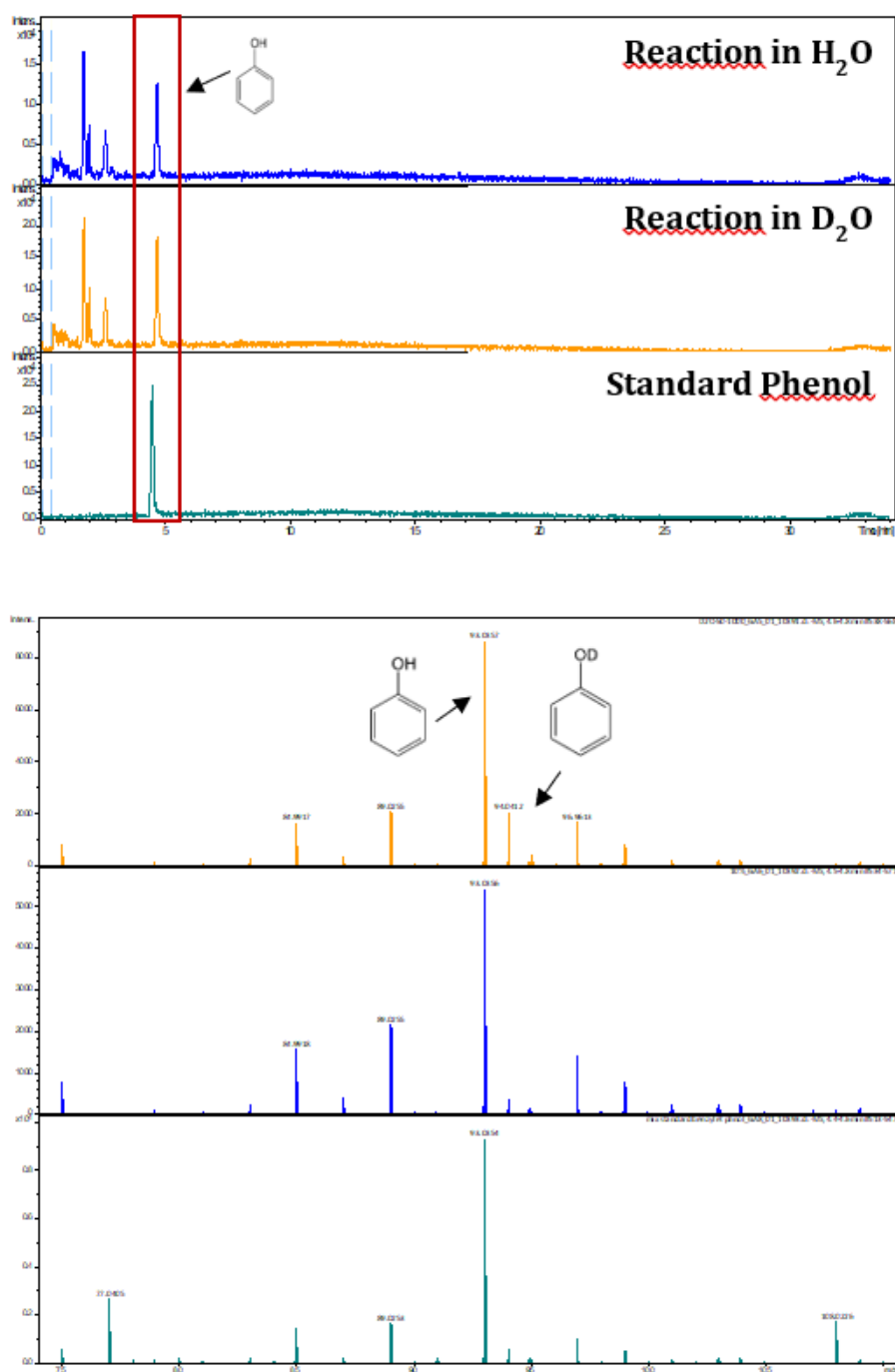


Figure B7. LC-MS analysis of the reaction in water and deuterated water : A) LC-MS chromatograms of benzyl alcohol oxidation over CuO catalyst, benzyl alcohol oxidation over CuO catalyst in D<sub>2</sub>O and Standard phenol. B) ESI-MS Spectra of benzyl alcohol oxidation over CuO catalyst, benzyl alcohol oxidation over CuO catalyst in D<sub>2</sub>O and Standard phenol. Reaction conditions: 5 mmol.L<sup>-1</sup> Benzyl alcohol, 5.4 mg CuO, 578 kHz, 0.11 W.mL<sup>-1</sup>, 25 °C.

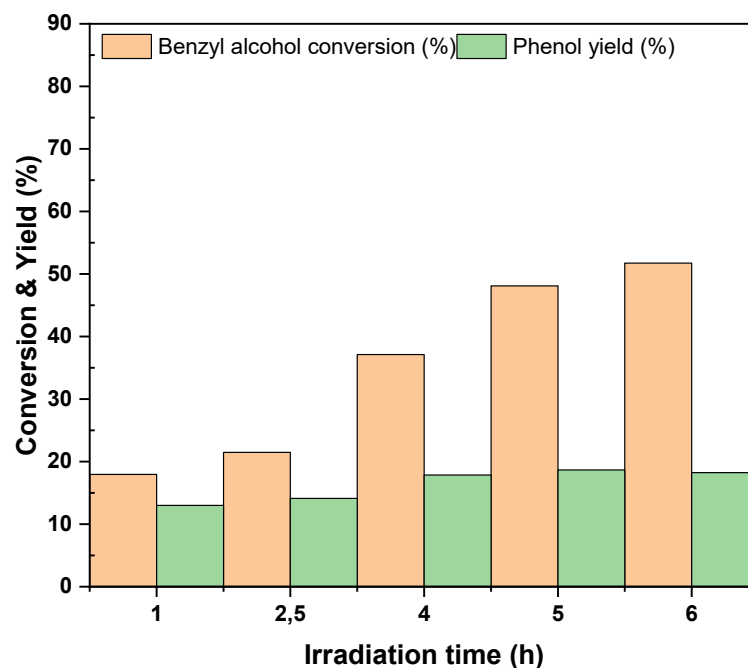


Figure B8. Ultrasonic irradiation time course for benzyl alcohol oxidation over CuO catalyst. Reaction conditions: 5 mmol.L<sup>-1</sup> Benzyl alcohol, 5.4 mg CuO, 578 kHz, 0.24 W.mL<sup>-1</sup>, 60 °C.

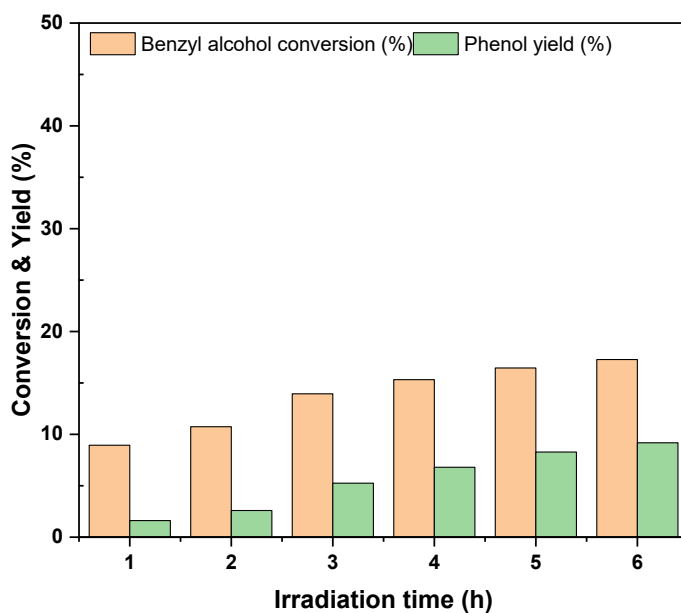


Figure B9. Ultrasonic irradiation time course for benzyl alcohol oxidation over CuO catalyst. Reaction conditions: 50 mmol.L<sup>-1</sup> Benzyl alcohol, 54 mg CuO, 578 kHz, 0.11 W.mL<sup>-1</sup>, 25 °C.

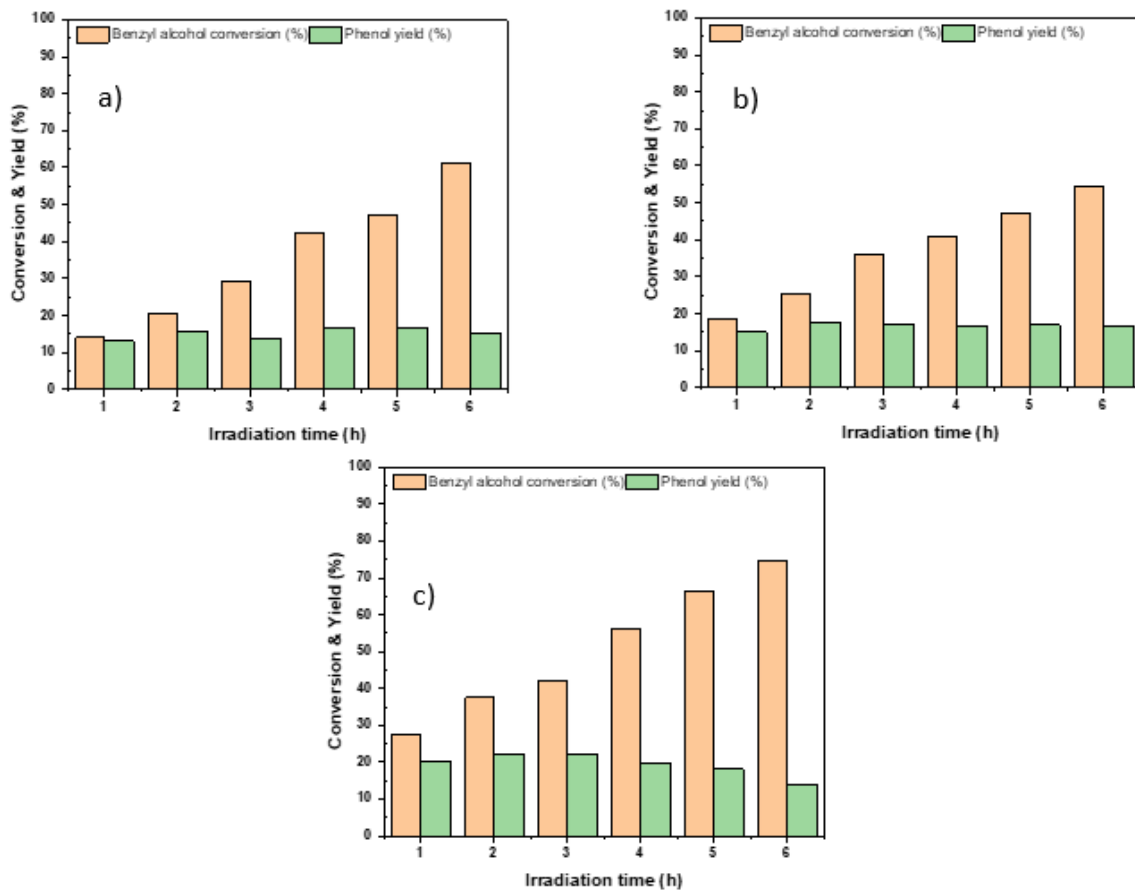


Figure B10. Effect of catalyst loading on the oxidation benzyl alcohol: a) 20%; b) 40%; c) 100%. Reaction conditions: 5 mmol.L<sup>-1</sup> Benzyl alcohol, 5.4 mg CuO, 578 kHz, 0.11 W.mL<sup>-1</sup>, 25 °C.

Table B2. Phenol yields for CuO catalyzed conversion of benzyl alcohol

Entry	Gas atmosphere	Reaction temperature (°C)	Reaction time (h)	H <sub>2</sub> O <sub>2</sub> concentration (mmol.L <sup>-1</sup> )	Conversion (%)	Phenol (%)
1	Argon	25	6	-	0	0
2		100	6	-	0	0
3		1	5	9	1	
		2	5	34.5	13.4	
		3	5	34.7	15.7	
	4	5	34.7	14.5		
		5	5	34.7	14.5	
Benzyl alcohol oxidation over CuO-864 under silent conditions. The reaction parameters are the following: 5 mmol.L <sup>-1</sup> of benzyl alcohol in 100 mL and 5.4 mg of catalyst under argon flow rate 20 mL.min <sup>-1</sup> and stirring 400 rpm						



## Appendix C Free Energy Profile Figures of Undesirable Side Reaction

Appendix C contains the free energy profile figures of undesirable side reactions (black arrow in Figure 14) with configurations of the initial, transition and final state of elementary steps. As the most favorable reaction pathways are shown in Figure 15, all reaction steps shown in this appendix are kinetically unfavourable and unlikely to happen in the experiment.

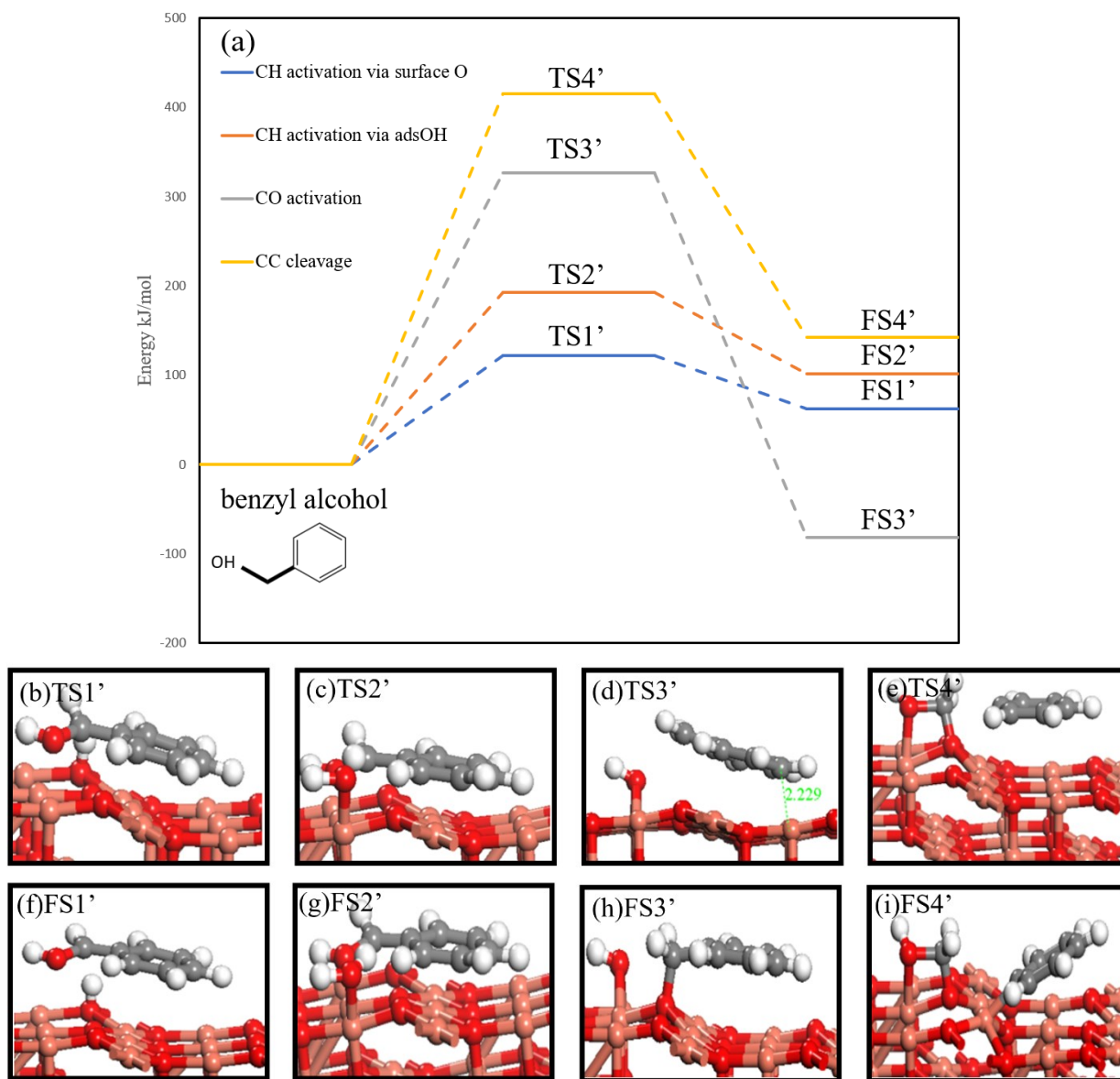


Figure C1. (a) Free Energy profile for the undesirable reaction step from benzyl alcohol on CuO (111) surface; transition state for (b) C-H activation via surface oxygen(TS1'); (c) C-H activation via adsorbed OH (TS2'); (d) C-O cleavage (TS3'); (e) C-C cleavage (TS4'); final state configuration for (f) C-H activation via surface oxygen(FS1'); (g) C-H activation via adsorbed OH (FS2'); (h) C-O cleavage (FS3'); (i) C-C cleavage (FS4') on CuO (111) surface. Activation

free energy barriers and reaction free energies are in kJ/mol. Salmon, red, grey, and white balls represent copper (Cu), oxygen (O), carbon (C) and hydrogen (H) atoms, respectively.

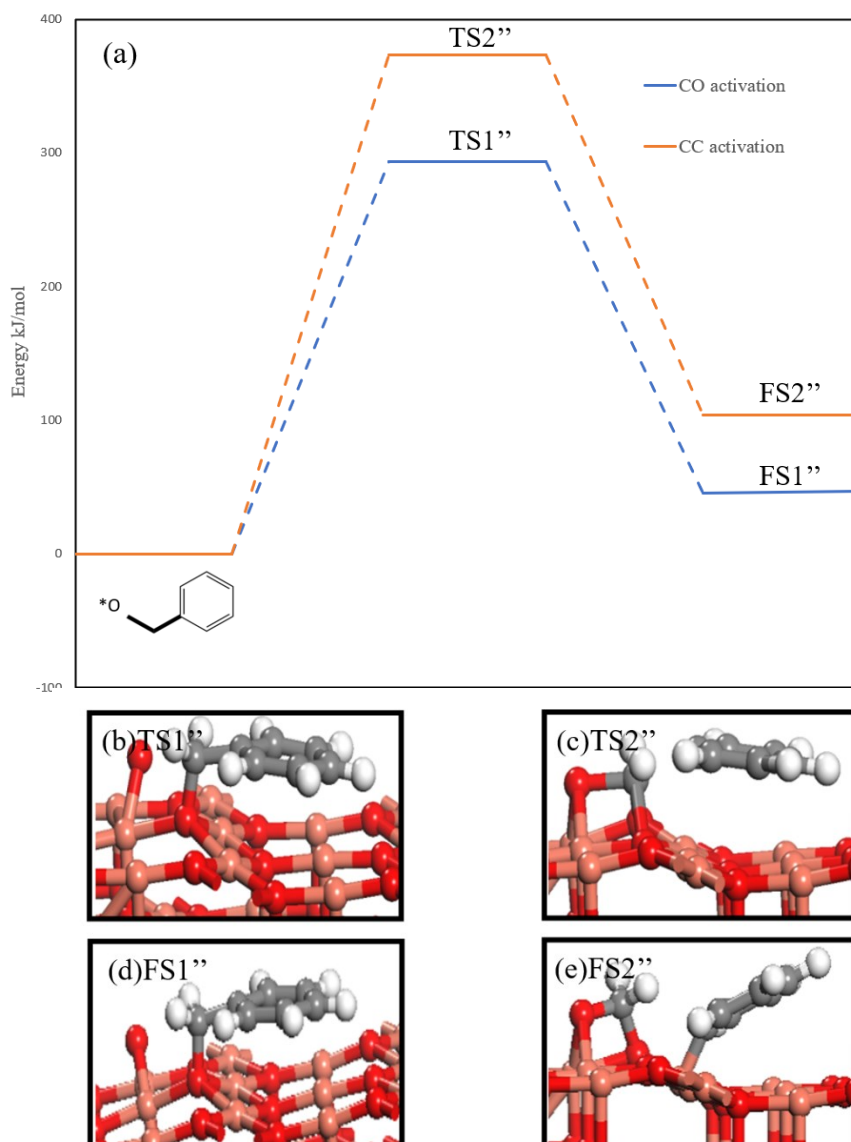


Figure C2. (a) Free Energy profile for the undesirable reaction step from \*O-CH<sub>2</sub>-C<sub>6</sub>H<sub>5</sub> on CuO (111) surface; transition state for (b) C-O cleavage (TS1''); (c) C-C cleavage (TS2''); final state configuration for (h) C-O cleavage (FS1''); (i) C-C cleavage (FS2'') on CuO (111) surface. Activation free energy barriers and reaction free energies are in kJ/mol. Salmon, red, grey, and white balls represent copper (Cu), oxygen (O), carbon (C) and hydrogen (H) atoms, respectively.

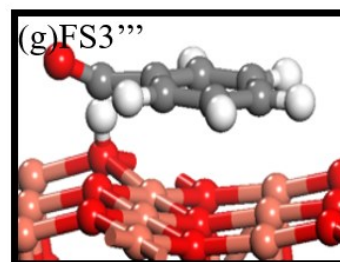
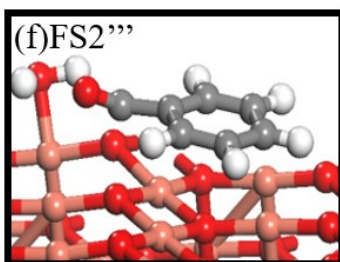
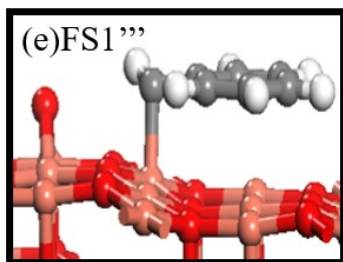
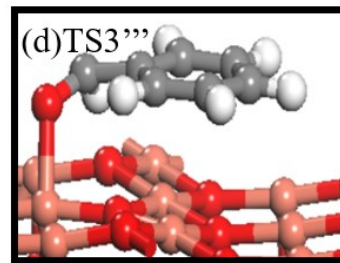
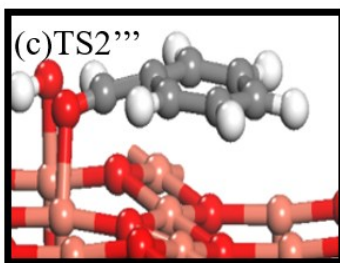
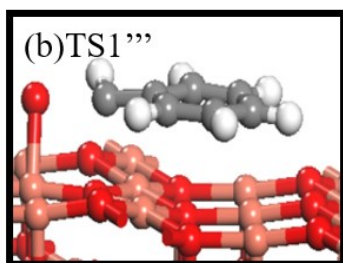
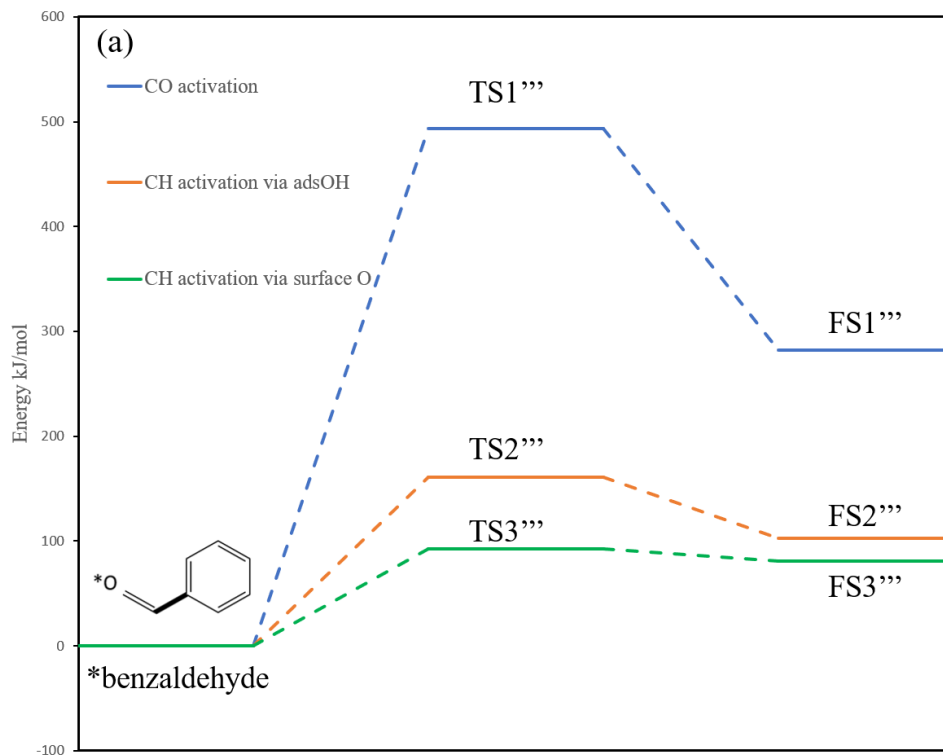


Figure C3. (a) Free Energy profile for the undesirable reaction step from benzaldehyde on CuO (111) surface; transition state for (b) C-O cleavage (TS1'''); (c) C-H activation via adsorbed OH (TS2'''); (d) C-H activation via surface oxygen(TS3'''); final state configuration for (e) C-O cleavage (FS1'''); (f) C-H activation via adsorbed OH (FS2'''); (g) C-H activation via surface oxygen(FS3''') on CuO (111) surface. Activation free energy barriers and reaction free energies are in kJ/mol. Salmon, red, grey, and white balls represent copper (Cu), oxygen (O), carbon (C) and hydrogen (H) atoms, respectively.

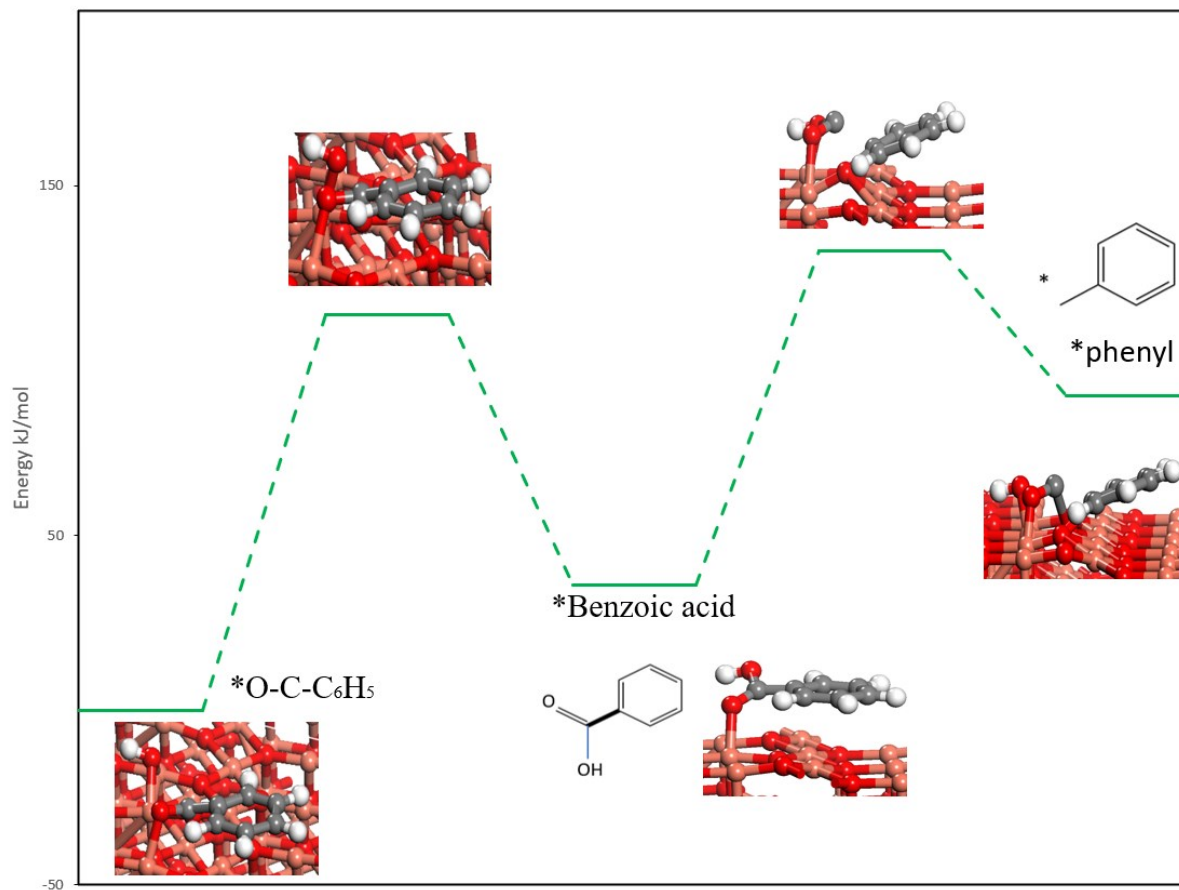


Figure C4. Free energy profile for pathways which benzoic acid as an intermediate on CuO (111). Activation free energy barriers and reaction free energies are indicated in kJ/mol. Salmon, red, grey, and white balls represent copper (Cu), oxygen (O), carbon (C) and hydrogen (H) atoms, respectively.